Analysis of Water Flowback and Gas Production Data for Fracture Characterization in the Horn River Basin

by

Yanmin Xu

A thesis submitted in partial fulfillment of the requirements for the degree of

Doctor of Philosophy

in

Petroleum Engineering

Department of Civil & Environmental Engineering
University of Alberta

Abstract

Shale gas is one of the most promising energy resources due to its wide distribution, abundant reserves, and low pollutant emissions to the environment. Although shale gas plays usually have very low permeability and porosity, the use of horizontal drilling and hydraulic fracturing technologies has made their economic production possible. This is achieved by creating complex fracture networks underground, through which the trapped gas flows from the rocks to the wellbore. Since these induced fracture networks are essential for hydrocarbon recovery forecast and future operation optimization, the industry is very interested in their characterization.

The data recorded immediately after opening the wells during flowback present the earliest opportunity to characterize the stimulated reservoirs. The objectives of this study include: 1) investigating flow regimes and understand fluid flow physics during flowback period, and 2) quantitatively characterizing the induced fracture network by analyzing the flowback rate and pressure data. The study focuses on an eight-well pad completed in the Horn River Basin, and aims to develop a protocol for flowback data analysis in gas shales. The main steps and key results are summarized in subsequent paragraphs below.

Step 1 constructs a series of diagnostic plots for investigating flow regimes in target shale gas wells. The rate plots show two-phase production at the very beginning of flowback period. The Gas Water Ratio plots separate the flowback period into two regimes: an early-time flow regime characterized by decreasing Gas Water Ratio trend, and a late-time flow regime characterized by increasing Gas Water Ratio trend.

Step 2 builds a numerical model to validate the flow signatures observed in field data using a commercial reservoir simulation software. The numerical model simulates the fracturing, shut-

in, and the flowback processes. The results suggest that the gradual build-up of gas in the fractures during shut-in is responsible for the immediate two-phase flowback. The results also suggest that the early-time flow regime indicates fracture depletion with negligible fluid support from the matrix; while the late-time flow regime suggests significant fluid and pressure communication between the matrix and the fracture systems.

Step 3 develops three material balance models for quantitatively characterizing the effective fracture network. These models include a closed-tank model, a closed-tank flowing model, and an open-tank model. Both closed-tank models estimate the initial volume of the effective fracture network from the early-time flowback data, while the open-tank model estimates the effective fracture-matrix interface area from the late-time flowback data.

Step 4 conducts a comparative volumetric analysis by using the estimated fracture parameters, total injected volume, pressure and water production profiles during flowback. The objectives of this step are to understand the hydraulic fracturing efficiency and to investigate the change in effective fracture volume with time during flowback period. The results show that most of the fracturing fluids are used in creating effective fracture volume. However, there is severe fracture volume loss during early-time flowback due to excessive pressure drop. The severe fracture closure is a key drive mechanism for early-time two-phase flowback. The results also imply that part of the induced fracture network may not contribute to long-time production.

Step 5 develops a mathematical model to estimate fracture compressibility, which is a key parameter to evaluate fracture closure in material balance analysis. The results show that fracture compressibility comprises two parts: the rate of fracture aperture change and the rate of fracture porosity change with respect to the change in effective pressure. The results show that proppants play a dominant role in resisting fracture closure and reducing the fracture volume loss. The results also indicate that the severe fracture volume loss during early-time flowback is mainly due to the closure of unpropped fractures.

Overall, this research demonstrates the feasibility of flowback data analysis for fracture characterization in shale gas reservoirs. Although this study focuses on an eight-well pad completed in the Horn River Basin, the methodology and some results could be extended for applications in other shale gas reservoirs.

Preface

All or parts of Chapters 2 to 5 have been published as peer-reviewed, journal papers. Chapters 2 and 3 have been published as "Xu, Y., Adefidipe, O. A., Dehghanpour, H. 2015. Estimating Fracture Volume Using Flowback Data from the Horn River Basin: A Material Balance Approach. *Journal of Natural Gas Science and Engineering*, 25: 253-270". Chapter 4 has been published as "Xu, Y., Adefidipe, O. A., Dehghanpour, H. 2016. A Flowing Material Balance Equation for Two-Phase Flowback Analysis. *Journal of Petroleum Science and Engineering*, 142, 170-185". Chapter 5 has been published as "Xu, Y., Dehghanpour, H., Ezulike, D. O., Virues, C. 2017. Effectiveness and Time Variation of Induced Fracture Volume: Lessons from Water Flowback Analysis. *Fuel*, 210 (15): 844-858". I was responsible for analyzing field data, forming key concepts, developing mathematical and numerical models, interpreting model outputs, writing and editing manuscripts. My co-authors assisted in collecting relevant data, forming research outlines, discussing model outputs, reviewing manuscripts, and securing company approvals for publication. None of the materials in this dissertation has been presented in the co-authors' theses.

Dedication

To my family.

Acknowledgements

First and foremost, I would like to express my sincere gratitude to my supervisor, Dr. Hassan Dehghanpour. Without a doubt, Dr. Dehghanpour has been an incredible teacher, mentor, and supporter during my five years of Ph.D. study. This dissertation would not have been possible without his insightful guidance, warm encouragement, and kind support. I feel extremely lucky to be a student of this talented young professor. His advice and guidance will be with me throughout my life.

I would like to thank Dr. Juliana Leung and Dr. Rick Chalaturnyk for their valuable discussions and feedbacks as my supervisory committee members. I would also like to thank Dr. Roberto Aguilera, Dr. Wei Victor Liu, and Dr. Yaman Boluk for attending my Ph.D. defense exam.

I have benefited a lot from extensive discussions and conversations with many people. I would like to acknowledge my industrial collaborators, Claudio Virues and Doug Bearinger for their technical inputs. I am grateful to Prof. Teng-fong Wong for being the host supervisor during my visit at the Chinese University of Hong Kong and for remarking on my research work. I would also like to appreciate my past and present colleagues, Dr. Obinna Ezulike, Tobi Adefidipe, Yingkun Fu, Dr. Ashkan Zolfaghari, Mingxiang Xu, Yue Shi, Mahmood Reza Yassin, Ali Habibi, Dr. Shu Yang and Ebrahim Ghanbari for their useful comments and suggestions.

I am grateful to the staff members at the Department of Civil and Environmental Engineering for handling administrative work. I am in particular grateful to Arlene Figley for her patience and encouragement during my tough times.

I gratefully acknowledge Natural Sciences and Engineering Research Council of Canada and Nexen Energy ULC for funding this study. I also appreciate Nexen Energy ULC for providing priceless field data and Computer Modeling Group for providing academic license for this research.

Finally, special thanks go to my family and friends for their love and support. Thank you for listening to the ups and downs in my journey, and sharing the laughter and tears in your lives. I love you all.

Table of Contents

List of Tables

List of Figures

Abbreviations

BHP	Bottomhole Flowing Pressure
CBM	Coal Bed Methane
CMG	Computer Modeling Group
DFIT	Diagnostic Fracture Injection Tests
DRP	Dynamic Relative Permeability
E	Expansion Coefficient
EIA	Energy Information Administration
EGP	Early Gas Production
EV	Evie
F	Underground Withdrawal
GRG	Generalized Reduced Gradient
GWR	Gas Water Ratio
HFE	Hydraulic Fracturing Efficiency
HR	Horn River
HRB	Horn River Basin
LGP	Late Gas Production
LGR	Local Grid Refinement
MBE	Material Balance Equation
MICP	Mercury Injection Capillary Pressure
MU	Muskwa

OP	Otter Park
RNP	Rate Normalized Pseudo-Pressure
SRV	Stimulated Reservoir Volume
TIV	Total Injected Volume
TLR	Total Load Recovery
UCS	Unconfined Compressive Strength

Chapter 1: Introduction

1.1 Overview

This section briefly introduces the key terminologies and the common field practices mentioned in this dissertation.

1.1.1 Unconventional Reservoirs

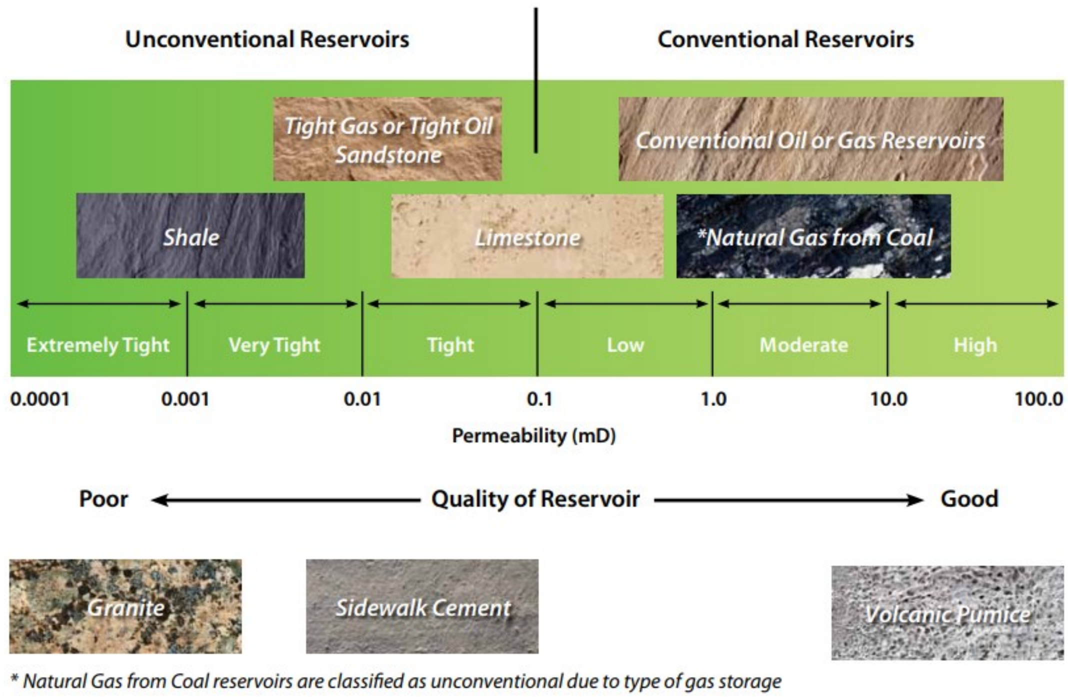

Figure 1.1: Comparison of rock matrix permeability between common unconventional and conventional reservoirs (Canadian Society for Unconventional Resources, 2018)

Unconventional reservoirs are the reservoirs that require special recovery operations (such as stimulation treatments or steam injection) for economic production of oil and gas resources (Wikipedia, 2018). Unconventional reservoirs include tight oil and gas sandstones, oil and gas shales, coal bed methane reservoirs, heavy oil and tar sands, and gas-hydrate deposits. In this study, "unconventional" refers to tight sandstones and shale, which have low permeability and porosity for oil and natural gas to move through the rock to the well. Figure 1.1 compares the rock matrix permeability between unconventional and common conventional reservoirs.

1.1.2 Unconventional Resources

The United States Energy Information Administration (EIA) defines unconventional resources as "an umbrella term for oil and natural gas that is produced by means that do not meet the criteria for conventional production". The unconventional resources and their conventional counterparts have similar chemical composition; the term "unconventional" simply refers to how they are produced and the types of rock in which they are found. Unconventional resources include shale and tight oil and gas, and coalbed methane (CBM). Unconventional resources are widely distributed in the world. Figure 1.2 shows the worldwide unconventional resources.

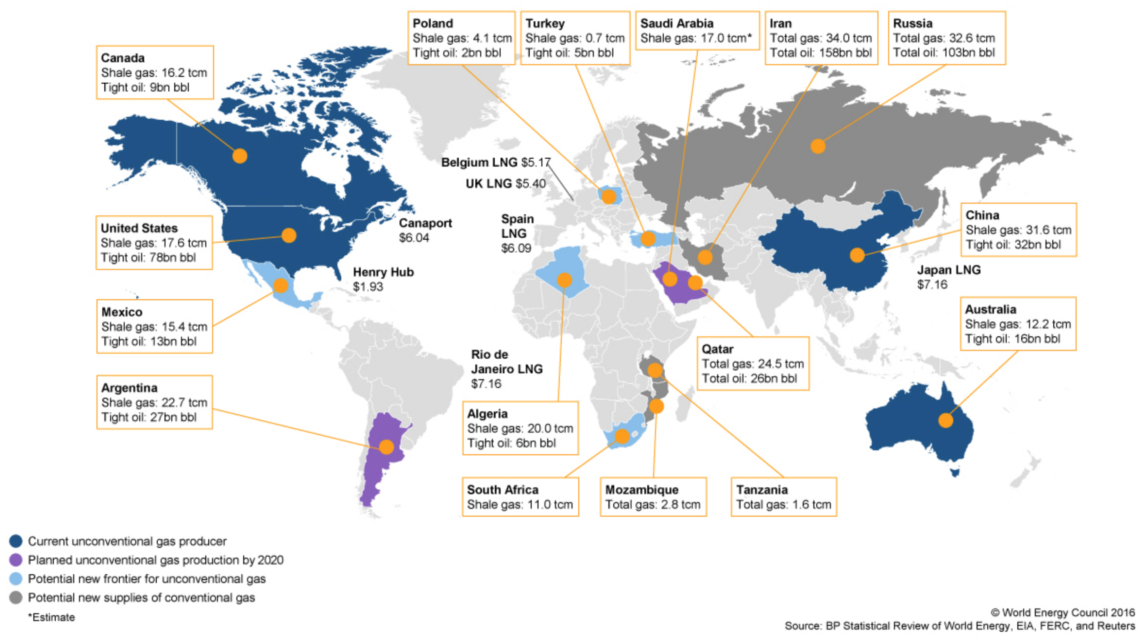

Figure 1.2: Worldwide unconventional resources (World Energy Council, 2016).

1.1.3 Shale Gas

Shale gas is the natural gas that is found trapped in shale plays. Shale a sedimentary rock composed of mud and clay particles that are less than 0.004 mm (Blatt et al., 2005). It is formed in stagnant water conditions (such as deep ocean water, lagoons, lakes and swamps) which allow the settling of extremely-fine clay particles. Due to the fine particles, shale usually has ultra-low porosity and permeability (Neuzil, 1994; Katahara, 2008).

Since the start of this century, shale gas has become an increasingly important hydrocarbon resource in the United States and throughout the world. Figure 1.3 shows the U.S. natural gas production by source from 1990 to 2040. In 2000, shale gas only accounted for 5 % of the total natural gas production in the United States. By 2015, this number increases to over 40 %. The EIA also predicts that by 2040, shale gas will account for over two thirds of the total natural gas production in the United States (EIA, 2018).

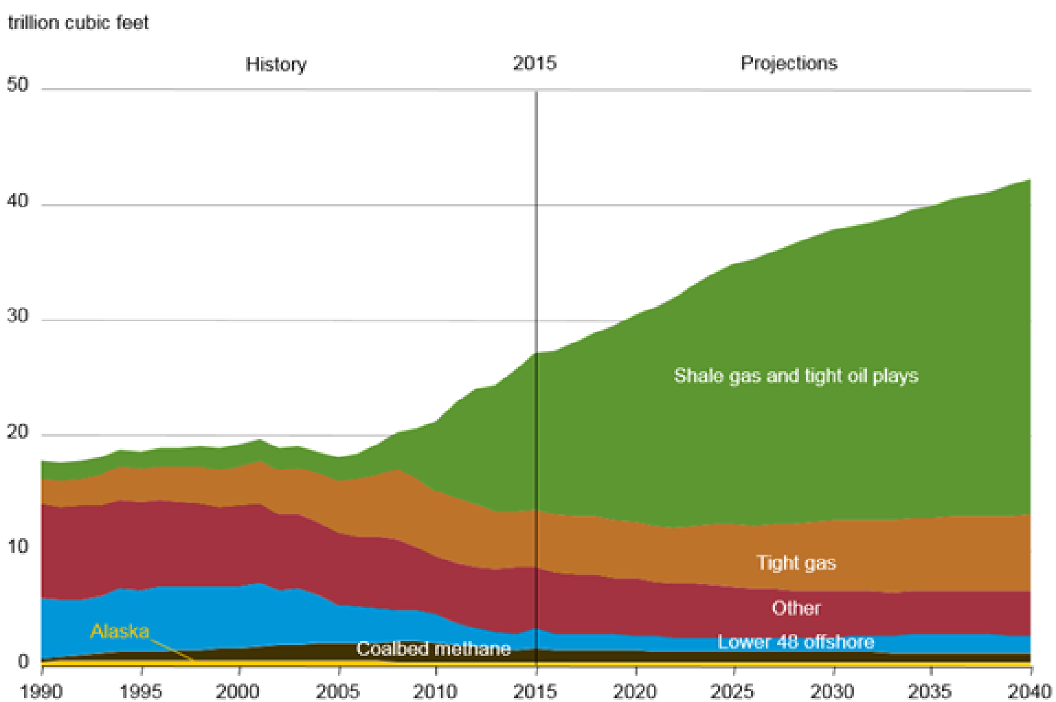

Figure 1.3: U.S. natural gas production by source from 1990 to 2040. Shale gas production starts to boom from 2010 and will account for over two thirds of the total natural gas production by 2040 (EIA, 2015).

Shale gas is widely distributed over the world, with estimated worldwide technically recoverable resources of 7,576.6 Tcf (EIA, 2015). The success exploitation of this natural gas resources in the United States has lead to the interest in shale gas development to the rest of the world. The field data used in this study is from the Horn River Basin (HRB), a shale gas play located in British Columbia, Canada.

Due to the ultra-low porosity and permeability of shales, shale gas cannot be economically produced using conventional techniques. The combination of horizontal well drilling and multi-stage hydraulic fracturing are adopted to exploit shale gas reservoirs and release the natural gas resources. Sections 1.1.4 and 1.1.5 introduce horizontal well drilling and hydraulic fracturing techniques, respectively.

1.1.4 Horizontal Well and Pad Drilling

Figure 1.4 compares a vertical well and a horizontal well. The horizontal well increases the surface area of the wellbore exposed to reservoir's pay zone. Therefore, a horizontal well usually have higher flow rate and hydrocarbon production. The drilling of a horizontal well includes three steps: 1) drill the vertical section to a "kick off" point (i.e. a location just above the target reservoir); 2) deviate the wellbore from vertical direction to intersect the reservoir at the "entry point" with a near-horizontal direction; and 2) drill the horizontal section to reach the desired well length (Helms, 2008).

Pad drilling is also called multi-well pad drilling. It is a practice that allows multiple wells to be drilled from a single, compact piece of land (i.e. well pad) (Figure 1.5). The multiple wells in the same well pad may share the vertical wellbore section. Pad drilling has been widely used in shale gas development: 80-90 % of the horizontal wells today are pad-drilled. Pad drilling helps to cut down the drilling and operational costs (e.g. monitoring costs, production facilities), increase the drilling efficiency, as well as minimize the environment impact (such as access roads and surface facilities).

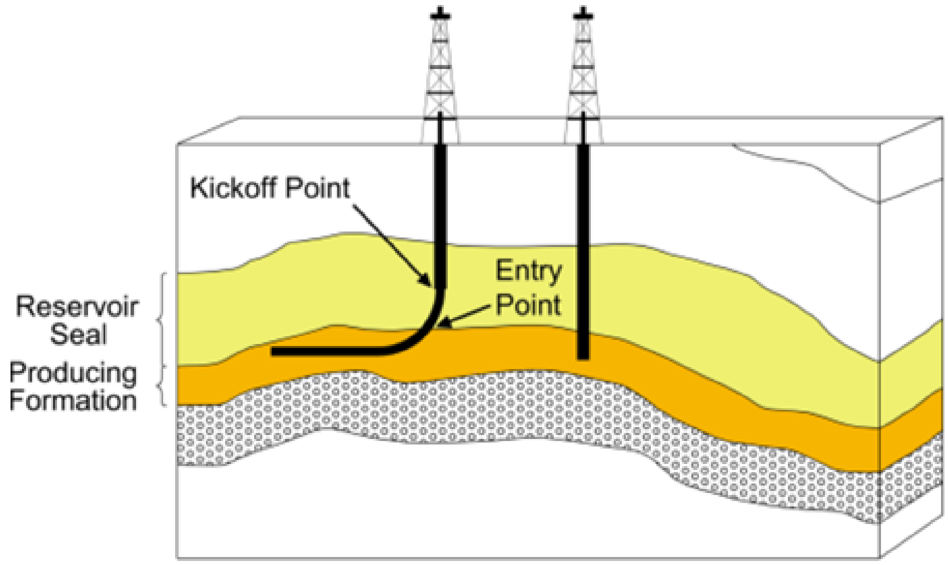

Figure 1.4: Comparison between a horizontal well (left) and a vertical well (right). The horizontal well increases the surface area of the wellbore exposed to reservoir's pay zone (from Helms, 2008).

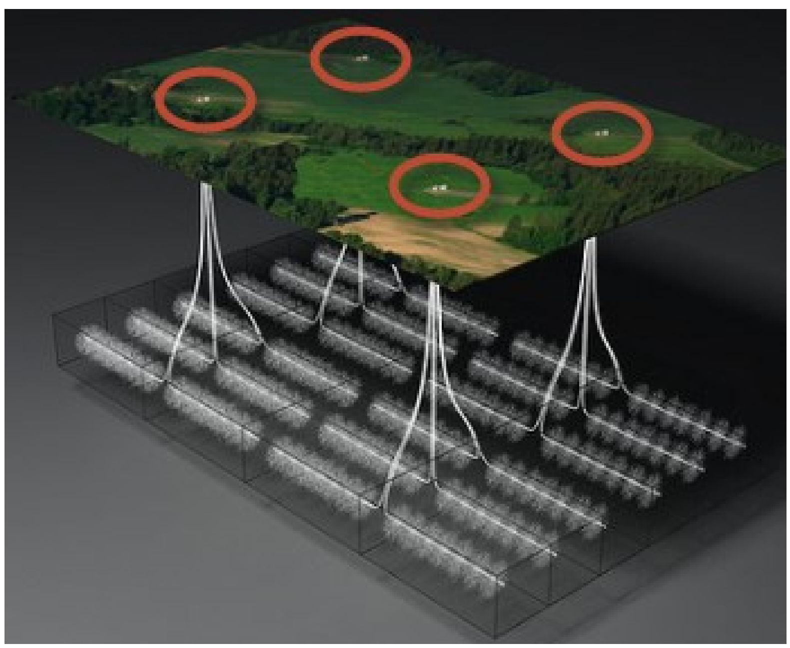

Figure 1.5: Schematic illustration of pad drilling. Pad drilling help to develop the reservoirs while remain minimum surface facilities (shown by red circles) (EIA, 2012).

1.1.5 Hydraulic Fracturing

After horizontal well drilling, multi-stage hydraulic fracturing is adopted to create flow paths (i.e. fractures) for fluid flow. Figure 1.6 schematically illustrates the hydraulic fracturing process. High-pressure fracturing fluids (water + chemicals) and proppants are pumped into the horizontal wellbore and create fractures (i.e. fissures) in the target formation. The injected proppants help to keep the induced fractures open. The trapped natural gas resource is thus released from the rock and flows from the reservoir into the wellbore through the induced fractures.

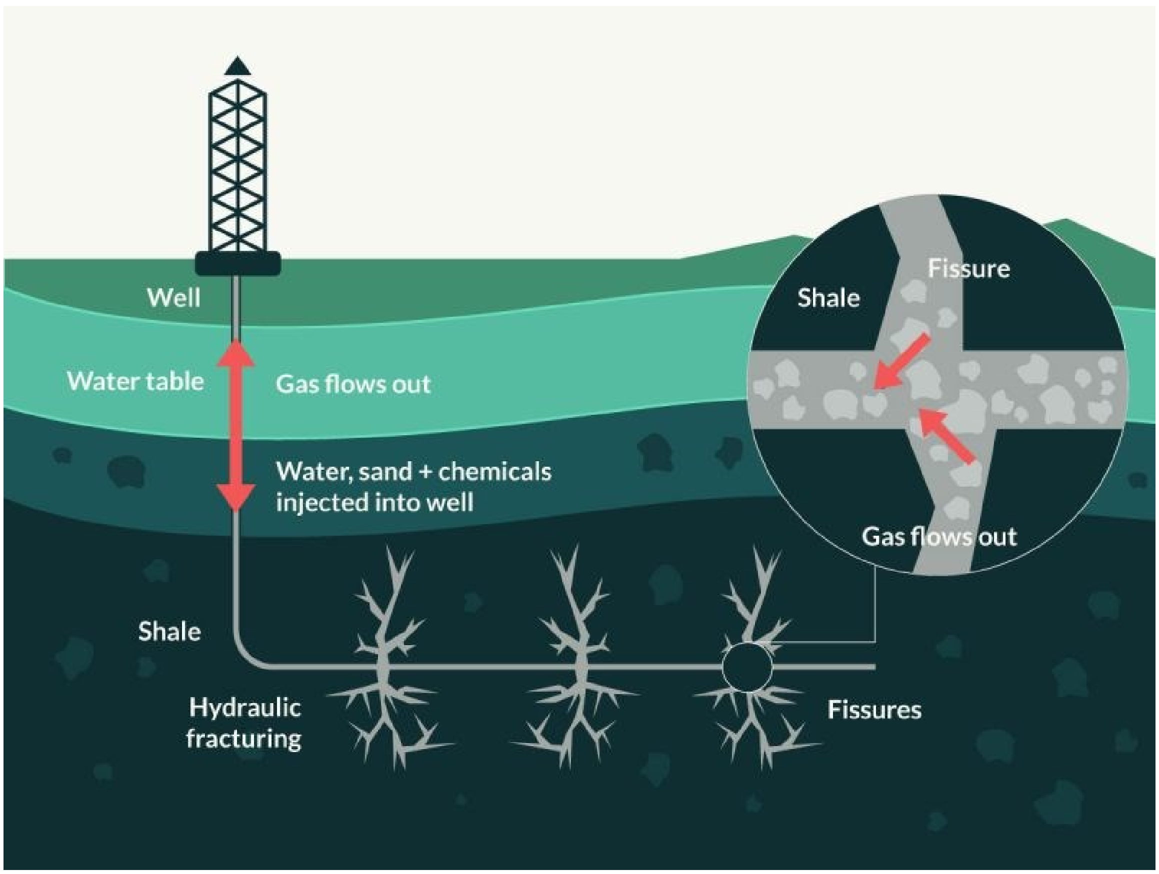

Figure 1.6: Schematic illustration of hydraulic fracturing process in a shale formation. Gas flows from the formation to the wellbore through the induced fissures (from Friends of the Earth, 2017).

1.1.5.1 Fracturing Fluids

The purposes of the fracturing fluids are to extend induced fractures, carry proppants to the fracture tip, and control fluid loss into the formation (Montgomery, 2012).

Slickwater, which is water-based fracturing fluids mixed with friction-reducing additives, is the predominant fracturing fluids used for hydraulic fracturing operations in shale gas reservoirs (B.C. Oil & Gas Commission, 2012). The friction-reducing additives allows fracturing fluids to be pumped at a higher rate and a reduced pressure. Figure 1.7 shows the composition of a typical fracturing fluid for shales, which contains 90 % water, 9.5 % proppants, and 0.5 % chemical additives. The additives in the fracturing fluids include diluted acid, friction reducer, and surfactants. Table 1.1 lists common additives in the fracturing fluids. The chemical additives used in the fracturing treatment depends on company preference, source water quality and reservoir properties.

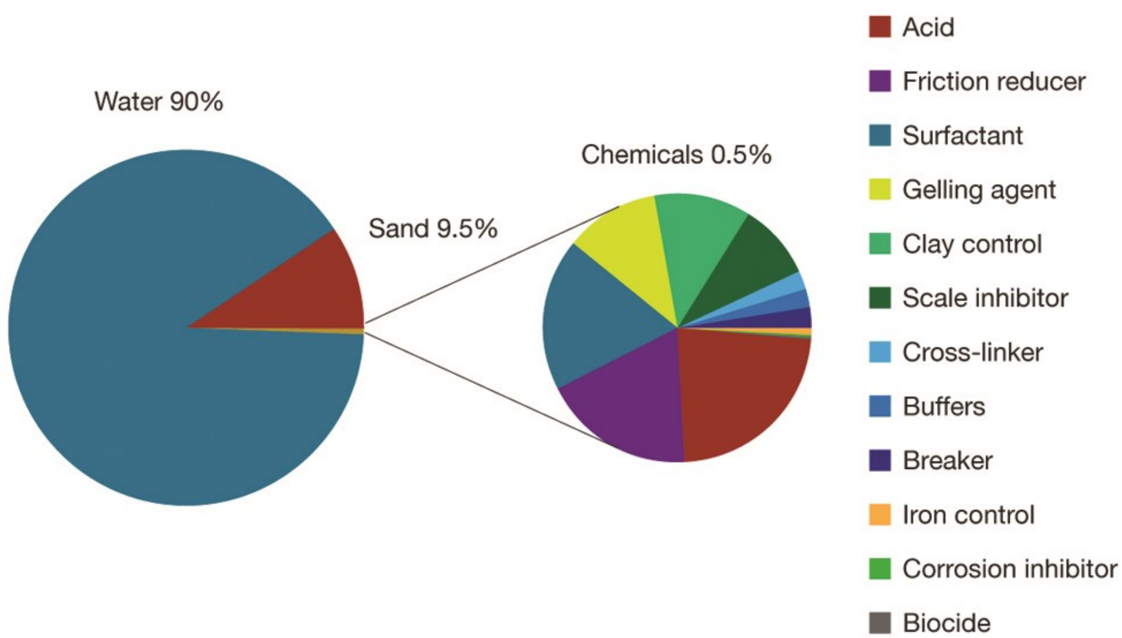

Figure 1.7: Composition of a typical fracturing fluid for hydraulic fracturing operations (Government of Western Australia, 2018).

Table 1.1: Common fracturing fluid additives used in hydraulic fracturing of gas shales (Authur et al., 2008).

Additive Type	Main Compound(s)	Purpose
Diluted Acid (15%)	Hydrochloric or muriatic acid	Help dissolve minerals and initiate cracks in the rock
Biocide	Glutaraldehyde	Eliminates bacteria in the water
Breaker	Ammonium persulfate	Allows a delayed break down of the gel polymer chains
Corrosion Inhibitor	N,n-dimethyl formamide	Prevents corrosion of the pipe
Crosslinker	Borate salts	Maintains fluid viscosity as temperature increases
Friction Reducer	Polyacrylamide Mineral oil	Minimizes friction between the fluid and the pipe
Gel	Guar gum	Thickens the water to suspend the sand
Iron Control	Citric acid	Prevents precipitation of metal oxides
KCl	Potassium chloride	Creates a brine carrier fluid
Oxygen Scavenger	Ammonium bisulfite	Removes oxygen from the water to prevent corrosion
pH Adjusting Agent	Sodium/potassiumm carbonate	Maintains the effectiveness of other components
Scale Inhibitor	Ethylene glycol	Prevents scale deposits
Surfactant	Isopropanol	Increase the viscosity of the fracturing fluid

1.1.5.2 Proppants

Proppants are small, granular, solid materials (such as sands) injected with the fracturing fluids during hydraulic fracturing operations. They are used to keep the fractures open for fluid flow over long periods. Figure 1.8 shows four types of proppants commonly used in hydraulic fracturing operations. Compared with natural sands, ceramic has higher strength and creates fractures with higher conductivity.

The sizes and shapes of proppants are very important because they determine the permeability and conductivity of the induced fracture. A fracture with wide range of particle sizes and shapes will have tight packing, low permeability and low conductivity (Liang et al., 2016). Proppant sizes are usually described using mesh size. Typical proppant sizes are between 8-140 mesh (i.e. 106 µm - 2.36 mm). Table 1.2 presents typical proppant sizes for hydraulic fracturing operations. The shape of the proppants are visually estimated using the Krumbein/Sloss chart (Figure 1.9).

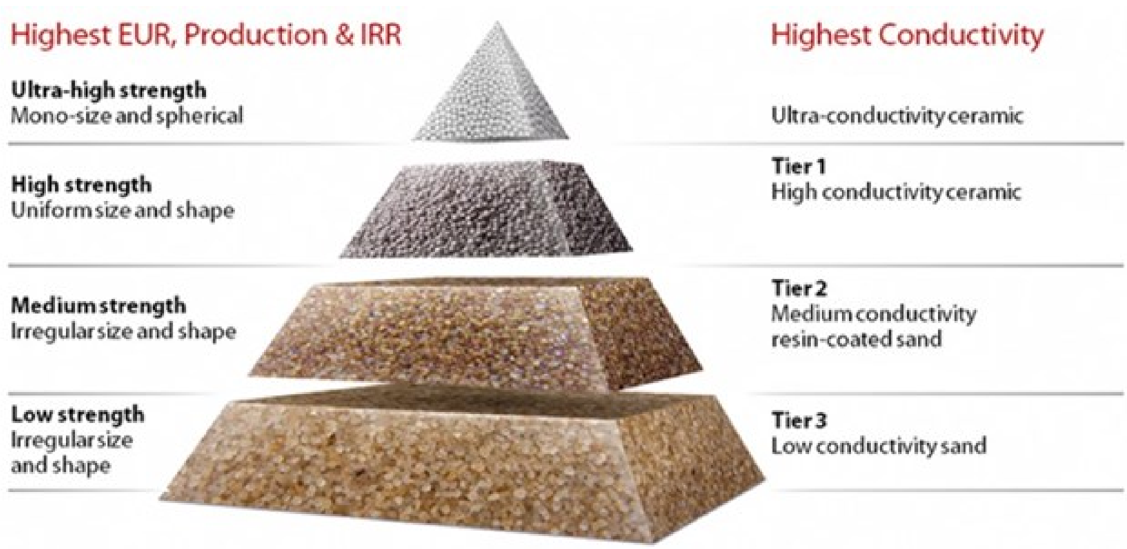

Figure 1.8: Four types of proppants commonly used in hydraulic fracturing (from ASD Report, 2015).

Table 1.2: Typical proppant sizes used in hydraulic fracturing treatment (Lutynski, 2015).

Mesh Size	Particle Size Range (µm)
10/14	1,400 - 2,000
12/18	1,000 - 1,700
16/20	8,500 - 1,180
16/30	600-1180
20/40	420 - 850
30/50	300 - 600
40/70	212 - 420
70/140	106 - 212

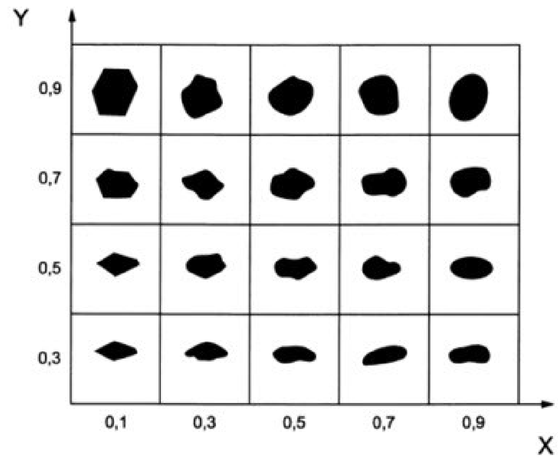

Figure 1.9: Krumbein/Sloss chart for visual estimation of sphericity (y-axis) and roundness (x-axis) (Krumbein and Sloss, 1996).

1.1.6 Shut-In

After hydraulic fracturing, the wells usually go through a shut-in period (also referred as "soaking" in some literature). During shut-in, surface facilities (such as gas pipelines) are installed in preparation for subsequent production (Liu et al., 2015). The shut-in period usually lasts 10-30 days.

During shut-in, the fracturing fluids are in contact with the shale rocks, causing physical, chemical, and mechanical changes underground. Currently, there are different views on the effects of shut-in on well production performance. Some researchers believe that leaving the fracturing fluid in the formation is detrimental to hydrocarbon production due to formation damage and reduced relative permeability in host rocks (Holditch, 1979; Noel and Crafton, 2013; Crafton 2015). The formation damage is especially severe for clay-rich shales since the water occupying the pore and fracture space will cause clays to swell. Besides, the fracturing fluids might cause water blockage in shales, as shown in Figure 1.10. During the shut-in period, fracturing fluids imbibe into the rock matrix due to the high capillary pressure of the host rock. The imbibed water accumulate near the fracture surface and forms a water-invaded zone with high water saturation. The water-invaded zone has low relative permeability for gas phase. The gas in the matrix cannot flow across this water-invaded zone and therefore resulting in low gas recovery.

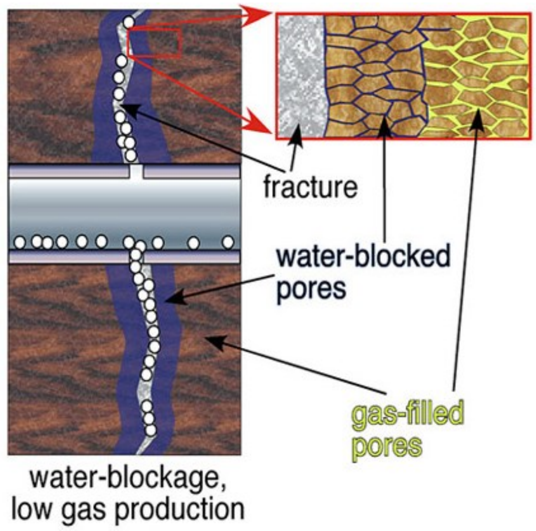

Figure 1.10: Schematic illustration of water blockage in shales (Tokunaga et al., 2016).

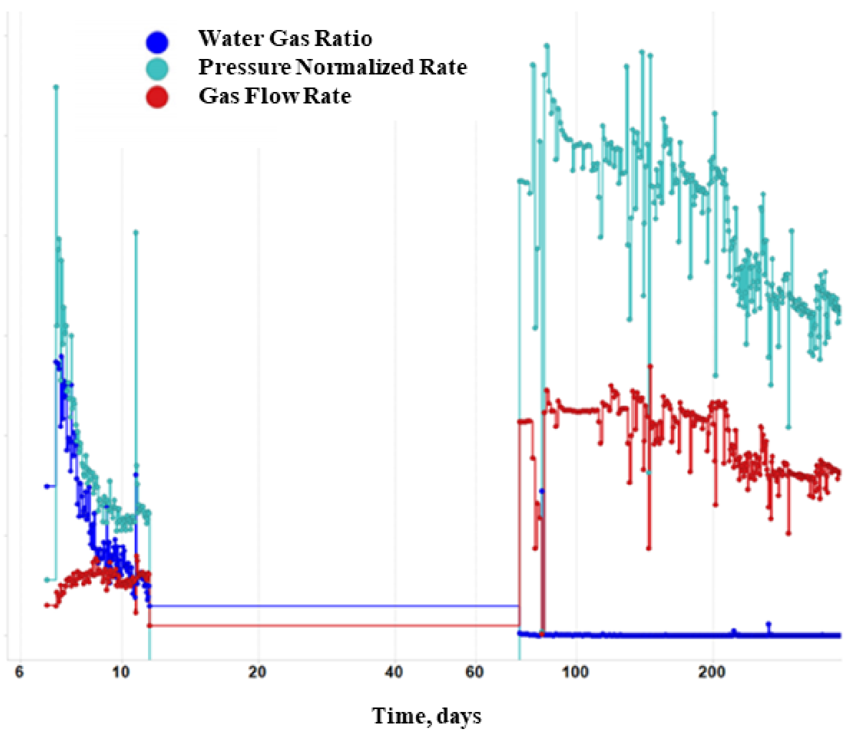

Figure 1.11: Production profile of a Marcellus well with extended shut-in period. After 70 days shut-in, the gas rate increased 4.4 times, and the pressure normalized gas rate increased fivefold (Yaich et al., 2015).

However, some operators observe significant increase in hydrocarbon production after extended shut-in of the wells. Figure 1.11 shows a Marcellus well with an extended shut-in period due to the unavailability of a gas pipeline (Yaich et al., 2015). After extended shut-in, the gas flow rate increases 4.4 times and the pressure normalized gas rate increases fivefold. The flow gas rate remains higher than that before shut-in period even after 300 days of production. Some researchers believe that extended shut-in may enhanced early-time hydrocarbon production due to counter-current imbibition (Dehghanpour et al., 2012, 2013; Makhanov et al., 2014) and osmotic forces (Fakcharoenphol et al., 2013).

1.1.7 Flowback

After shut-in, the fractured wells are opened for well cleanup and subsequent production. Part of the injected fracturing fluids are returned to the surface during a short period called "flowback". Flowback usually lasts for several days, but can be as long as 3-4 weeks. Besides the original fracturing fluids, the recovered fluids may also contain formation fluids and minerals, and a small amount of injected proppants. For shale gas reservoirs, it is reported that only 15-30 % of the total injected fracturing fluids can be recovered during flowback period (Wattenbarger and Alkouh, 2013).

In recent years, the rate, pressure, and salinity profiles of the recovered fracturing fluids are recorded during flowback. It is believed that flowback data contains critical information on the stimulated reservoir and the induced fracture network. Therefore, analysis of flowback data provides the earliest opportunity for reservoir and fracture characterization (Bearinger, 2013).

1.1.8 Fracture Network

During hydraulic fracturing, fracture monitoring techniques (such as microseismic surveillance) are usually adopted to track the fracture propagation process. Microseismic monitoring, which records the seismic events generated during the fracturing treatment, suggests that a complex fracture network is usually developed in gas shales. The complexity of the fracture network partly attributes to the pre-existing natural fractures, which could be re-activated in the process of hydraulic fracturing (Fisher et al., 2004; 2005). Figure 1.12 shows a microseismic image of a well pad in the HRB. The different colors represent the seismic signals received in the fracturing operations of different wells. The microseismic “clouds” overlap each other, indicating the complexity of the induced fracture network.

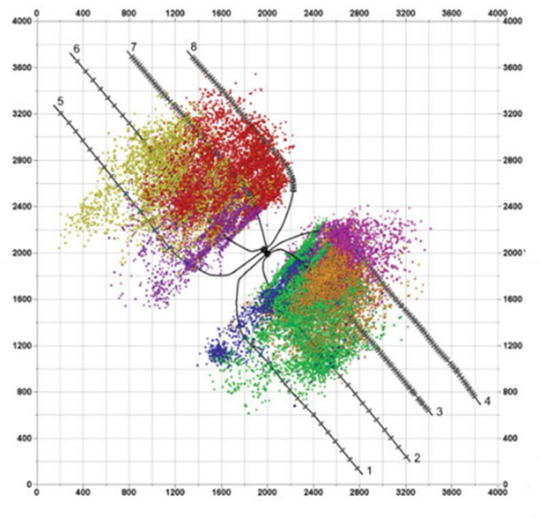

Figure 1.12: Microseismic event locations recorded during the fracturing of a well pad in the Horn River Basin. The x- and y-axis are in the unit of [m] (Virues et al., 2016).

1.1.8.1 Hydraulic Fractures

When the pressurized fracturing fluids are injected into the target formation, hydraulic fractures will be created underground. The pressure required to create hydraulic fractures depends on the in-situ stress conditions as well as the rock strength. Figure 1.13 shows a typical pressure profile during hydraulic fracturing operations. It is usually believed that when the pumping pressure exceeds the breakdown pressure, hydraulic fractures are created. Breakdown pressure is the minimum in-situ stress (usually minimum horizontal stress) plus the tensile strength of the reservoir rock.

Once initiated, the hydraulic fractures propagate along the direction of maximum horizontal stress (i.e. fracture plane is perpendicular to the direction of minimum stress). Figure. 1.14 shows the directions of the hydraulic fractures in different in-situ stress conditions.

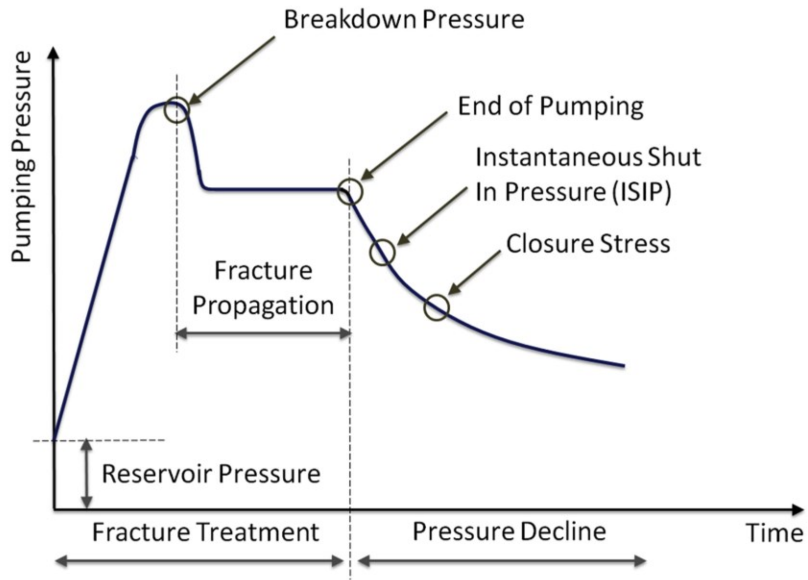

Figure 1.13: A typical pressure profile during hydraulic fracturing operations (Prabhakaran et al., 2017).

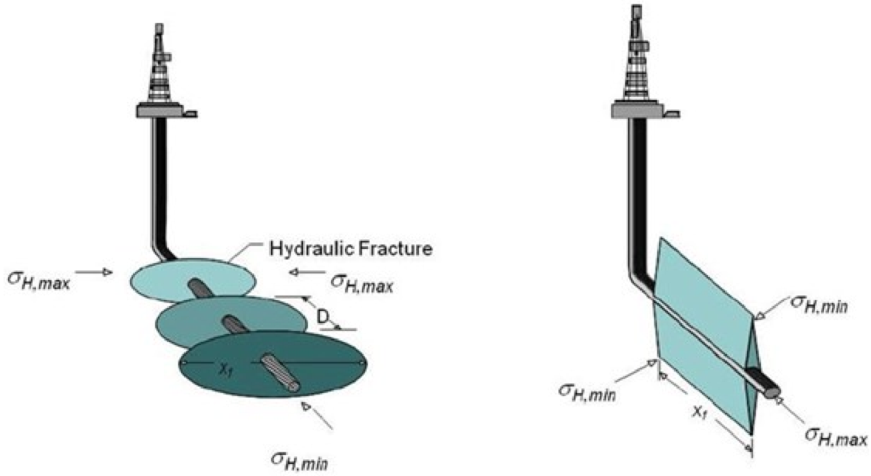

Figure 1.14: The direction of the hydraulic fractures depends on the in-situ stress conditions. Theoretically, the fracture plane is perpendicular to the minimum horizontal stress direction (Salah, 2016).

1.1.8.2 Natural Fractures

In this study, natural fractures refer to the planar discontinuities that pre-exists in rocks before drilling or any operations. Natural fractures are formed due to the stress change associated with tectonic events, and their directions reflect the paleostress conditions (Rezaee, 2015). Natural fractures are ubiquitous in shales. Figure 1.15 shows the natural fractures in outcrops and in the shale samples. Natural fractures in shale are commonly developed in sub-parallel arrays or “sets”, with a minimum two sets observed on a regional scale (Gale et al., 2014). Natural fractures have different compositions and sizes, and may be filled or partially filled with minerals (such as calcite, quartz, and dolomite).

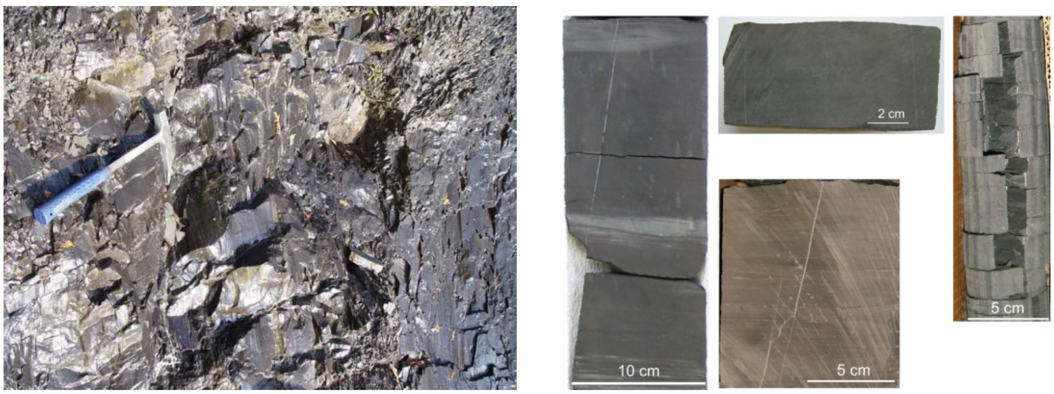

(a) (b)

Figure 1.15: Natural fractures in (a) shale outcrops; and (b) core samples.

Natural fractures affect the propagation of the fracture network during the hydraulic fracturing process of shales (Zhang et al., 2009). Figure 1.16 shows the possible scenarios when a hydraulic fracture encounters a pre-existing natural fracture. The hydraulic fracture could re-activate, dilate, or cross the natural fracture, depending on the opening mode of the natural fracture, the approaching angle between the two fractures, as well as the injection rate and viscosity of fracturing fluid (Cheng et al., 2015; Maxwell 2011). Deformation along natural fractures is one of the reasons responsible for the complex microseismic patterns and the irregular fracture network underground (Gale et al., 2014).

There are debates about the effect of natural fractures on hydrocarbon recovery of the hydraulically-stimulated reservoir. On one hand, natural fractures provide conduits for fluid flow, and increase the permeability of the shale rocks by connecting the hydraulic fractures and the rock matrix. Therefore, they enhance the hydrocarbon recovery. This argument is supported by the field data from the Antrim (Curtis, 2002) and the Marcellus shales (Engelder et al., 2009). On the other hand, natural fractures may hinder the growth of hydraulic fractures by capturing the injected fracturing fluids and dissipates their energy. Simulation studies show that the hydraulic fractures are longer in areas with no natural fractures; but becomes shorter and segmented in areas with well-developed natural fractures (Younes et al., 2011).

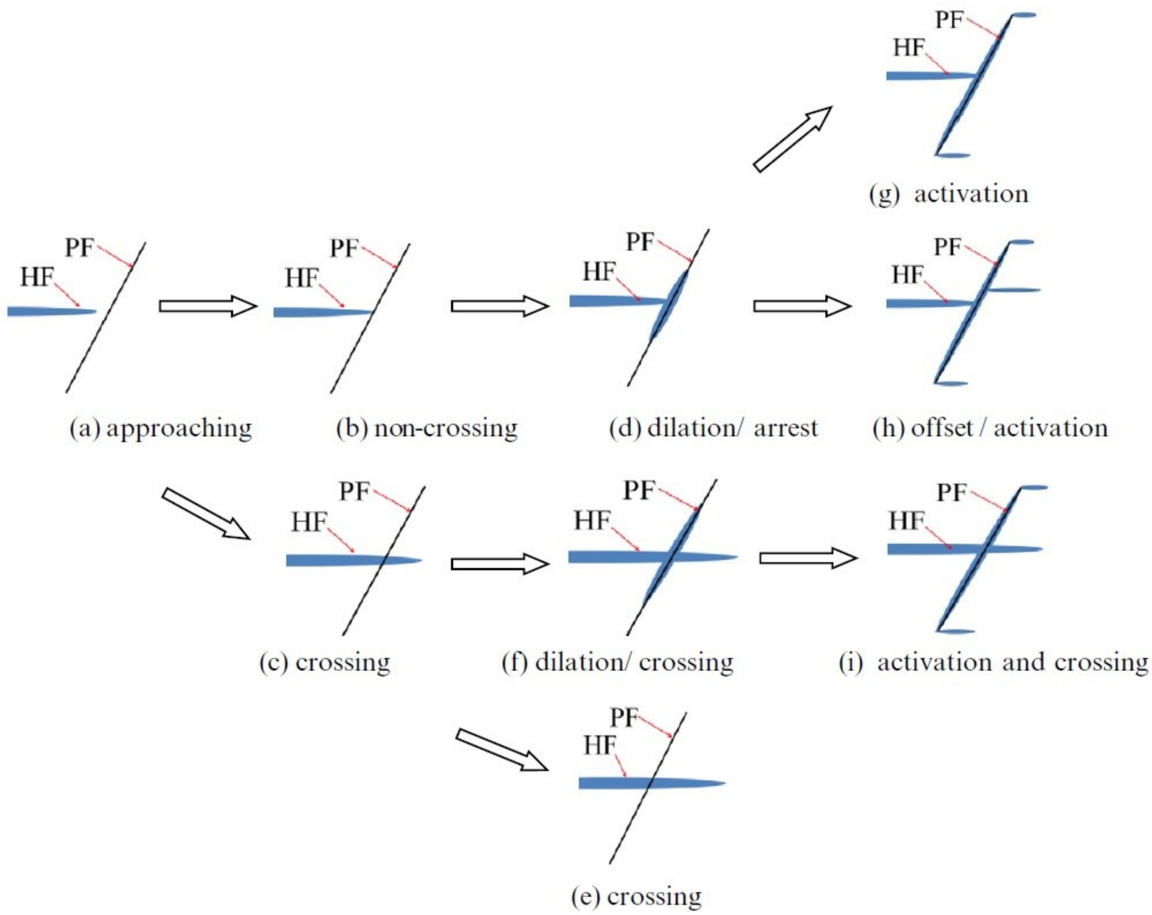

Figure 1.16: Possible scenarios when a hydraulic fracture (HF) encounters a pre-existing natural fracture (PF) in gas shales (Cheng et al. 2015).

Gale et al. (2014) analyzed the sizes of the natural fractures in cores and outcrops from six shale plays. Figure 1.17 shows the distribution of kinetic aperture and height and of the natural fractures analyzed. Kinetic aperture is the distance between the opposite fracture surfaces, including cements and pores. The results show that most natural fractures in shales have kinematic aperture between 30 µm and 1 mm; while the fracture height (measured in cores) ranges from <1 cm to 1.8 m.

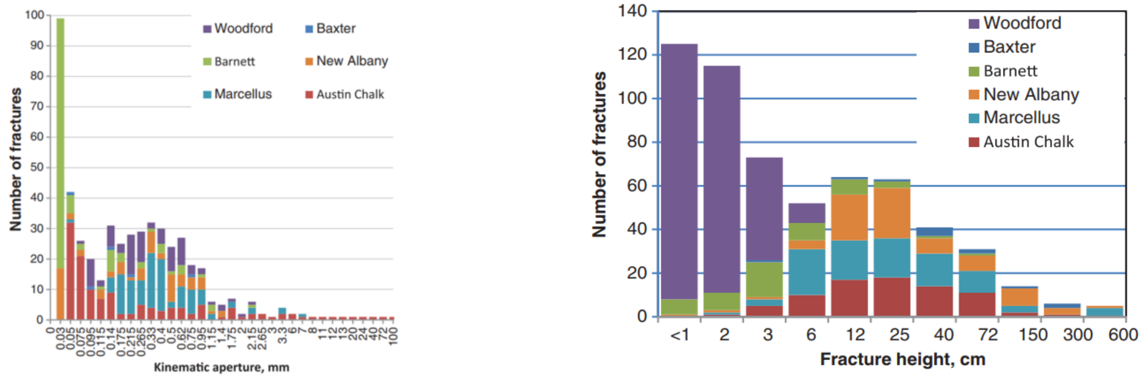

(a) (b)

Figure 1.17: (a) Kinematic aperture and (b) Fracture height distribution of the natural fractures from six shale plays (Gale et al., 2014).

1.2 Research Gap

The research gaps are summarized as follows:

1. The flowback data, although regularly recorded in field practices, are often neglected in conventional production data analysis (i.e. pressure/rate transient analysis) and are seldom used for fracture/reservoir characterization and recovery forecast of gas shales.

2. Despite the large amount of fracturing fluids injected, multi-phase (water + gas) flowback has been observed and reported in many shale gas wells, especially the ones with extended shut-in periods. However, the reasons behind the multi-phase flow signature is poorly understood.

3. Although several models exist for characterizing the stimulated reservoir using multi-phase production data, they usually assume simple fracture geometry (such as planar, bi-wing, identical fractures). However, the induced fracture network after hydraulic fracturing does not follow a regular pattern. Different types of fractures, such as hydraulic fracture, secondary fractures, and natural fractures, contribute to fluid flow and are effective for hydrocarbon

production. There is currently lack of understanding of the effective fracture network for hydraulically-stimulated wells.

4. One approach commonly used in literature to estimate fracture compressibility is based on experimental studies on carbonates (Aguilera, 1999). This approach cannot be applied to fractured unconventional reservoirs due to its lack of proppant consideration. Hence, there are little to no practical models for estimating compressibility of fracture networks in hydraulically-fractured reservoirs.

1.3 Research Objectives

The main objective of this study research is to provide a protocol for fracture/reservoir characterization in shale gas reservoirs by using flowback rate and pressure data. The specific objectives of this research, which corresponds to the four research gaps in Section 1.2, are listed below.

1. Propose practical techniques (such as workflows) for reservoir/fracture characterization in hydraulically-fractured reservoirs by using rate and pressure data during flowback period.

2. Investigate the flow regimes and investigate fluid flow physics behind the multi-phase flow signatures observed in the shales gas wells.

3. Develop mathematical models to estimate key reservoir and fracture parameters in hydraulically-fractured shale gas reservoirs by using flowback data. The proposed models should release the regular fracture geometry assumption and account for multi-phase flow signatures.

4. Propose practical models to estimate the fracture compressibility for hydraulically-fractured shale gas reservoirs. The proposed models should account for proppants in the fractures and the natural fractures in the fracture network.

1.4 Thesis Structure

This thesis has seven chapters, including overview (Chapter 1), four key topics (Chapter 2 to 6), and conclusion and recommendation (Chapter 7). The contents of Chapters 2 to 5 have been published as peer-reviewed journal articles. Therefore, there might be some repetitive texts or figures in these chapters. A modified version of Chapter 6 is currently under review in a peer-reviewed journal. To maintain consistency and prevent redundancy, some contents in the original journal articles have been slightly modified.

Chapter 1 presents an overview of this study. It introduces the key terminologies in this thesis, describes the research gaps, and states the research objectives.

Chapter 2 presents a comprehensive qualitative analysis to understand the fluid flow physic during flowback period. It introduces the target reservoir and the well pad, analyzes the real-time flowback data, investigates flow regimes using diagnostic plots, validates the observed flow regimes using a commercial numerical simulation software, and interprets the fluid flow physics during flowback period. Based on the qualitative analysis, a material balance concept for the fracture network is proposed. This concept forms the basis of this study.

Chapters 3 to 5 propose material balance models to quantitatively characterize the effective fracture network by analyzing the rate and pressure data during flowback period. Besides, the estimated fracture parameters are analyzed and compared through a comparative analysis to help understand the induced fracture network.

Chapter 6 introduces a mathematical model to estimate fracture compressibility for hydraulically-fractured reservoirs. Sensitivity analysis are conducted to investigate 1) the effect of proppant parameters on the fracture compressibility and 2) the roles of unpropped and propped fractures during the fracture closure process.

Chapter 7 summarizes the key results and main conclusions of this study. It also provides the recommendations for future work.

Chapter 2: Understanding the Fluid Flow Physics for Two-Phase Flowback in the Horn River Shales Gas Wells

This chapter comprises 1) diagnostic analysis of the rate and pressure data during flowback period of an eight-well pad completed in the HRB, 2) numerical validation of the observed flowback regimes, and 3) qualitative interpretation of different drive mechanisms in different flow regimes. The contents of this chapter have been previously published in two journal articles (Xu et al., 2015; 2016a). They are combined as an independent chapter here for conciseness and easy understanding of this thesis. I was responsible for analyzing field data, forming key concepts, writing and editing manuscripts. My co-authors assisted in identifying flow signatures, reviewing manuscripts, and securing company approvals for publication.

2.1 Introduction

Shale gas has gradually become an important source of hydrocarbon due to the dwindling supply of hydrocarbon from conventional reservoirs and the rapidly increasing energy demands. The United States and Canada are reputed to have technically recoverable shale gas reserves of up to 623 Tcf and 573 Tcf, respectively (EIA, 2015). A combination of horizontal well technology and hydraulic fracturing has made exploitation of these reserves possible. After drilling the horizontal wells, the pressurized fracturing fluids are injected into the wells to create fractures. These fractures significantly increase the permeability of shale reservoirs. Part of the fracturing fluids are recovered during a post stimulation period known as “flowback”. Although this flowback data is usually discarded in conventional production data analysis, it actually presents the earliest opportunity for reservoir characterization, production forecast, and gaining useful insights on improving hydraulic fracturing designs.

Abbasi (2013) and Abbasi et al. (2014) presented a series of diagnostic plots that separate flowback data of tight oil/gas reservoirs into three distinct regions. The first region is single-phase water flow which occurs during very early periods. Interestingly, flowback data from Horn River (HR) shales do not show this single-phase region. Instead, they show two-phase (gas + water) production once the wells are opened (Abbasi, 2013; Ghanbari et al., 2013). This immediate two-phase flow behavior is also reported in the Barnett (Zhang and Ehlig-Economides, 2014) and the Marcellus shales (Clarkson and Williams-Kovacs, 2013), and can be viewed as a unique behavior of gas shales. However, the mechanisms responsible for this instant gas production is poorly understood.

The Gas Water Ratio (GWR) plot for analyzing tight reservoirs was first presented by Ilk et al. (2010). It has been used to identify the flow regimes and drive mechanisms in shales. Zhang and Ehlig-Economides (2014) analyzed data from 32 wells completed in the HR and Barnett shales. They reported slope changes in the Water Gas Ratio (i.e. inverse of GWR) plots and separated the data into two distinct flow regions: the negative half slope signifying “drainage” followed by a negative unit slope signifying “vaporization”. Abbasi (2013) and Ghanbari et al. (2013) observed a V-shape trend in the GWR plots from similar well pads in the HRB. Based on this V-shape signature, Adefidipe et al. (2014) divided the flowback data in the HR shales into two regimes: 1) Early Gas Production (EGP), which is characterized by a decreasing GWR trend; and 2) Late Gas Production (LGP), which is characterized by an increasing GWR trend. They hypothesized that the EGP phase indicates free gas depletion from the fracture network, while the LGP phase occurs once significant gas saturation builds up in the secondary fractures connected to the primary (hydraulic) fractures. However, this hypothesis is yet to be validated.

This chapter qualitatively interprets the flowback rate and pressure data collected from an eight-well pad completed in the HRB. Also, it seeks to understand the fluid flow physics behind the immediate two-phase production observed in these wells. The rest of this chapter is organized as follows. Section 2.2 introduces the HRB and target well pad. Section 2.3 constructs diagnostic plots to capture flow regimes during flowback. Section 2.4 builds a numerical model in a commercial simulation software to validate these flow regimes and investigate the drive mechanisms in different flow regimes. Based on these results, Sections 2.5 and 2.6 proposes a material balance concept for flowback data analysis and pictorially illustrate this concept. Finally, Section 2.7 summarizes the key results from this chapter. 2.2 Reservoir and Well Pad Description

The focus of this study is an eight-well pad drilled and completed in the HRB. This section briefly introduces the HRB and the target well pad.

2.2.1 Horn River Basin

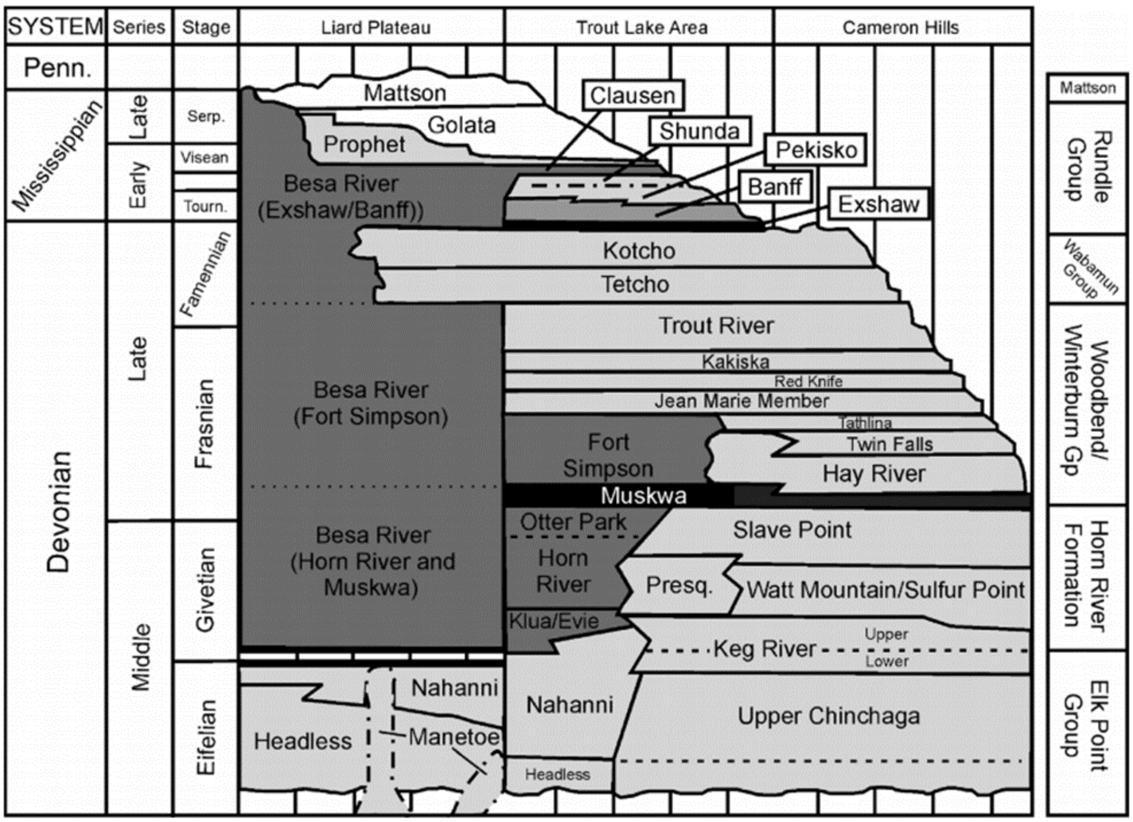

Figure 2.1: Stratigraphic section of Devonian-Mississippian strata (Ross and Bustin, 2008).

HRB is located in the northeastern part of British Columbia and extends into the northwest territories of Canada (Johnson et al., 2011). It is one of the largest unconventional resources in Canada with estimated technically recoverable natural gas resource of 133 Tcf (EIA, 2015). Figure 2.1 shows its stratigraphic section: it is of Devonian age and belongs to the Western Canada Sedimentary Basin. HRB consists of three shale members: the Muskwa (MU) at the top, the Otter Park (OP) in the middle and the Evie (EV) at the bottom. The fluid composition is dry gas comprised mainly of methane (> 85 %) and CO_2 (10-12 %) (B.C. Oil & Gas Commission, 2014). Mineralogy studies suggest that the HR shales consist of 44-60 % quartz, 1-25 % calcite, and 11-

26 % illite (Virues et al., 2016b). Due to the high quartz content, the HRB shales show high brittleness and have a large amount of pre-existing natural fractures (EIA, 2015).

2.2.2 Target Well Pad

Figure 2.2 schematically illustrates the target well pad, which includes eight wells completed in the MU and OP shale members of the HRB. Four wells are drilled in each bank of the pad. This is a pilot pad drilled and completed in 2010. Multi-stage hydraulic fracturing is performed in all eight wells. Each horizontal well is isolated into different sections called stages and is stimulated in sequence from toe (i.e. the stage farthest from well head) to heel (i.e. the stage nearest to the well head). For all eight wells, each stage is designed to be 100 m. Single (1 cluster/stage) or multiple (4 clusters/stage) perforations were applied on different wells, as schematically shown in Figure 2.3. After stimulation, all wells were shut for an extended period. Shut-in time refers to the time after well completion and before flowback. The left half-pad has shorter shut-in time (72-106 days) compared with the right half-pad (107-132 days). Table 2.1 summarizes the completion design parameters for the target pad, including target formation, horizontal well length, number of stages, number of perforation clusters per stage, total injected volume (TIV), and shut-in time.

Table 2.1: Summary of completion design parameters of the target pad in the HRB.

Well ID	Formation	Well Length (m)	Number of Stages	Perforation Clusters per Stage	TIV (m^3)	Shut-in Time (days)
A	OP	1,500	15	4	60,590	106
B	MU	1,700	17	4	66,246	76
C	OP	1,900	20	1	75,504	84
D	MU	1,400	15	1	69,673	72
E	OP	1,970	20	4	54,217	112
F	MU	1,500	15	4	43,927	132
G	OP	1,900	20	1	58,678	107
H	MU	1,600	17	1	54,217	112

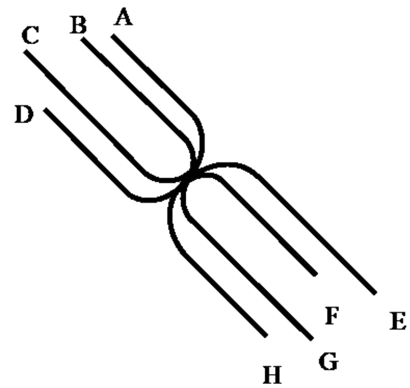

Figure 2.2: Plan view of the target well pad completed in the MU and OP members of the HRB.

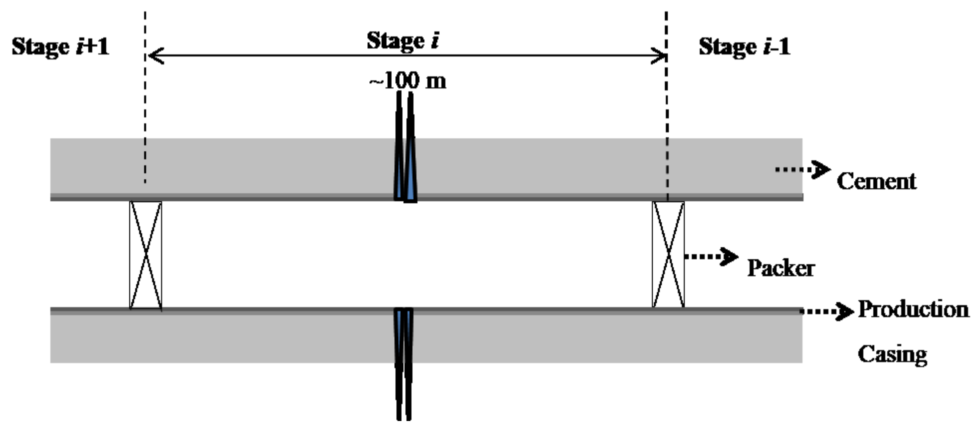

(a)

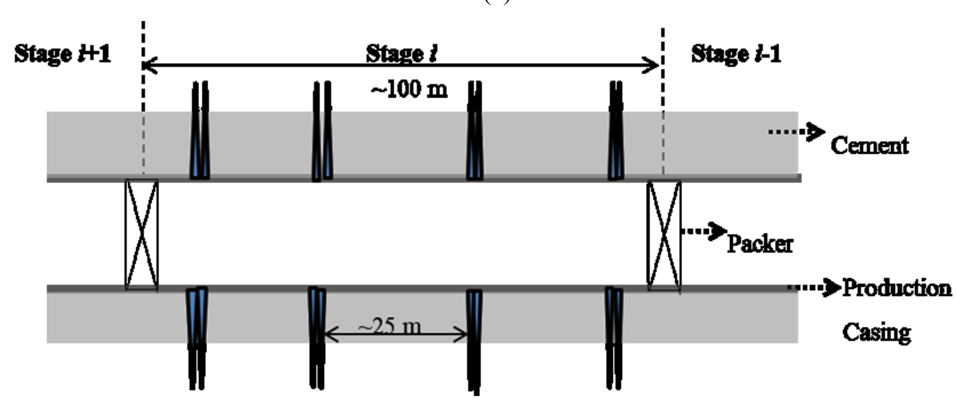

(b)

Figure 2.3: Schematic of (a) single (1 cluster/stage) and (b) multiple (4 clusters/stage) perforation strategies applied on the target well pad (modified from Virues et al., 2015).

2.3 Diagnostic Plots

Ilk et al. (2010) suggested a workflow to analyze flowback data in tight/shale reservoirs, which includes generating diagnostic plots of production rates (gas + water) and GWR from flowback data. Following Ilk's procedure, this section constructs the production rates and GWR plots of the target wells to identify flow regimes during flowback period.

2.3.1 Gas and Water Production Rates

Figure 2.4 shows gas and water production rates in the first 200 hours for the eight wells studied. A surprising trend of immediate gas breakthrough is observed in the production rate plots.

Previous studies show that the immediate gas breakthrough is mainly due to 1) an extended shut-in period for this particular well pad, 2) the possibility of strong counter-current water imbibition into the HR shales (Dehghanpour et al., 2012, 2013; Makhanov et al., 2014), and 3) the initial gas in the pre-existing natural fractures.

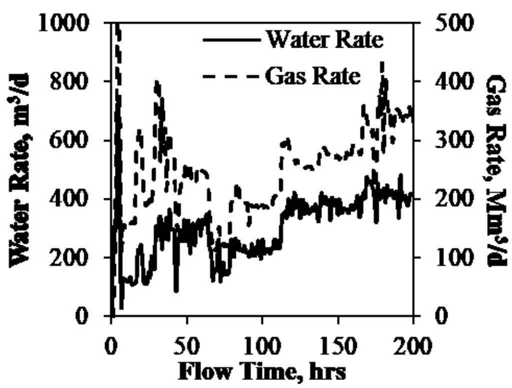

(a)

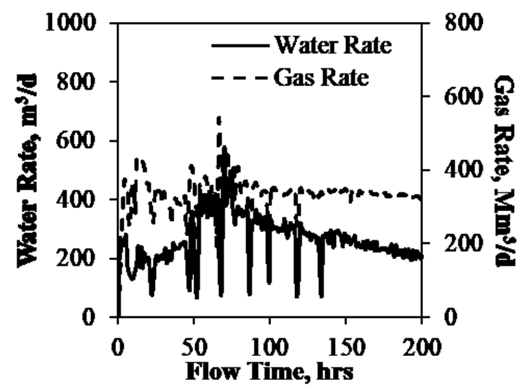

(b)

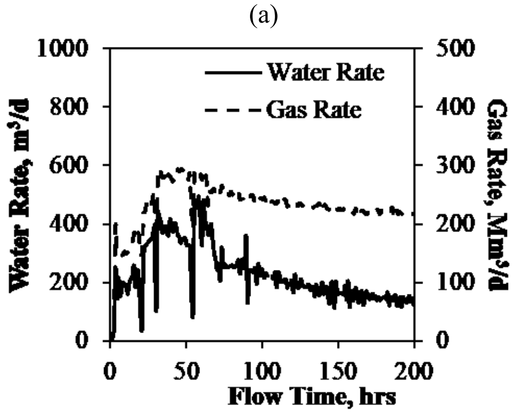

(c)

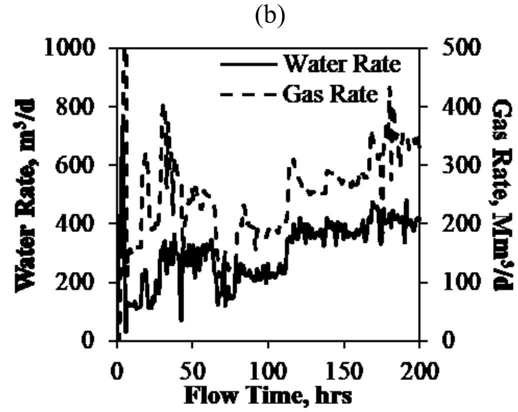

(d)

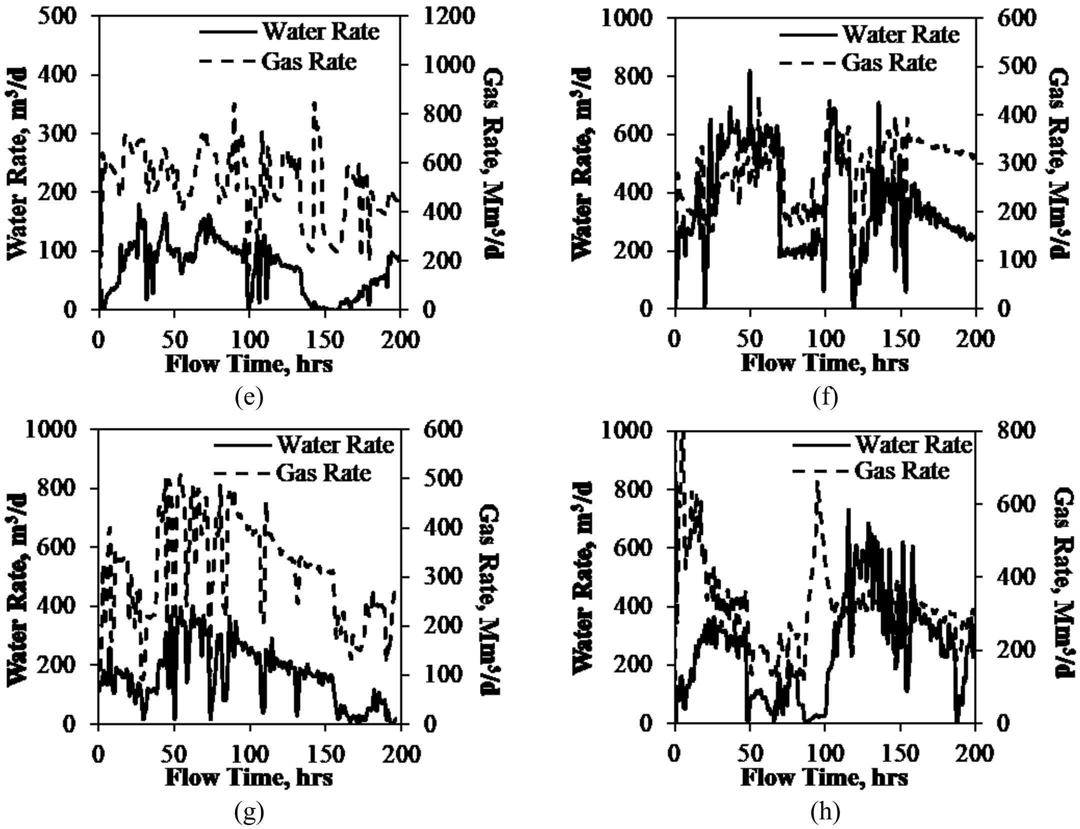

Figure 2.4: Early-time (First 200 hrs) production rates (gas + water) for the target pad in the HBR. The plots show immediate two-phase (gas + water) flow for all wells. Plots (a) to (h) correspond to Wells A to H, respectively.

2.3.2 Producing Gas Water Ratio

Figure 2.5 shows the GWR vs. cumulative gas production (G_p) for the wells considered. Generally, a striking V-shape behavior is observed in the GWR plots: It is characterized by a decreasing/negative sloping GWR curve at first, immediately followed by an increasing/positive sloping GWR trend. In the pad analyzed, five wells (Wells A to E) show remarkable V-shape trend; Well G shows a delayed V-shape response; Wells F and H show a sudden "jump" in the V-shape GWR. The V-shape GWR has also been reported in similar wells in the HRB (Abbasi, 2013; Ghanbari et al., 2013). A similar trend is also observed in the GWR vs. time plots (Adefidipe et al., 2014).

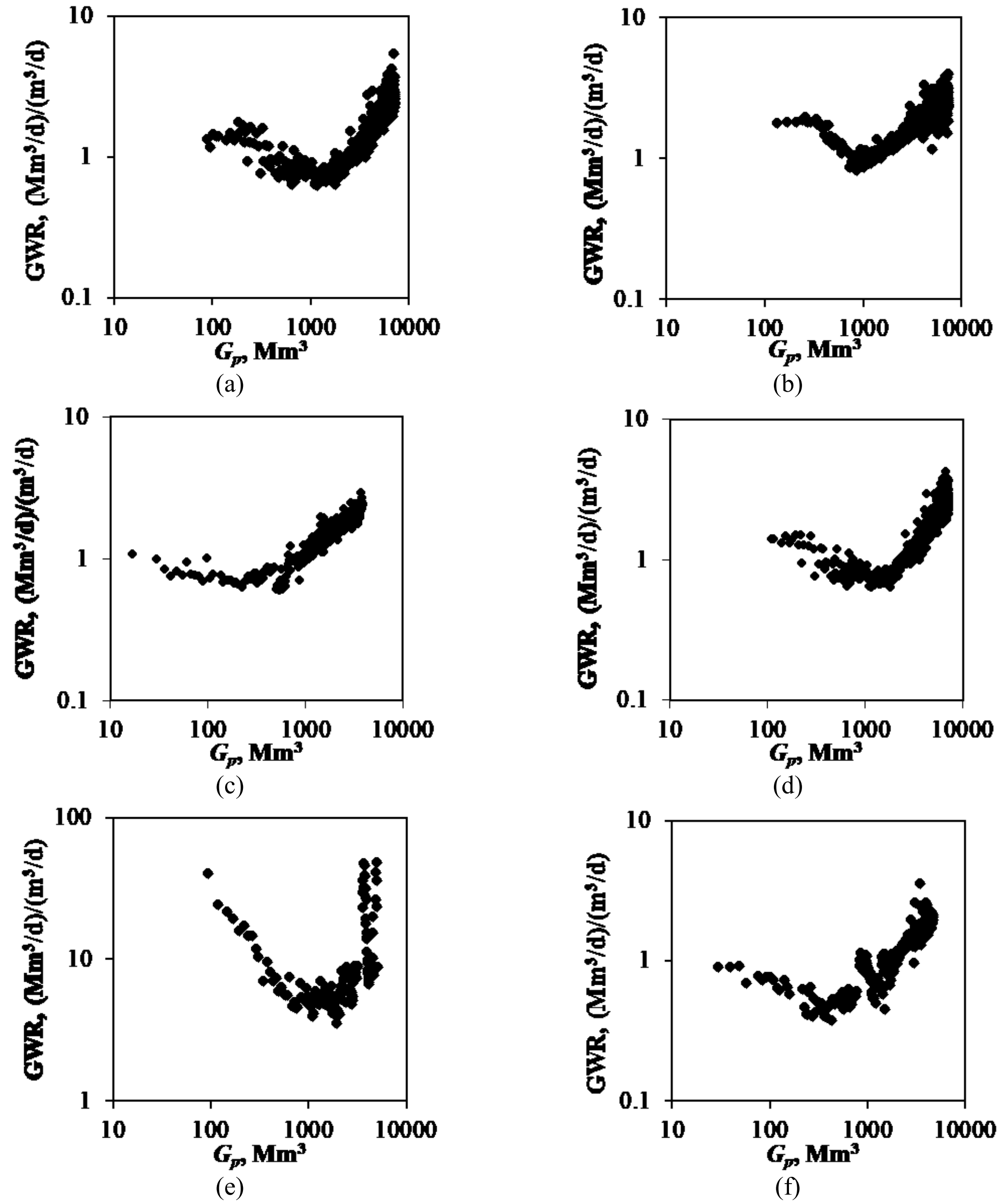
GWR, (Mm³/d)/(m³/d)
G_p, Mm³
10
1
0.1
100
10000
1000
(a)
(b)
(c)
(d)
(e)
(f)

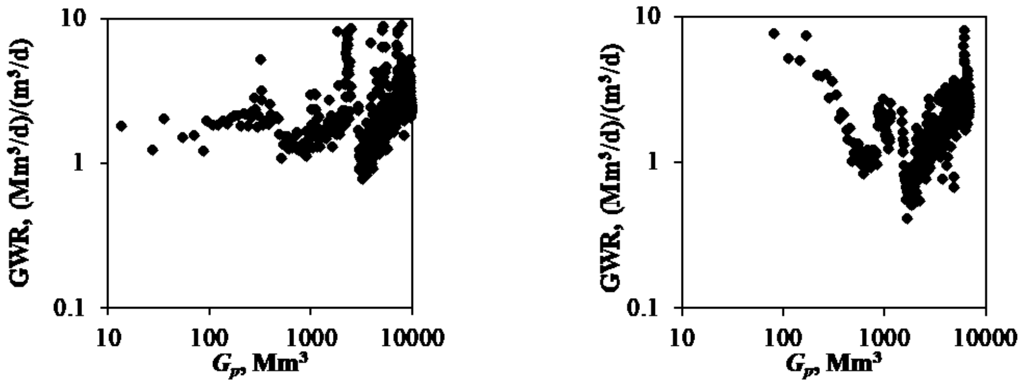

(g) (h)

Figure 2.5: Diagnostic GWR plots for the target pad in the HRB. The GWR plots show a striking V-shape trend for all wells. Plots (a) to (h) correspond to Wells A to H, respectively.

2.4 Observations from Numerical Model

Flowback data usually show rapidly fluctuating rates, especially during the first few hours. This is usually due to frequent changes in choke sizes at the beginning of flowback. To ensure that the observed flow signatures in Section 2.3 is not an artifact of the poor data quality or the changes in choke sizes, a numerical model is built using the Computer Modeling Group (CMG) software to simulate shut-in and flowback operations. The simulation model also aims to investigate the reasons behind the immediate two-phase flow signatures.

2.4.1 Model Configuration

The numerical model is built in the CMG software following the approach presented by Cheng (2012a) who simulated a similar process. It takes advantage of the symmetrical configuration and simulates a quarter of the reservoir volume around two hydraulic fractures. Figure 2.6 shows the 3D view of the numerical model: it has the dimensions of 61 m in x-direction, 110 m in y-direction and 17 m in z-direction, as shown in. The fractures are perpendicular to the horizontal wellbore with a spacing of 30.5 m and half-length of 110 m. CMG uses finite volume method to solve the fluid flow equations in the porous media.

Basic reservoir and fracture properties are listed in Table 2.2. The fracture conductivity of the simulation model is set to be 59 md-ft based on the experiment results in Barnett shales (Zhang et al., 2014). Gas properties and capillary pressure used in the model are described in Figure 2.7.

The capillary pressure curve used for shale matrix is generated based on an empirical correlation presented by Eq. 2.1 (Gdanski et al., 2009). The relative permeability curves used to describe fluid flow through fractures and shale matrix are similar to the previous simulation study by Cheng (2012a). The numerical simulation also accounts for the effects of water imbibition and gravity segregation.

$$P_c = \frac{\sigma}{a_2(S_w)^{a_1}}\left(\frac{\phi}{k}\right)^{a_3} \tag{2.1}$$

where P_c is capillary pressure. σ is surface tension; S_w is water saturation; ϕ is porosity; k is absolute permeability. a_1, a_2, and a_3 are adjustable constants. For a porous medium with porosity of 0.08, a_1 = 1.86, a_2 = 6.42, and a_3 = 0.50.

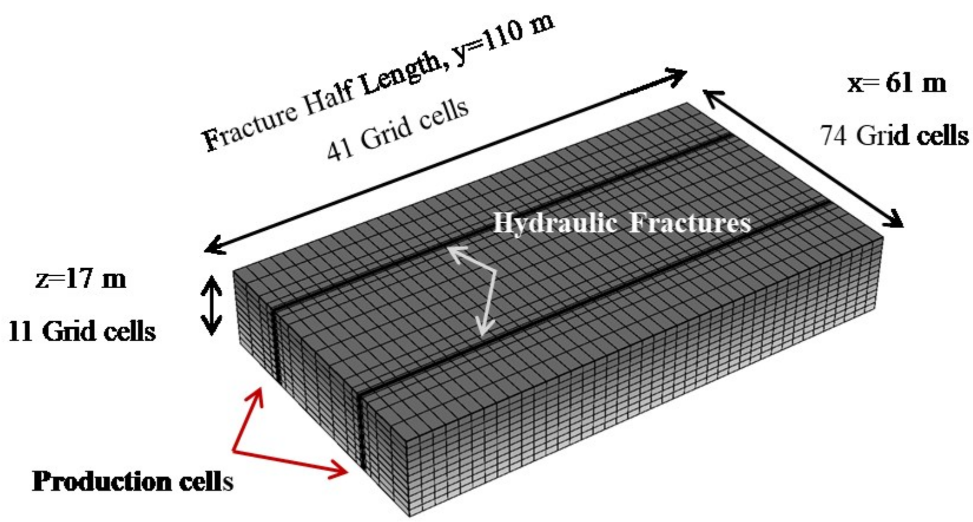

Figure 2.6: 3D view of the numerical model used for simulating shut-in and flowback processes.

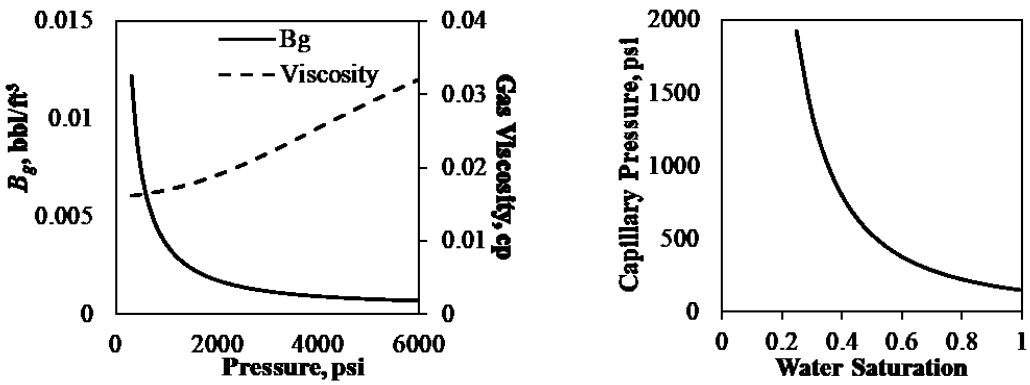

(a) (b)

Figure 2.7: (a) Gas PVT and (b) capillary pressure curves used in the simulation model.

Table 2.2: Reservoir and fracture properties for the numerical model.

Parameter	Value	Unit
Matrix Permeability	0.0005	mD
Fracture Permeability	2000	mD
Matrix Porosity	8	%
Fracture Porosity	60	%
Fracture Aperture	0.9	cm
Fracture Conductivity	59	md-ft
Initial Reservoir Pressure	3000	psi

2.4.1.1 Water Imbibition

When the water injected during hydraulic fracturing treatment contacts the shale matrix, the water can imbibe into the rock matrix and affect the reservoir/well production performance. The imbibition process is mainly controlled by the capillary pressure, which is a function of rock pore structure, wettability, interfacial tension, and initial fluid saturations. In low permeability reservoirs, the capillary pressure can be several hundred psi or even higher (Holditch, 1979). Therefore, the imbibition effects are considered to be significant.

2.4.1.2 Gravity Segregation

In thick reservoirs with long vertical fractures, gravity affects water and gas distribution in fractures. During the shut-in period, when gas is expelled into fractures due to counter-current imbibition, water can be separated vertically from gas by gravity segregation (Parmar et al., 2014). In this study, the numerical model is divided into 11 layers to account for the effect of gravity segregation.

2.4.2 Model Initialization

The fractures in the numerical model are initially fully saturated with water. To mimic the fracturing process, 500 bbl of water is injected into the existing fractures to increase the fracture pressure to approximately 7,000 psi, which is close to the fracturing pressure. Then the wells are shut for 54 days before production. To simulate the flowback process, two scenarios for production constraints are considered: a) constant gas rate at 50,000 ft^3/d, and b) constant bottomhole flowing pressure (BHP) at 1,000 psi.

2.4.3 Simulation Results

The simulation results discussed below are consistent with the behavior of the field data presented in Figures 2.4 and 2.5.

2.4.3.1 Saturation Change during Shut-in Period

Figure 2.8a shows gradual build-up of free gas in the fracture plane during the shut-in period in the numerical model. During the simulated fracturing process, the fractures are fully saturated with water. During shut-in, water imbibes into the matrix through both forced and spontaneous imbibition while gas is expelled out from the matrix into the fractures. This causes the increasing free gas saturation in the fracture network. The increasing average gas saturation owes to 1) capillary pressure, which is the driving force for spontaneous imbibition; 2) pressure difference between the fracture network and the matrix system, which causes forced imbibition, and 3) extended shut-in period, which gives sufficient time for the imbibition processes to take place. By the end of the shut-in period, the average gas saturation in the fracture plane reaches about 67 %. Figure 2.8b vividly shows the effects of water imbibition and gravity segregation during shut-in period. Red and blue represent gas saturation of one and zero, respectively. The effect of water imbibition can be observed by comparing the saturation profiles at different times. As shut-in time increase, the water occupied less space and gas occupied more space in the fracture plane. The effect of gravity segregation is shown by gas and water distribution in the fracture plane. At each time step, gas is accumulated at the top of the fracture plane while water is distributed at the bottom due gravity difference.

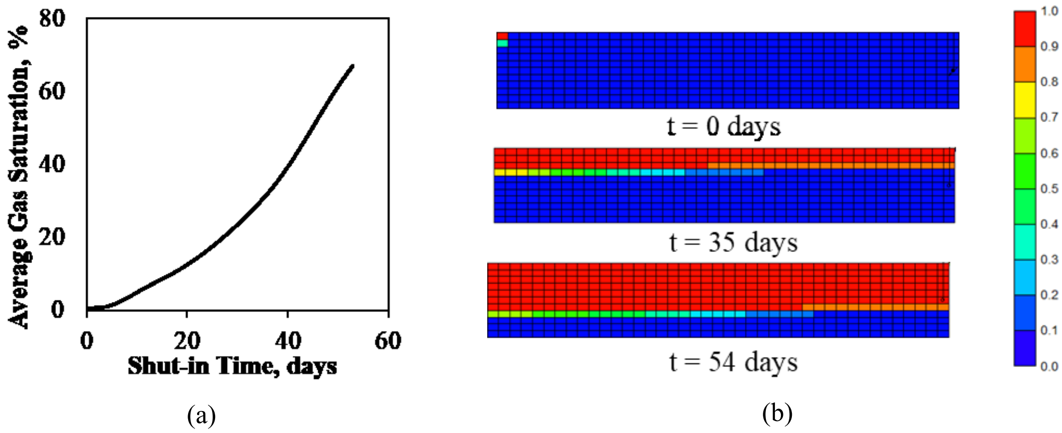

Figure 2.8: Fluid saturation change inside the fractures during shut-in: (a) Average gas saturation increases from 0 to 67 %, and (b) Distribution of water and gas in the fractures at different times during shut-in.

2.4.3.2 Diagnostic Plots of Simulated Flowback Data

Figures 2.9 and 2.10 show the production rates and the GWR plots for the simulated cases. In the constant rate case (Figure 2.9), the gas production rate remains constant during flowback. The water production rate is initially very low and increases gradually until it peaks at about 3.5 bbl/d after 150 hrs. The water rate then declines continuously till the end of the flowback process. In the constant BHP case (Figure 2.10), very high water and gas production rates are observed at the very beginning of flowback. Once the production rates stabilize, they follow the similar trend. The water production rate increases gradually and peaks at about 6 bbl/d after 100 hrs before declining gradually till the end of the flowback process. The gas production rate increases slowly to around 80 Mft^3/d after 350 hrs and slowly declines till the end of the flowback process. In both cases, the V-shape GWR is observed (Figures 2.9b and 2.10b). The simulation results suggest that the V-shape GWR is not an artifact of the noisy field data. The gas/water flow dynamics resulting from the two-phase relative permeability effects is what drives the V-shape GWR behavior observed in both field and simulation cases.

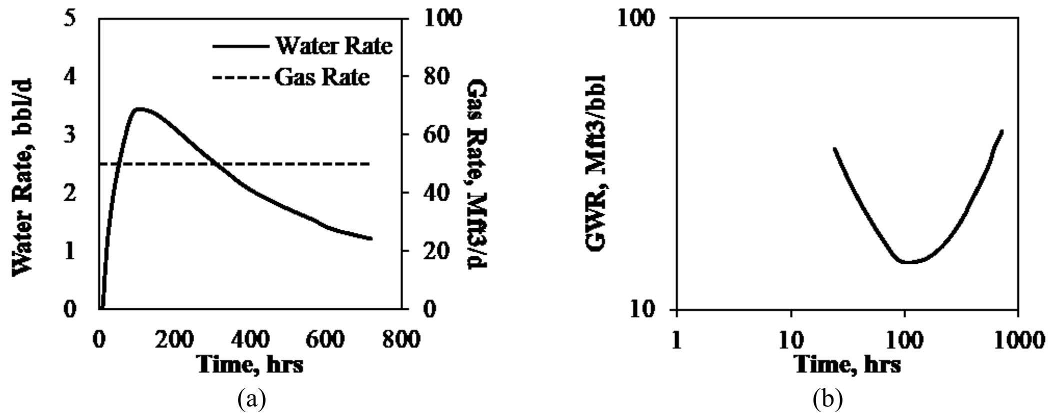

Figure 2.9: (a) Production rates and (b) GWR plots for the constant rate case in the numerical model.

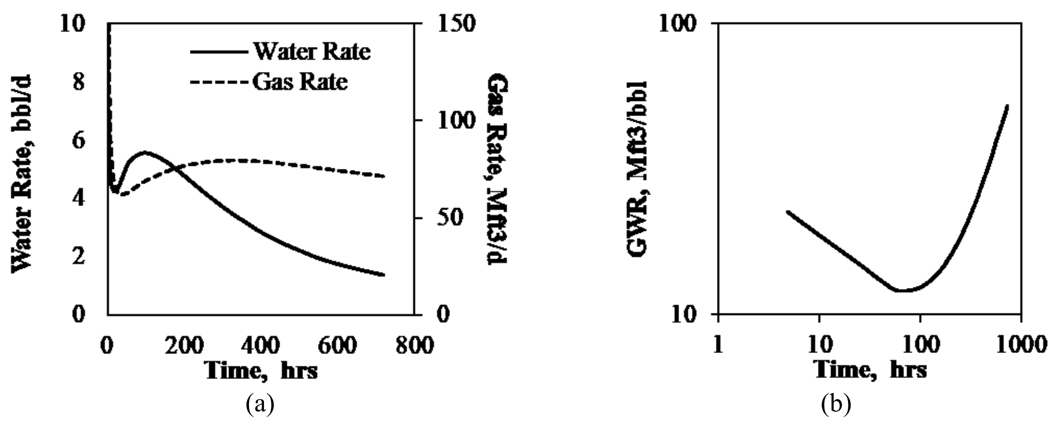

Figure 2.10: (a) Production rates and (b) GWR plots for the constant BHP case in the numerical model.

Figure 2.11 shows that during the flowback process, the average gas saturation in fractures decreases initially, and after reaching to a minimum value, increases gradually, in both constant rate and constant BHP cases. A reverse trend occurs for the water phase since water and gas saturations add up to one. Consequently, gas relative permeability and gas flow rate decrease initially and increase after reaching a minimum value, with the reverse trend occurring for the water phase. This gas saturation change inside the fractures explains the reason for the V-shape GWR behavior observed in both field and simulated cases.

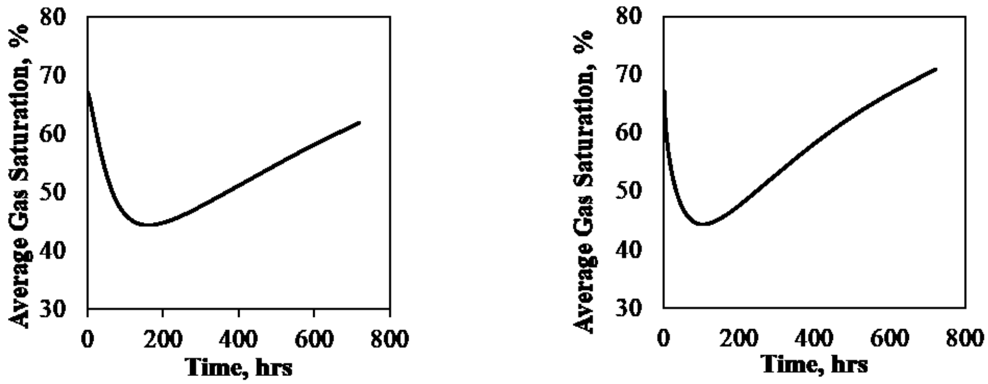

(a) (b)

Figure 2. 11: Change in average gas saturation in fractures during flowback period in the numerical simulation: (a) Constant rate case; and (b) Constant BHP case.

2.5 Flow Regimes

The GWR plots of both simulation and field data show a V-shape trend. Based on this signature, one can separate the flowback data into two distinct regions: 1) EGP, which is characterized by a decreasing GWR, occurs immediately when the wells are opened; and (2) LGP, which is characterized by an increasing GWR, occurs once there is significant gas contribution from the matrix system.

The V-shape GWR can be explained mathematically using Darcy's Law (Eq. 2.2). Assuming negligible capillary force in the fracture network, GWR represents the mobility ratio between gas and water phases:

$$GWR = \frac{q_g}{q_w} = \frac{\mu_w}{\mu_g(P)} \frac{k_{rg}(S_g)}{k_{rw}(S_w)} \frac{\partial p_g}{\partial p_w} \approx \frac{\mu_w}{\mu_g(P)} \frac{k_{rg}(S_g)}{k_{rw}(S_w)} \quad (2.2)$$

where q, μ, k_r, S and P represent production rate, viscosity, relative permeability, saturation, and pressure, respectively. w and g in the subscripts represent water and gas phase, respectively.

2.5.1 Early Gas Production

EGP characterized by a negative slope on the GWR plot. According to Eq. 2.2, after opening the wells, μ_g drops with pressure while μ_w remains relative constant. Thus, the decreasing GWR suggests that k_{rg}/k_{rw} decreases with time. This is in agreement with the simulated production data (Figures 2.9a and 2.10a) showing that water production rate increases gradually at early time. Furthermore, based on the two-phase relative permeability characteristics (i.e. Corey correlation), decreasing k_{rg}/k_{rw} suggests decreasing S_g/S_w. This is consistent with the decreasing gas saturation at early times, observed in Figures 2.11a and 2.11b. In addition, the decreasing gas saturation also suggests that S_{gi} is the maximum gas saturation in EGP region. In other words, there is significant volume of gas saturated in the fractures before opening the wells. This is also backed by the simulation results (Figure 2.8) showing the build-up of gas in the fracture network during the extended shut-in period.

2.5.2 Late Gas Production

LGP is characterized by a positive slope on the GWR plot. This flow regime has been the subject of several papers (Ilk et al., 2010; Clarkson and Williams-Kovacs, 2013; Ezulike and Dehghanpour, 2014a). In conventional production data analysis, this is the first flow regime identified after wellbore storage effects become negligible. Importantly, this flow regime signifies the onset of gas transfer from the matrix into the fracture network. According to Eq. 2.2, gas influx from the matrix system increases the average gas saturation in the fracture network, resulting in an increasing k_{rg}/k_{rw} and consequently an increasing GWR. This signature is also observed in the results from the numerical model. As gas saturation quickly builds up in the fractures, water saturation decreases, resulting in decreasing relative permeability and production rate for the water phase, as observed in Figures 2.9a and 2.10a.

2.6 Material Balance Concept for the Effective Fracture Network

Eq. 2.3 is the MBE for a volumetric gas reservoir. It indicates that a plot of p/Z vs. G_p yields a straight line for a dry gas reservoir where production is driven by the expansion of free gas only (Ahmed, 2010). The x-axis intercept gives the volume of gas initially in place at standard conditions.

$$\frac{p}{Z} = \frac{p_i}{Z_i} - (\frac{p_i}{Z_i G})G_p \quad (2.3)$$

where p_i and p are the initial reservoir pressure and current reservoir pressure, respectively. Z_i and Z are the gas compressibility factor at p_i and p, respectively. G is the origin gas in place. G_p is the cumulative gas production.

Figure 2.12a highlights possible deviations from this straight line relationship for different gas reservoirs such as over-pressured reservoirs, aquifer-supported reservoirs and coal bed methane (CBM) reservoirs (Moghadam et al., 2011). In these reservoirs, the tank volume continuously changes, leading to the deviation of the straight line. Kuchuk et al. (2014) conducted a similar p/Z analysis for naturally fractured reservoirs. The authors identified three different depletion patterns by observing the changes in the slopes of the p/Z plots, as shown in Figure 2.12b. The first flow regime observed is a fracture-dominated pseudo-steady-state flow, which is typically observed in wells with a finite fracture volume where the formation matrix is very tight. During this phase, fluid is depleted from the primary fracture network, with negligible support from the matrix and the minor- and micro-fractures. The x-axis intercept of the straight line represents the initial free gas in the primary fracture network. In cases where there is a significant secondary fracture volume, a second flow regime indicated by a change in the slope is observed. This slope change corresponds to depletion from the minor- and micro-fractures. As the matrix contribution becomes significant, there is another deviation which signifies the beginning of matrix depletion.

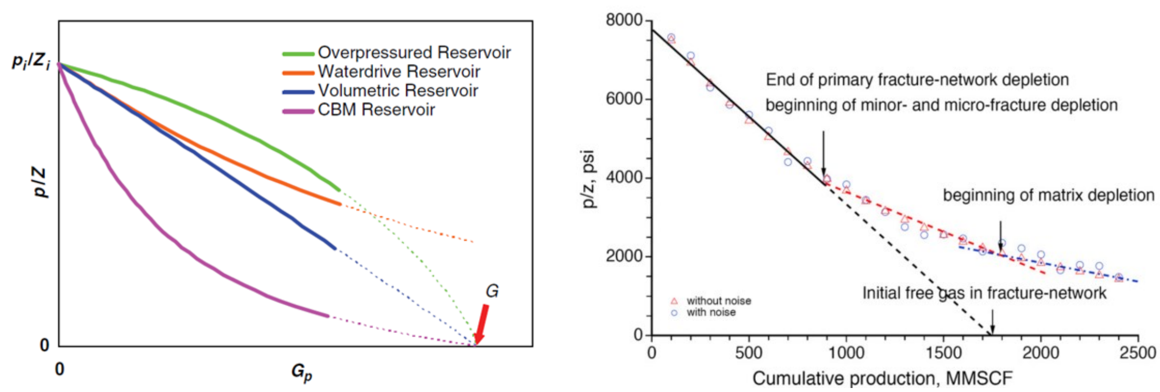

(a) (b)

Figure 2.12: (a) Gas material balance plots (i.e. *p/Z* plots) for different gas reservoirs. *p/Z* plots deviates from the straight line when other drive mechanisms exist (Moghadam et al., 2011); (b) The *p/Z* plot for a naturally fractured reservoir shows three flow regimes with different slopes (Kuchuk et al., 2014).

Figure 2.13 shows the flowback p/Z analysis for the eight wells analyzed in this study. In the p/Z analysis, the calculated BHP is used as p. Generally, a linear p/Z trend with a constant slope is observed during the first few hours of flowback. Well G shows a delayed response again, just as in the GWR plot. The linear p/Z behavior at the beginning of flowback indicates that 1) the fractures can be viewed as a "closed tank" at early times, and 2) gas expansion is the predominant drive mechanism during this phase. Thus, the x-axis intercept of the extrapolated line should give an estimate of the initial free gas volume inside the fracture network (indicated as G_p^* in Figure 2.13). As the flowback process continues into late-time phase, significant amount of gas kicks into the fractures from the matrix system. The closed-tank system assumption no longer applies, and the p/Z plots show a second line with a gradual slope. The change in slope signifies the onset of matrix depletion.

Figure 2.13 also shows another trend in the p/Z plots which may be peculiar to the HR wells. The p/Z plots of four wells (i.e. Wells A, D, F and H) show a "rightward shift" of the initial straight line (shown by arrows in Figure 2.13). This "rightward shift" signatures may be due to the frequent shut-ins of nearby wells. Shutting the nearby wells causes an increase in the pressure of the producing well, which in turn results an increase in the value of p/Z.

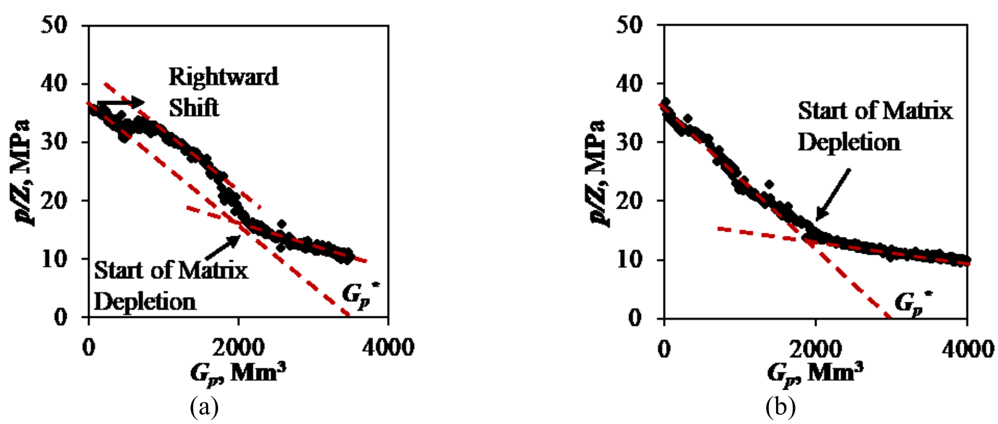

(a)
(b)

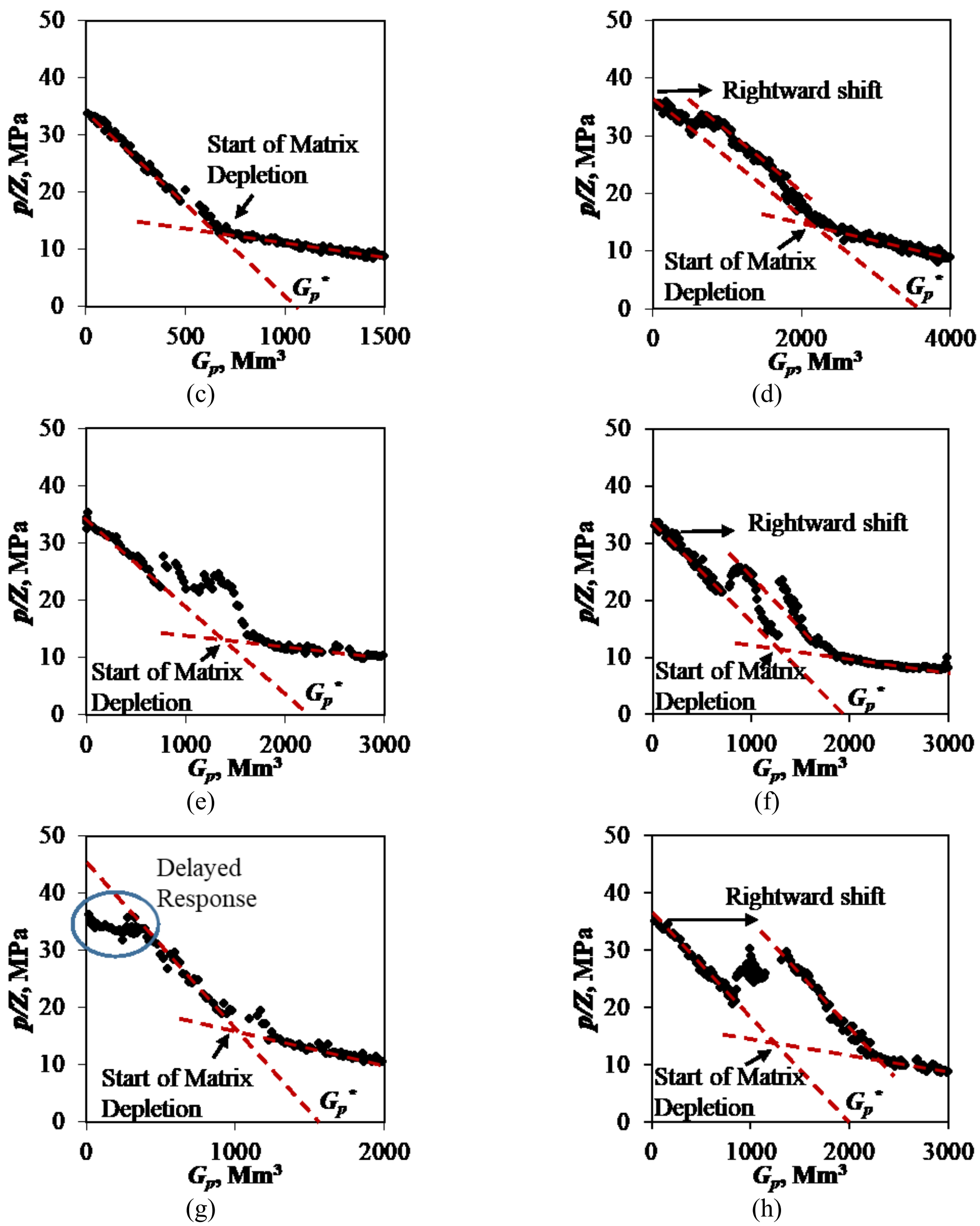

Figure 2.13: ***p/Z*** **analysis of flowback data for the target pad in the HRB. Two lines with different slopes are observed in all wells. The intercept of them indicate the start of matrix depletion. Plot (a) to (h) corresponds to Wells A to H, respectively.**

The signatures on the *p/Z* plots suggest that the effective fracture network can be viewed as a two-phase tank. The tank is isolated from the surrounding matrix system during EGP, while receives pressure support during LGP. Figure 2.14 schematically illustrates this two-phase material balance concept. The control volume is the effective fracture network, which includes all connected hydraulic fractures, secondary fractures (i.e. minor- and micro-fractures created due to the change of stress), and reactivated pre-existing natural fractures contributing to fluid flow towards the wellbore. It should be noted that the model does not aim to explicitly model the complex fracture network. Rather, it aims to lump all connected and producing fractures as an effective fracture system. During flowback period, the fracture system is assumed to have infinite conductivity compared with the surrounding matrix. Therefore, the fracture exhibits boundary-dominated flow regime, where pressure response with time can be treated as space-independent (i.e. $\Delta P_f = \Delta P_{wf} = \Delta \overline{P_f}$) despite its complex geometry (Patzek et al., 2013; Edwards et al., 2015). Before flowback, the fracture system is initially filled with gas and water (Figure 2.14a). The gas is believed to be released from the water-wet shale matrix imbibing the water during the fracturing and shut-in periods (Dehghanpour et al., 2012; 2013). After opening the well, the fracture network first undergoes pressure depletion during EGP phase (Figure 2.14b). In this phase, the fluid/pressure communication between the fracture network and the matrix is assumed to be negligible. Two-phase (gas + water) production comes from 1) expansion of initial gas in fractures, 2) expansion of initial water in fractures, and 3) fracture closure. When the fracture pressure drops below the reservoir pressure, gas and water from the matrix kick into the fracture network and production turn to the LGP phase (Figure 2.14c). In this phase, the drive mechanisms for two-phase production include 1) expansion of gas in fractures, 2) expansion of water in fractures, 3) fracture closure, 4) gas influx from the matrix, and 5) water influx from the matrix. The proposed material balance concept in Figure 2.14 forms the basics of this study and will be used in the following chapters.

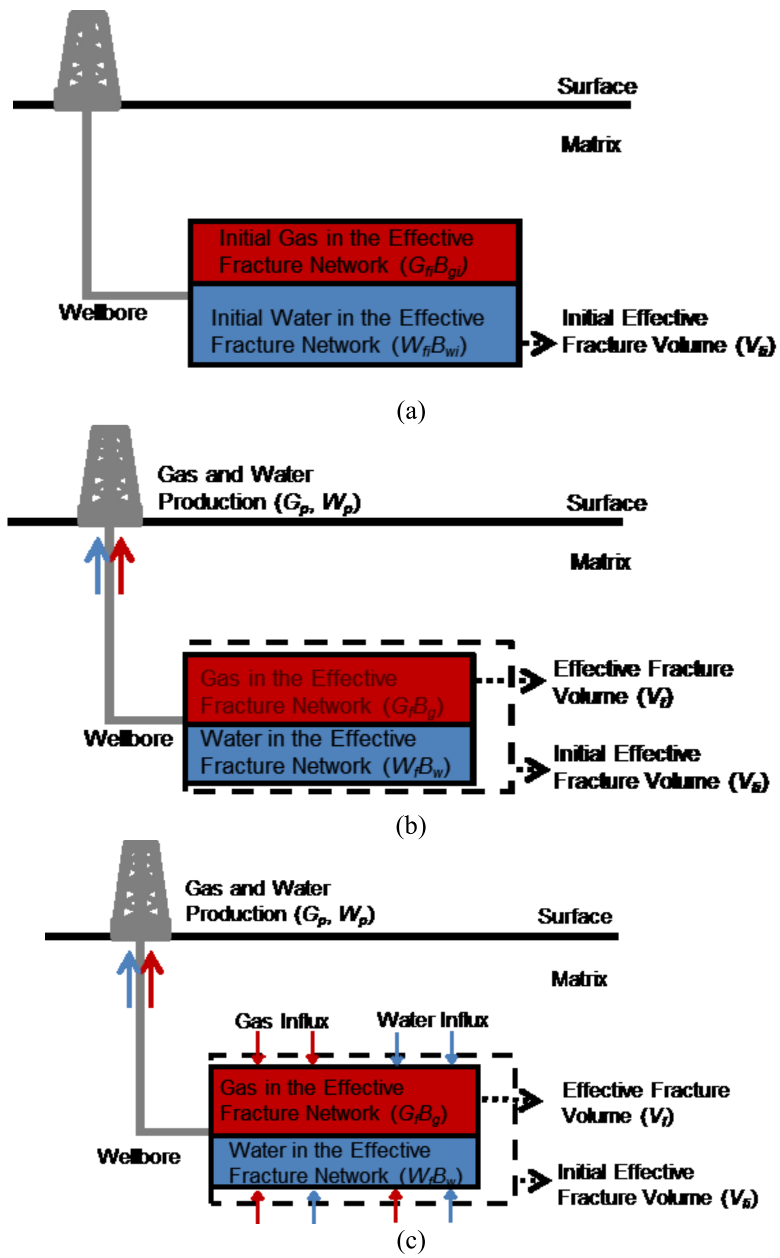

Figure 2.14: Schematic illustration of the material balance concept: (a) Before flowback, the effective fracture network is simplified as an arbitrary "tank" filled with free gas and water; (b) Fracture depletion during EGP phase; (c) Gas and water from the matrix kick into the effective fracture network during LGP phase (Xu et al., 2017).

2.7 Summary

This chapter qualitatively interprets rate and pressure flowback data from an eight-well pad completed in the Horn River Basin, identifies and validates the flow regimes during flowback period, investigates key drive mechanisms in different flow regimes by using numerical simulation, and proposes a material balance concept for flowback analysis.

The analyzed wells show instantaneous gas production once flowback starts. Their diagnostic plots of Gas Water Ratio (GWR) show a V-shape behaviour. This behaviour divides flowback data into two distinct flow regimes. The first regime is the Early Gas Production (EGP) characterized by a decreasing GWR trend. The second regime is the Late Gas Production (LGP) characterized by an increasing GWR trend.

The V-shape GWR curve and instantaneous gas production suggest the presence of initial free gas in the fracture network before flowback. This hypothesis is in agreement with the numerical model simulating the hydraulic fracturing, shut-in, and flowback processes. The simulation results show that free gas in the fractures, which comes from the counter-current imbibition during the shut-in period, is responsible for the immediate gas production observed.

Gas material balance analysis (i.e. *p/Z* plots) of the flowback data shows a linear relationship during EGP, followed by a gradual decline during LGP. Based on this signature, the effective fracture system is simplified as a two-phase tank of arbitrary geometry. Although there is negligible fluid and pressure support from the matrix during the EGP phase, this support becomes signigficant during the LGP phase. The proposed material balance concept will be used in modeling flowback data in subsequent chapters.

Nomenclature

B_g = gas formation volume factor, std. volume/res. volume

B_{gi} = gas formation volume factor at initial conditions, std. volume/res. volume

B_w = water formation volume factor, std. volume/res. volume

B_{wi} = water formation volume factor at initial conditions, std. volume/res. volume

G = volume of origin gas in place, std. m^3

G_{fi} = volume of gas initially in the fractures, std. m^3

G_f = volume of gas in the fractures, std. m^3

G_p = cumulative gas production, std. m^3

G_p^* = cumulative gas production obtained from p/Z plots, std. m^3

k = absolute permeability, md

k_{rg} = gas relative permeability

k_{rw} = water relative permeability

p = pressure, psi

p_i = initial pressure, psi

p_g = pressure for gas phase, psi

p_w = pressure for water phase, psi

P_c = capillary pressure, psi

q_g = gas flow rate, m^3/d

q_w = water flow rate, m^3/d

S_g = gas saturation

S_w = water saturation

V_f = effective fracture volume, m^3

V_{fi} = initial effective fracture volume, m^3

W_{fi} = volume of water initially in the fractures, std. m^3

W_f = volume of water in the fractures, std. m^3

Z = gas compressibility factor

Z_i	=	gas compressibility factor at initial conditions
μ_g	=	gas viscosity, cp
μ_w	=	water viscosity, cp
ϕ	=	porosity
σ	=	surface tension, dynes/cm

Chapter 3: Estimating Initial Volume of the Effective Fractures using Early-Time Flowback Data: A Material Balance Approach

This chapter is a modified version of the article Xu et al. (2015) published in *Journal of Natural Gas Science and Engineering*. I was responsible for analyzing field data, forming key concepts, developing analytical models, writing and editing manuscripts. My co-authors assisted in discussing model outputs, reviewing manuscripts, and securing company approvals for publication. The original article was modified by changing the voice from plural first person (we) to singular first person (I). The introduction section was revised to connect with Chapter 2 and highlight the focus of this chapter. To maintain consistency and prevent redundancy, some sections in the original published paper (including reservoir and well pad description, diagnostic plots, numerical simulation, and flowback regime analysis) have been moved to Chapter 2. In addition, the numerical validation section in the original article will be presented in Chapter 5.

3.1 Introduction

This chapter aims to develop a two-phase closed-tank material balance equation (MBE) applicable for the EGP phase discussed in Chapter 2. One key advantage of the material balance model is that it does not consider the complex fracture geometry. Besides, the material balance model requires fewer input parameters since it neglects the space-dependent properties, such as pressure gradient in the fractures, fluid saturations, fracture density and distribution. Fewer input parameters reduce the uncertainties associated with the current flowback analysis models which try to model fluid flow signatures inside the complex fracture networks. To demonstrate the feasibility of the model, the proposed MBE is applied on the target well pad. Field application shows that the MBE enables estimation of the initial effective fracture volume (V_{fi}) by using the EGP data. A sensitivity analysis is conducted to investigate the effect of initial free gas saturation in fractures on the estimated V_{fi}. Furthermore, a comparative analysis is conducted to investigate the relationships between estimated V_{fi} and various operational parameters (e.g. TIV, number of stages, perforation clusters, shut-in time, and flowback sequence).

The rest of this chapter has four main sections. Section 3.2 presents the closed-tank MBE. Section 3.4 demonstrates the application of the closed-tank model on the target well pad. Section 3.5 discusses the output parameters from the model and investigates the relationships between V_{fi} and key operational parameters. Section 3.7 concludes this chapter. For conciseness of this dissertation, the numerical validation (Section 3.3) and limitations (Section 3.6) of the proposed model will be presented in Section 5.4 and Section 5.2, respectively.

3.2 Two-Phase Closed-Tank Material Balance Equation for Early Gas Production

The diagnostic analysis in Chapter 2 shows that the effective fracture network can be approximated by a "two-phase closed tank" during EGP. On this basis, this section derives the closed-tank MBE applicable to EGP phase in shale gas wells.

3.2.1 Conceptual Model

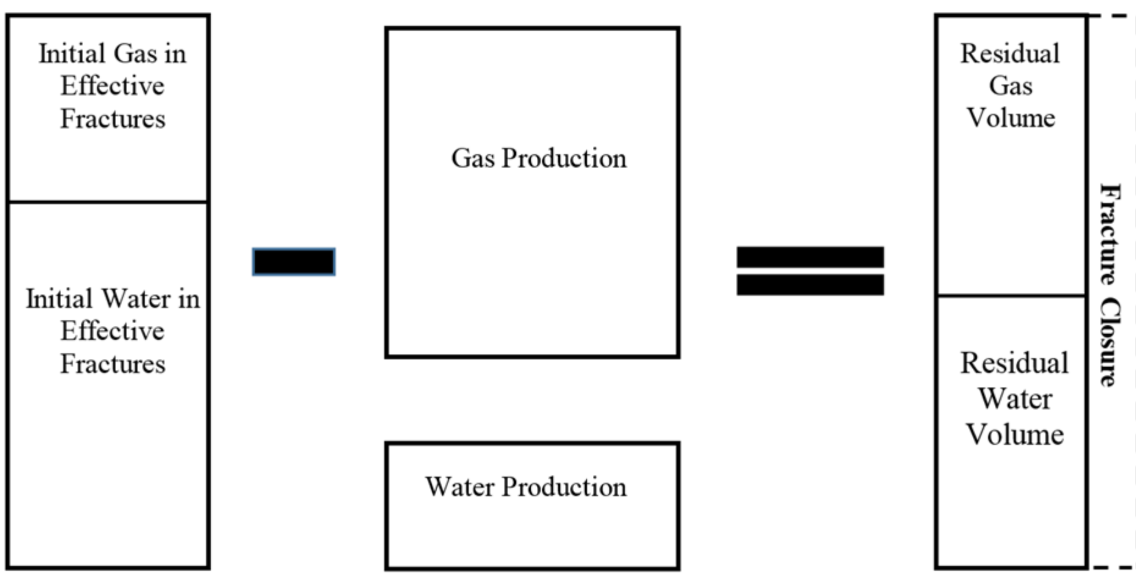

Figure 3.1: Schematic illustration of the material balance concept for EGP phase. Gas and water are produced from three mechanisms: free gas expansion in fractures, water expansion in fractures, and fracture closure.

Figure 3.1 schematically explains the closed-tank material balance concept. The control volume is the "effective fracture network" that includes all active/connected fractures in the same pressure system. The "effective fracture network" has an arbitrary geometry, which is represented using a black box in Figure 3.1. Before flowback, the system is saturated with free gas and water. The free gas is believed to come from the matrix due to counter-current imbibition during the extended shut-in, as discussed in Chapter 2. Based on the simulation results in Chapter 2, it is assumed that during EGP phase, gas and water production are driven by 1) expansion of initial free gas in fractures, 2) expansion of initial water in fractures, and 3) fracture closure.

3.2.2 Mathematical Derivation

Figure 3.1 shows the volume balance of the effective fracture network during EGP phase:

Volume of Initial Effective Fracture Network

= Volume of Initial Gas in Fractures + Volume of Initial Water in Fractures

= Volume of Residual Gas in Fractures + Volume of Residual Water in Fractures + Fracture Volume Loss (Fracture Closure)

$$G_{fi}B_{gi} + W_{fi}B_{wi} = \left(G_{fi} - G_p\right)B_g + \left(W_{fi} - W_p\right)B_w + \Delta V_f \tag{3.1}$$

where G_{fi} and W_{fi} are the volumes of initial gas and initial water in fractures at standard conditions, respectively. B_{gi} and B_{wi} are the gas and water formation volume factor at initial conditions, respectively. G_p and W_p are the cumulative gas and water production, respectively. ΔV_f represents the volume change of the effective fracture network due to fracture closure.

Fracture closure is a function of the fracture stiffness, $\mathcal{S}_f$, defined by the reciprocal of fracture compliance (Craig, 2006). Assuming constant $\mathcal{S}_f$ and constant facture surface area (A_f) during EGP phase, ΔV_f can be expressed as

$$\Delta V_f = A_f \Delta \omega_f = A_f \Delta \left(\frac{P_f - P_c}{\mathcal{S}_f}\right) = \frac{A_f}{\mathcal{S}_f}\Delta P_f \tag{3.2}$$

where w_f is the average fracture aperture. P_f is the fracture pressure, and P_c is the minimum pressure required to keep the effective fractures open.

Substituting Eq. 3.2 into Eq. 3.1 gives

$$G_pB_g + W_pB_w = G_{fi}\left(B_g - B_{gi}\right) + W_{fi}(B_w - B_{wi}) + \frac{A_f}{S_f}\Delta P_f \tag{3.3}$$

Assuming constant water compressibility (c_w) during EGP, $c_w = -\frac{1}{V_w}\left(\frac{\partial V_w}{\partial P_f}\right)_T = -\frac{1}{B_w}\left(\frac{\partial B_w}{\partial P_f}\right)_T$, Eq. 3.3 becomes

$$G_pB_g + W_pB_w = G_{fi}\left(B_g - B_{gi}\right) + W_{fi}B_{wi}\left(P_{fi} - P_f\right)\left(\frac{1}{B_{wi}}\frac{B_w - B_{wi}}{P_{fi} - P_f}\right) + \frac{A_f}{S_f}(P_{fi} - P_f) \tag{3.4}$$

$$G_pB_g + W_pB_w = G_{fi}B_{gi}\left(\frac{B_g}{B_{gi}} - 1\right) + W_{fi}B_{wi}\left(P_{fi} - P_f\right)c_w + \frac{A_f}{S_f}(P_{fi} - P_f) \tag{3.5}$$

Note that $G_{fi}B_{gi}$ and $W_{fi}B_{wi}$ are volumes of initial gas and initial water in the effective fracture network before flowback, respectively. They are both related to V_{fi} by

$$W_{fi}B_{wi} = V_{fi}S_{wi} = \frac{G_{fi}B_{gi}}{S_{gi}}S_{wi} = \frac{1-S_{gi}}{S_{gi}}G_{fi}B_{gi} \tag{3.6}$$

where S_{wi} and S_{gi} are the initial gas and water saturations in the effective fracture network, respectively.

Substituting Eq. 3.6 into Eq. 3.5 gives

$$G_pB_g + W_pB_w = G_{fi}B_{gi}\ [\left(\frac{B_g}{B_{gi}} - 1\right) + \left(\frac{1-S_{gi}}{S_{gi}}C_w + \frac{A_f}{S_f}\frac{1}{G_{fi}B_{gi}}\right)\Delta \mathrm{P}_f] \tag{3.7}$$

Eq. 3.7 can be simplified by defining Underground Withdrawal (F) and Expansion Coefficient (E):

$$F = G_pB_g + W_pB_w \tag{3.8}$$

$$E = \left(\frac{B_g}{B_{gi}} - 1\right) + \left(\frac{1-S_{gi}}{S_{gi}}c_w + \frac{A_f}{S_f}\frac{1}{G_{fi}B_{gi}}\right)\Delta P_f \tag{3.9}$$

$$F = G_{fi}B_{gi}[E] \tag{3.10}$$

Eq. 3.10 is the final form of the closed-tank MBE used in our study. It predicts that a plot of F vs. E yields a straight line which passes through the origin with slope of $G_{fi}B_{gi}$. F represents cumulative fluid (gas + water) production during early-time flowback. E is a dimensionless term that accounts for all three drive mechanisms considered: $\left(\frac{B_g}{B_{gi}}-1\right)$ represents expansion of initial gas in the fractures; $\left(\frac{1-S_{gi}}{S_{gi}}C_w+\frac{A_f}{s_f}\frac{1}{G_{fi}B_{gi}}\right)\Delta P_f$ combines the effects of initial water expansion in fractures and fracture closure.

Furthermore, V_{fi} can be estimated by

$$V_{fi}=\frac{G_{fi}B_{gi}}{S_{gi}} \tag{3.11}$$

3.3 Numerical Validation

The closed-tank MBE is validated against a 2D numerical model using the CMG software. To prevent redundancy of this thesis, the numerical validation will be presented in Section 5.4.

3.4 Field Application

Eq. 3.10 suggests that the plot F vs. E on Cartesian coordinates gives slope of $G_{fi}B_{gi}$, which can be further used to calculate V_{fi} in Eq. 3.11. This section aims to estimate V_{fi} for each well of the target pad by using the proposed closed-tank MBE. It is worth noting that in field application, the change in average P_f is represented by the change in BHP (i.e. $\Delta P_f=\Delta P_{wf}$).

However, analysis of EGP data using Eq. 3.10 requires S_{gi} which is unknown in field cases. Therefore, field applications of the proposed model brings up an interesting challenge in that either S_{gi} or $G_{fi}B_{gi}$ must be determined by independent methods. In this study, applications of the closed-tank model is demonstrated in three different scenarios: 1) V_{fi} is estimated by assuming a reasonable S_{gi}; 2) A sensitivity analysis is conducted to investigate the effect of S_{gi} on V_{fi}; and 3) The closed-tank MBE is constrained by the G_p^* values obtained from the x-axis intercept of the p/Z plots (Figure. 2.13).

3.4.1 Estimating Initial Effective Fracture Volume with Assumed Values of Initial Free Gas Saturation

Although gas builds up in the effective fractures by counter-current imbibition during the shut-in period, the large volumes of water injected ensure that a significant portion of the fracture networks is still saturated with water (Ezulike and Dehghanpour, 2014a). Therefore, S_{gi} is assumed to be 15 %, and Eq. 3.10 is applied on the target wells. The assumption is based on the results form the spontaneous imbibition experiments conducted on the cores samples from a similar well in the HRB (Makhanov et al., 2014). Figure 3.2 shows the results of the material balance analysis. The data points correspond to EGP phase only.

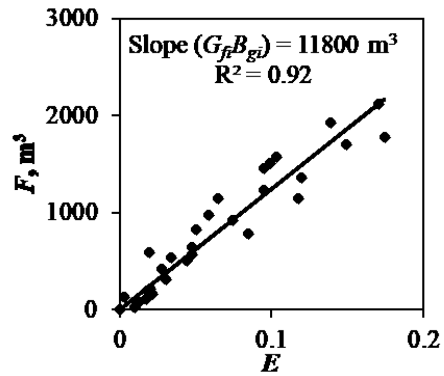

(a)

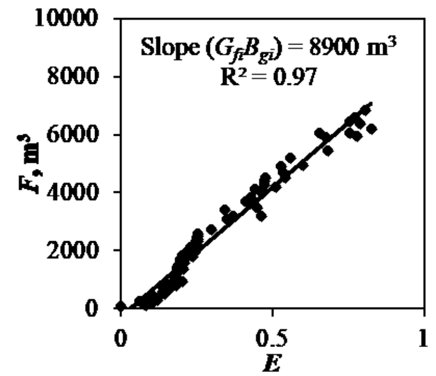

(b)

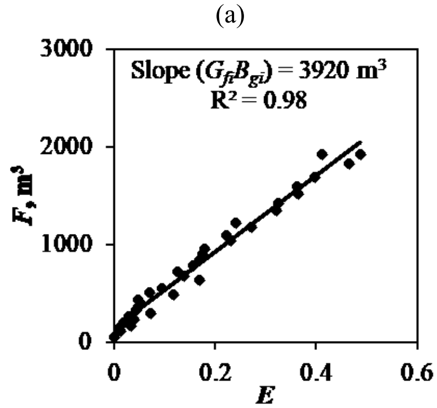

(c)

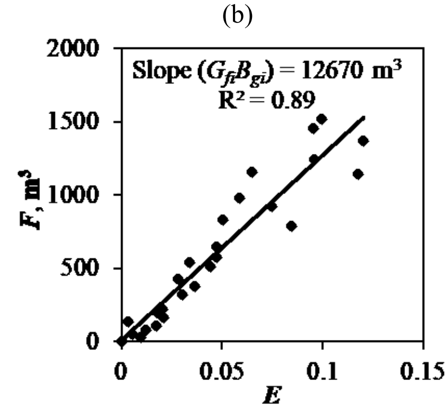

(d)

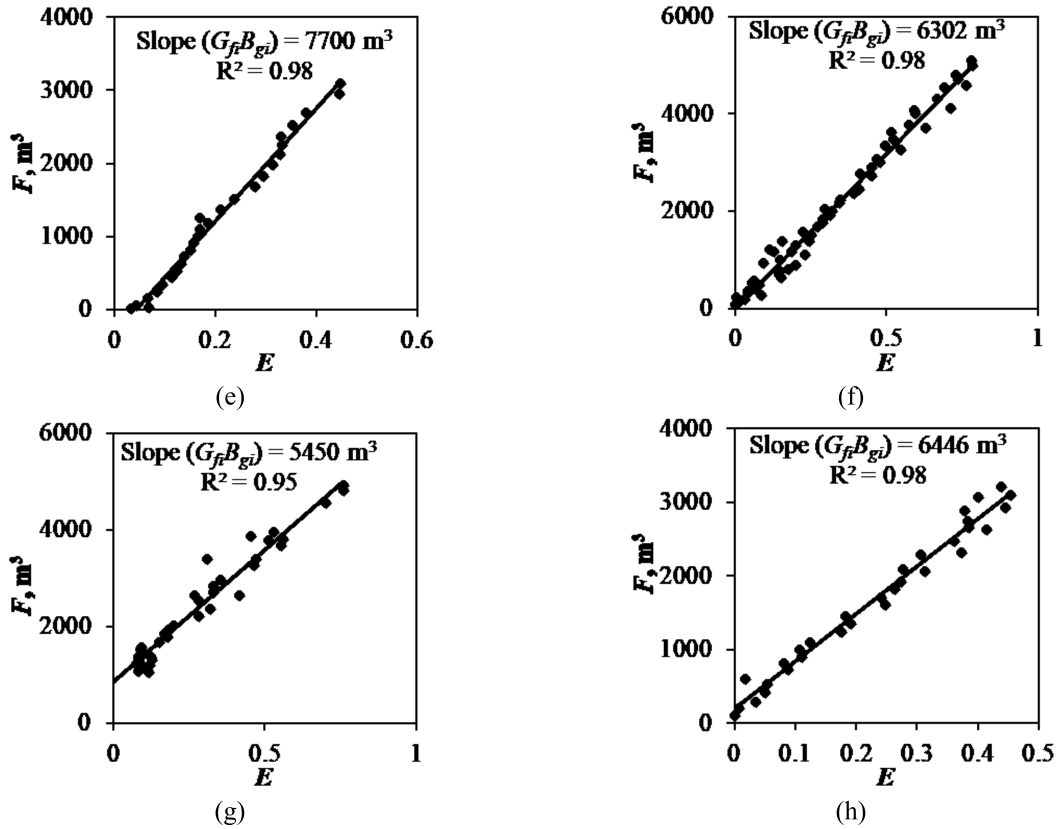

Figure 3.2: Material balance plots for the target pad in the HR (Assuming S_{gi} = 15 %). Plots (a) to (h) correspond to Wells A to H, respectively. Plots of F vs. E show straight lines across the origin with the slopes of $G_{fi}B_{gi}$. The small y-intercepts in some wells (i.e. Wells B, C, and H) can be viewed as a "skin" at early-time flowback. Well G has a relatively large intercept due to ignoring the very early-time data points.

Figure 3.2 shows linear relationships between F and E, as predicted by Eq. 3.10. The key output of these plots is the slope of the straight line that can be interpreted as $G_{fi}B_{gi}$. However, it should be noted that some wells (i.e. Wells B, C, G, and H) show a small, positive y-axis intercept which is not expected from the derived MBE. The intercepts indicate a small amount of production (i.e. F) with negligible pressure drop inside the fracture network (i.e. E). These production might come from the wellbore storage at the very beginning of flowback. Well G shows a relatively large intercept on y-axis. This happens because some early-time data points were ignored when applying the MBE. Compared to other wells, Figures 2.5 and 2.13 show that Well G has a delayed response in V-shape GWR and linear p/Z trend, respectively. These very early-time data was neglected in the material balance analysis, resulting in the relatively large intercept in the MBE plot.

3.4.2 Effect of Initial Gas Saturation on the Estimated Initial Effective Fracture Volume

Figure 3.3 shows the typical response of V_{fi} and $G_{fi}B_{gi}$ to the change in S_{gi} when S_{gi} increases from 0 to 40 % for all eight wells. In all cases, $G_{fi}B_{gi}$ first increases with increasing S_{gi} when S_{gi} < 20 %, and reaches to a plateau when S_{gi} is higher than 20 %. That is to say, $G_{fi}B_{gi}$ becomes less sensitive as S_{gi} increases. On the other hand, V_{fi} remains highly sensitive to S_{gi}. The values of V_{fi} keeps decreasing when S_{gi} changes from 0 to 40 %. The general understanding in hydraulically-fractured wells is that V_{fi} cannot exceed the TIV during the fracturing operations (Ezulike et al., 2014a). Thus, the sensitivity analysis suggests that there exists a minimum initial gas saturation ($S_{gi\text{-}min}$) that ensures the estimated V_{fi} is always less than the TIV (shown by red arrows in Figure 3.3). Table 3.1 lists the values of $S_{gi\text{-}min}$ for this well pad. The results show that the $S_{gi\text{-}min}$ for this pad is between 5-20 %, suggesting a significant portion of the created fracture volume must be saturated with gas before flowback. This result is in agreement with the simulation studies discussed in Chapter 2.

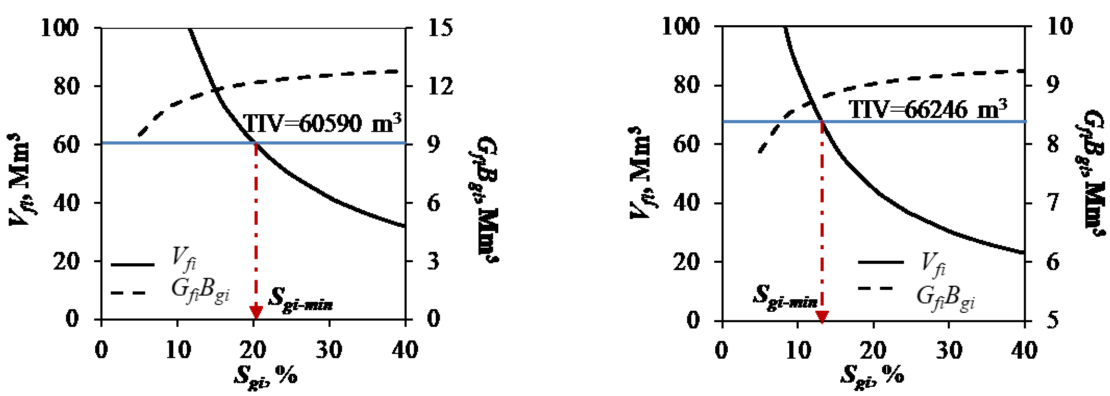

(a) (b)

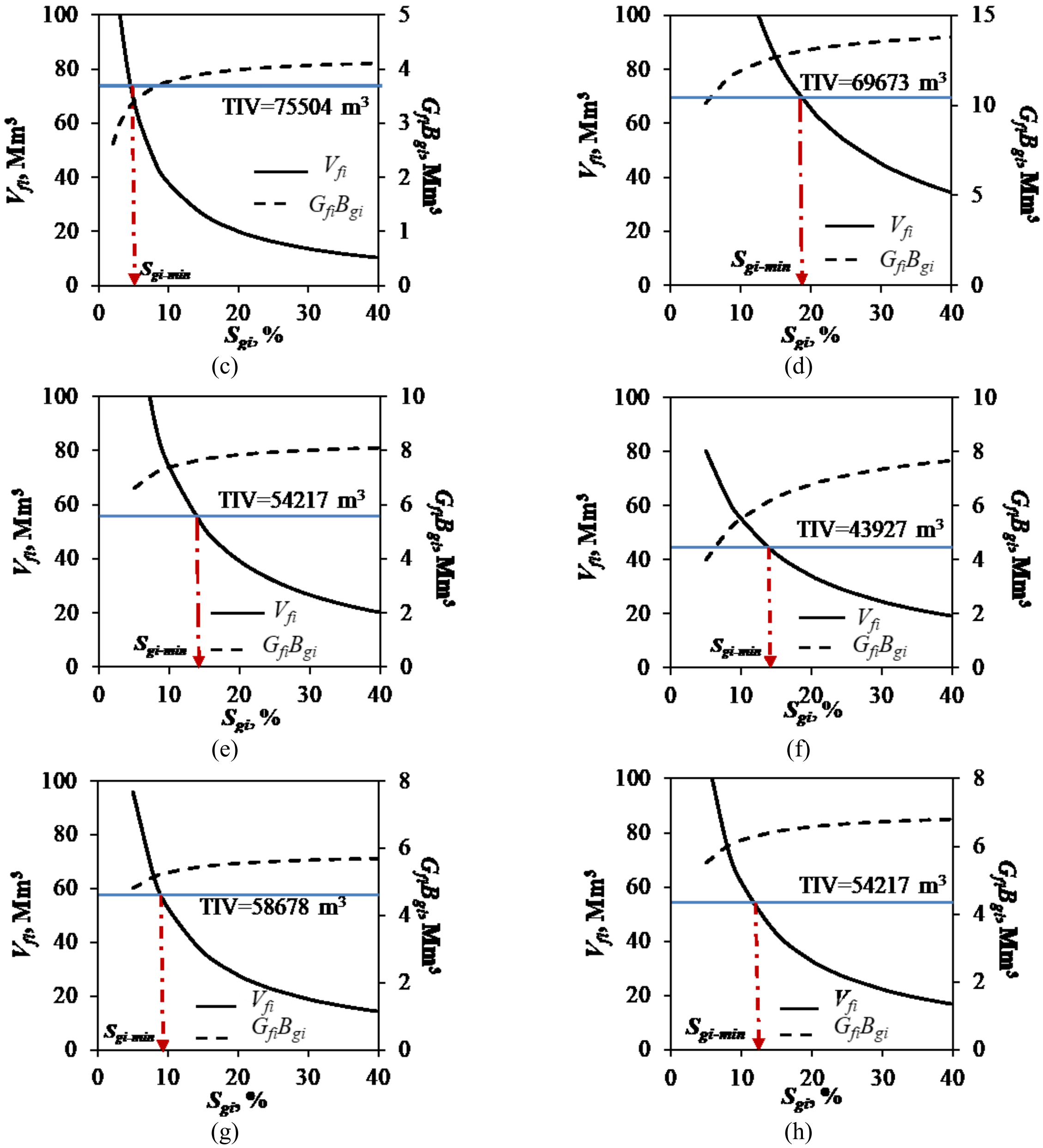

Figure 3.3: Effect of S_{gi} on estimated V_{fi} and $G_{fi}B_{gi}$ (0 < S_{gi} < 40%). Plots (a) to (h) correspond to Wells A to H, respectively. The estimated $G_{fi}B_{gi}$ increases with increasing S_{gi} when S_{gi} < 20 %, and reaches to a plateau when S_{gi} > 20 %. The estimated V_{fi} remains highly sensitive to the change in S_{gi}. TIV gives a value of minimum gas saturation $S_{gi\text{-}min}$ before flowback.

Table 3.1: Calculated V_{fi} using closed-tank MBE.

Well ID	TIV (m^3)	$S_{gi\text{-}min}$ (%)	G_p^* (Mm^3)	S_{gi} (%)	$G_{fi}B_{gi}$ (m^3)	V_{fi} (m^3)	HFE (%)	TLR (%)
A	60,590	21	3,700	22.6	12,310	54,469	90	22
B	66,246	13	2,750	25.7	9,149	35,600	54	14
C	75,504	5	1,050	5.8	3,495	60,258	79	8
D	69,673	18	3,950	20.7	13,142	63,487	91	12
E	54,217	13	2,350	18.4	7,820	42,500	78	22
F	43,927	14	1,950	16.8	6,487	38,613	88	32
G	58,678	9	1,650	16.7	5,490	32,875	56	21
H	54,217	13	2,000	24.0	6,654	27,725	51	16

The $G_{fi}B_{gi}$ is the optimal volume of initial gas in the fracture network. $G_{fi}B_{gi} = G_p^*B_{gi}$, $B_{gi} = 0.003327$.

3.4.3 Estimating Initial Effective Fracture Volume with Initial Gas Volume obtained from Gas Material Balance Plots

In the final step, the material balance analysis is constrained by the G_p^* values obtained from the intercept of the p/Z plots. Figure 2.7 shows that the x-intercept of p/Z plots gives an estimate of G_{fi} at standard conditions (reported as G_p^*). Table 3.1reports the values of G_p^* for the target well pad. Therefore, there exists an optimal value of S_{gi} that matches the $G_{fi}B_{gi}$ obtained from slope of the material balance plot and from the intercept of the p/Z plot ($G_p^*= G_{fi}$).

Table 3.1 lists the optimal values of S_{gi}, and the corresponding values of $G_{fi}B_{gi}$ and V_{fi} for the target wells. The S_{gi} obtained is the average gas saturation in the effective fracture network, including the secondary and natural fractures. The V_{fi} is the total effective fracture volume contributing to the flow, which includes not only the primary/hydraulic fracture network but also all active secondary and natural fractures. However, it should be noted the calculated V_{fi} lumps the effects of hydraulic and natural fractures into an "effective fracture network", without differentiating their mechanical and/or hydraulic behavior. Although the primary fractures are mostly saturated with water because of the large volumes of fracturing fluids injected, gas builds up in the effective fracture network during the shut-in period. This gas is released once the wells are opened, causing the instant gas production observed in the HR shale gas wells.

3.5 Results Discussion

This section conducts a volumetric comparison to understand hydraulic fracturing efficiency (HFE) by comparing the estimated V_{fi} with TIV and the volumes of produced water. It also investigates the effects of various operational parameters on estimated V_{fi}.

3.5.1 Volumetric Comparison

Table 3.1 shows that there is a significant difference between TIV and the estimated V_{fi} for the wells analyzed. This indicates that a significant portion of the injected water is lost into pre-existing natural and secondary fractures and/or imbibed into the shale matrix during the hydraulic fracturing and the shut-in periods. HFE is defined as V_{fi}/TIV, which represents the effective fracture volume created per unit volume of fracturing fluid injected into the formation. On average, the calculated HFE is about 75 % for this well pad. Table 3.1 also presents the total load recovery (TLR) for the eight wells, which is defined as cumulative water production during flowback period divided by TIV. The results show that TLR is between 10 - 40 % for this well pad.

However, the relatively high values of HFE (~75 %) for the target wells cannot explain the poor load recovery (< 25 %) observed. If indeed a large percentage of the injected fluid is effective in creating hydraulic fractures, the load recovery should be much larger than 10 - 15 % commonly observed during flowback of shales. One possible explanation is that the total water recovered during the flowback comes from the large, well connected hydraulic fracture networks. The water imbibed into the existing natural fractures, trapped in small and poorly connected secondary fractures, and retained in the bottom of vertical fractures can hardly be recovered during flowback (Parmar et al., 2014). Therefore, the huge discrepancy between HFE and TLR suggest there is severe water trapping in the effective fracture network. This result highlights the importance of considering the effects of water trapping in modeling fluid flow in shale reservoirs.

3.5.2 Correlations between the Initial Effective Fracture Volume and the Fracture Design Parameters

This section attempts to investigate possible correlations between the estimated V_{fi} and some common fracture design/operational parameters, such as TIV, number of stages, number of clusters per stage, and the flowback sequence within a well pad. It should be noted that due to limited number of wells analyzed, the trends between operational parameters and estimated V_{fi} might be insignificant or misleading.

Figure 3.4a shows the relationship between the TIV and estimated V_{fi}. Expectedly, TIV and V_{fi} has a positive correlation. This signature indicates that wells with higher TIV would generally result in higher V_{fi}, which is beneficial for future production.

On the other hand, Figures 3.4b and 3.4c show that the estimated V_{fi} has no linear correlation with the number of perforation clusters per stage or the number of fracture stages. The results are in agreement with findings by Cheng (2012b) stating that increasing the number of perforation clusters does not necessarily have a positive impact on production rates or ultimate recovery because of the increased number of ineffective fractures. According to Cheng (2012b), increasing the number of perforation clusters may even inhibit fracture propagation and increase the number of ineffective fractures.

Figure 3.4d compares the HFE with the flowback sequence of wells in this pad. It shows that the wells flowed earlier have a higher V_{fi}/TIV value compared with the ones opened later. One possible explanation is that the wells flowed earlier help clean up the vertical wellbore and thus have more significant wellbore storage effects. In other words, the calculated V_{fi} contains not only the actual fracture network downhole, but also part of the wellbore volume. This signature implies that wellbore storage effects may mask the flowback data, especially for the wells flowed earlier. Another possible explanation is that the wells flowed earlier may producing fluids beyond their drainage area, resulting in a higher V_{fi} calculated from material balance analysis. This signature suggests that the proposed single well material balance approach may not be sufficient for flowback data analysis in well pads that have severe inter-well communications. Combining production data from different wells and analyzing the well pad as "flow groups" will remain the subject of future studies.

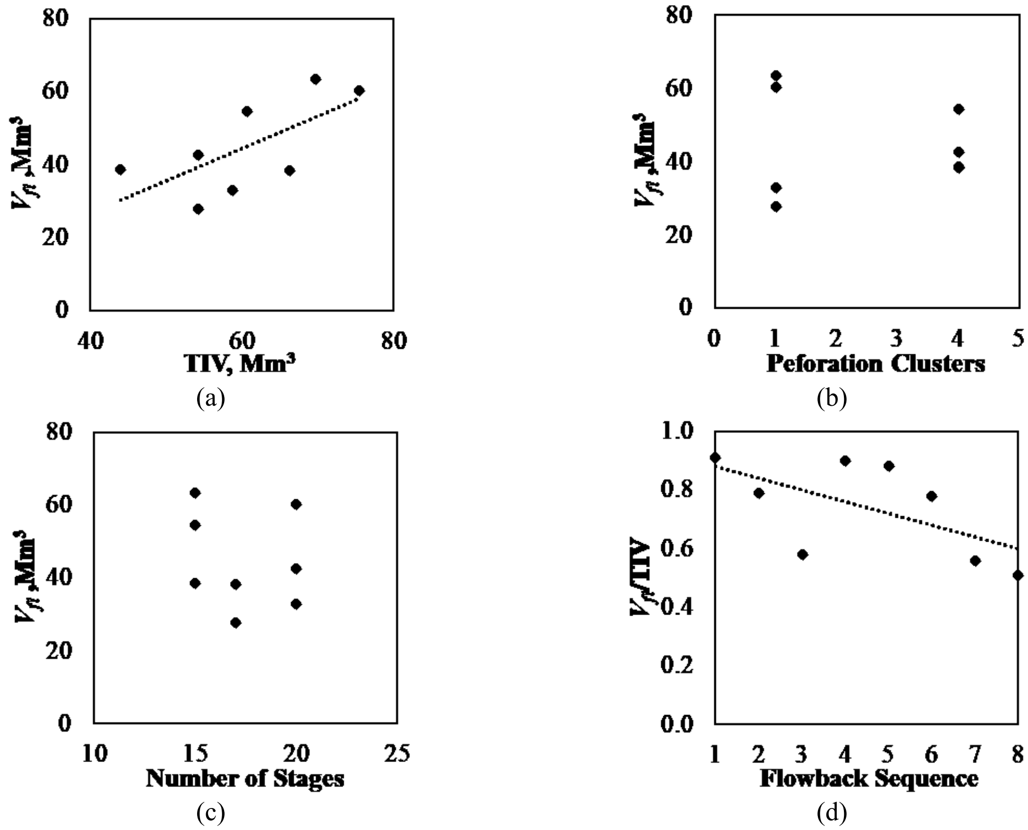

Figure 3.4: Cross plots of V_{fi} vs. common operational parameters for the target well pad in HRB: (a) V_{fi} vs. TIV; (b) V_{fi} vs. number of perforation clusters (c) V_{fi} vs. number of stages (d) V_{fi}/TIV vs. flowback sequence.

3.6 Limitations

The proposed model is a single-well analysis method, without considering the effects of well communication/interference. In addition, different well operational parameters may result in different fracture patterns among different wells. Spatial distribution of the fracture network and its potential effects on V_{fi} are beyond the scope of this study.

In addition, the proposed model assumes the effective fracture network as a "closed tank", and describes the early-time (first 200 hrs) flowback signatures using a two-phase MBE. In Chapter 5, the closed-tank MBE will be extended to an open-tank MBE. The limitations of this closed-tank MBE are discussed in detail in Section 5.2, and are no longer be presented here.

3.7 Summary

This chapter 1) proposes a closed-tank material balance model for analyzing two-phase rate and pressure data during early-time flowback period, 2) demonstrates the application of the proposed model on an eight-well pad completed in the Horn River Basin, and 3) investigate the effects of key operational parameters on initial effective fracture volume. The proposed model enables estimation of initial effective fracture volume contributing to flow regardless of fracture geometry.

The results of this chapter show that a significant percentage of the induced fracture volume comes from secondary/natural fractures, not primary hydraulic fractures. The results also suggest that the flowback sequence of wells within a pad plays an important role in the observed flow signatures. Wells flowed earlier not only produce from fractures within their drainage area. They may also produce from the inter-connected fractures of adjacent wells. For the target pad, no direct correlation is observed between the number of clusters/stages and the estimated initial effective fracture volume. This is possibly due to the increased number of ineffective fractures created during the stimulation process. Overall, the results from this chapter suggest that some operational parameters (such as the flowback sequence in a well pad) should be considered when planning future fracturing operations.

Nomenclature

A_f	=	fracture-matrix interface area, m^2
B_g	=	gas formation volume factor, std. volume/res. volume
B_{gi}	=	gas formation volume factor at initial conditions, std. volume/res. volume
B_w	=	water formation volume factor, std. volume/res. volume
B_{wi}	=	water formation volume factor at initial conditions, std. volume/res. volume
c_w	=	water compressibility, 1/psi
E	=	expansion coefficient

F	=	underground withdrawal, res. m^3
G_{fi}	=	volume of gas initially in the fractures, std. m^3
G_p	=	cumulative gas production, std. m^3
G_p^*	=	cumulative gas production obtained from p/Z plots, std. m^3
P_c	=	closure pressure, psi
P_f	=	average fracture pressure, psi
P_{fi}	=	initial fracture pressure, psi
S_{gi}	=	initial gas saturation inside the fractures
$S_{g\text{-}min}$	=	minimum gas saturation inside the fractures
S_{wi}	=	initial water saturation inside the fractures
V_f	=	effective fracture volume, m^3
V_{fi}	=	initial effective fracture volume, m^3
V_w	=	water volume, m^3
w_f	=	average fracture aperture, m
W_{fi}	=	volume of water initially in the fractures, std. m^3
W_p	=	cumulative water production, std. m^3
Z	=	gas compressibility factor
Δ	=	change
$\mathcal{S}_f$	=	fracture stiffness, Pa/m

Chapter 4: A Flowing Material Balance Equation for Early-Time Two-Phase Flowback Analysis in the Horn River Shales

This chapter is a modified version of the article Xu et al. (2016a) published in *Journal of Petroleum Science and Engineering*. I was responsible for analyzing field data, forming key concepts, developing numerical and analytical models, writing and editing manuscripts. My co-authors assisted in discussing model outputs, reviewing manuscripts, and securing company approvals for publication. The original article was modified by changing the voice from active to passive. The introduction section was revised to connect with the previous chapters and highlight the focus of this chapter. To maintain consistency and prevent redundancy, the quantitative analysis in the original published paper (including field observations, numerical simulation, and flowback regime analysis) have been moved to Chapter 2.

4.1 Introduction

Flowback data analysis presents the earliest opportunity to characterize the hydraulically-stimulated reservoirs (Bearinger, 2013). The diagnostic plots presented by Abbasi (2013) and Abbasi et al. (2014) show that the first flow regime observed in tight oil/gas reservoirs is single-phase water flow. They developed a rate transient model to describe the single-phase flow regime. The model gives fracture permeability and storage coefficient estimates by history matching early-time flowback data. Crafton and Gunderson (2006; 2007) demonstrated the use of high frequency single-phase flowback data for estimating fracture permeability and conductivity. Williams-Kovacs et al. (2015) considered the single-phase period to be fracture depletion region. They analyzed the water flowback data using radial flow and flowing material balance plots and obtained fracture conductivity and permeability.

Unlike tight reservoirs, shale gas reservoirs usually show immediate two-phase flow after opening wells. The immediate multi-phase (gas + water) flow behavior has been reported in the HR (Ghanbari et al., 2013; Abbasi, 2013), the Barnett (Zhang and Ehlig-Economides, 2014), and the Marcellus shales (Clarkson and Williams-Kovacs, 2013). Thus, the single-phase flowback models are not applicable for characterizing hydraulic fractures in such shale gas reservoirs.

Many methods have been proposed to model the multi-phase flow characteristics in shale gas reservoirs. Clarkson and Williams-Kovacs (2013) analyzed two-phase flowback data using simulation and pressure transient techniques originally developed for CBM reservoirs. The methodology takes advantage of the similarity between the two-phase flowback and the simultaneous flow of gas and water during long-term production from fractured coal reservoirs. They improved their approach by introducing stochastic history matching and multi-phase type curve matching techniques to deal with the uncertainties in fracture characterization from flowback data. Ezulike and Dehghanpour (2014b) developed a dynamic relative permeability (DRP) function applicable for modeling two-phase flowback data from wells completed in both tight and shale reservoirs. The DRP function is obtained from a data-driven analysis of cumulative water and hydrocarbon production data recorded during flowback. The authors suggested incorporating this DRP function into the existing linear dual porosity models. Li et al. (2013) carried out simulation studies by varying several fracture parameters to develop a correlation between the early gas production signatures and the fracture parameters in shale reservoirs. Although this method allows qualitative comparison of fracture parameters from different wells and/or reservoirs, it is unable to quantitative characterize the fracture network. Alkouh et al. (2014) combined two-phase flowback data with long-term gas production data to characterize shale gas reservoirs. By conducting several simulation runs, they concluded that gas is the dominant phase in the system and that early-time water production is driven by the expansion of gas within the fractures. Thus, they neglected the difference between the total compressibility (c_t) and volumetric gas compressibility (c_g), and presented a method to estimate effective fracture volume by analyzing water flowback data.

The goals of this chapter is to extend the single-phase rate transient model developed by Abbasi et al. (2013) to a two-phase rate transient one to describe the early-time two-phase flow behavior observed in shale gas wells. Chapter 3 develops a closed-tank MBE for two-phase flowback during EGP. This chapter proposes a closed-tank flowing MBE by coupling the closed-tank MBE and a two-phase linear diffusivity equation. The DRP function proposed by Ezulike and Dehghanpour (2014b) is incorporated in the diffusivity equation to account for saturation change in the fracture network.

The rest of this chapter is organized as follows: Section 4.2 presents the flowing MBE; Section 4.3 proposes an analysis procedure for early-time two-phase flowback data analysis in gas shales; Section 4.4 demonstrates the application of the analysis procedure on two wells of the target well pad and discusses the results; Section 4.5 states the limitations of the flowing MBE; and Section 4.6 summarizes this chapter.

4.2 A Flowing Material Balance Equation for the Effective Fracture System

The aim of this section is to develop a flowing material balance model that describes two-phase flow in fractures during EGP phase.

4.2.1 Conceptual Model

The control volume is the effective fracture network in the stimulated reservoir volume (SRV) created by a multi-fractured horizontal well of length X_e, as shown in Figure 4.1. This schematic is an approximation of a very complex fracture geometry which also includes secondary fractures and pre-existing natural fractures. It does not consider specific fracture geometry but assumes an equivalent "effective fracture volume" with average fracture half-length of Y_e and fracture permeability of K_f. The effective fracture system contains an initial water saturation of S_{wi} and an initial free gas saturation of S_{gi}, corresponding to the volumes of initial water in fractures ($W_{fi}B_{wi}$) and initial gas in fractures ($G_{fi}B_{gi}$), respectively.

The conceptual model assumes that negligible gas contribution from the matrix during EGP and that the fracture system can be approximated by a two-phase "closed tank". Gas and water production gathered at the surface is driven by fracture closure and expansion of free gas and water in the effective fracture volume. Fracture linear flow towards the horizontal wellbore is assumed during EGP.

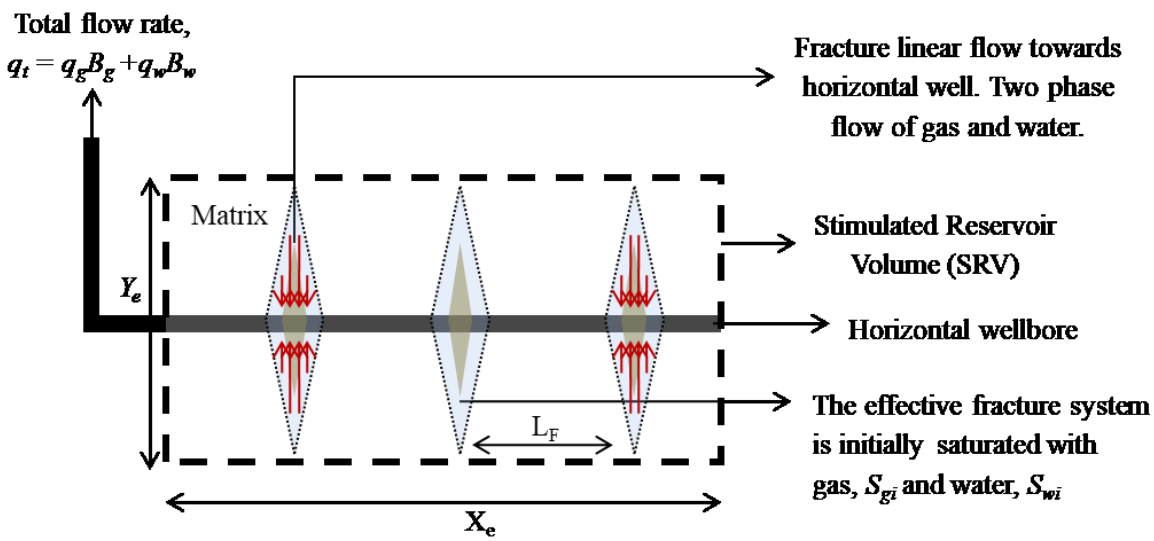

Figure 4.1: Conceptual model for modeling gas and water production during EGP.

4.2.2 Mathematical Derivation

This section presents the mathematical derivation of the flowing MBE, which couples the closed-tank MBE and a two-phase diffusivity equation.

4.2.2.1 Material Balance Equation

Several authors (Rahman et al., 2006a; Moghadam et al., 2011; Singh, 2013) have considered advanced gas MBEs that take into account several drive mechanisms. By defining an effective compressibility term, they were able to retain simplicity of their MBEs. Following a similar approach, a MBE for the gas phase within the fracture network is developed for EGP. The effects of gas and water expansion and fracture closure are lumped into an effective compressibility term ($\tilde{C}_t$). Detailed derivation is presented in Appendix A.

$\tilde{C}_t$ is defined by

$$\tilde{C}_t = \left(1 - \frac{G_p}{G_{fi}}\right)\frac{B_g}{B_{gi}} S_{gi} c_g + \left(1 - \frac{W_p}{W_{fi}}\right) S_{wi} c_w + \frac{1}{V_{fi}}\frac{\partial V_f}{\partial P_f} \tag{4.1}$$

$\tilde{C}_t$ is analogous to c_t in conventional multi-phase well testing (Martin, 1959), but is expressed as a function of measurable flowback parameters including cumulative gas and cumulative water production. It has a unit of [1/pressure] and measures the percentage of fluid released by the fracture system per unit drop in fracture pressure. Each term in $\tilde{C}_t$ represents a drive mechanism during EGP. $\left(1-\frac{G_p}{G_{fi}}\right)\frac{B_g}{B_{gi}}S_{gi}c_g$ and $\left(1-\frac{W_p}{W_{fi}}\right)S_{wi}c_w$ represent free gas and water expansion in fractures, respectively. $\frac{1}{V_{fi}}\frac{\partial V_f}{\partial P_f}$ is similar to the formation compressibility term in conventional material balance analysis. When dealing with fractures, it refers to the inverse of the fracture stiffness, S_f, defined by the elastic or strain energy required to keep a hydraulic fracture open (Craig, 2006).

The final MBE for the fracture system is given by

$$\frac{\partial P_f}{\partial t} = -\frac{q_t}{\tilde{C}_t V_{fi}} \tag{4.2}$$

where q_t is the total flow rate, $q_t = q_g B_g + q_w B_w$.

4.2.2.2 Linear Two-Phase Diffusivity Equation

The diffusivity equation for single-phase gas flow in fractures is given by

$$\nabla\left[\frac{P_f}{\mu_g Z}\nabla P_f\right] = \frac{\varphi_f}{K_f}\frac{P_f}{Z}c_g\frac{\partial P_f}{\partial t} \tag{4.3}$$

Eq. 4.3 can be modified for transient two-phase flow by 1) introducing an explicitly determined gas relative permeability function (k_{rg}), and 2) replacing c_g by $\tilde{C}_t$. Therefore, Eq. 4.3 becomes

$$\nabla\left[\frac{P_f}{\mu_g Z}\nabla P_f\right] = \frac{\varphi_f}{K_f k_{rg}(t)}\frac{P_f}{Z}\tilde{C}_t\frac{\partial P_f}{\partial t} \tag{4.4}$$

Al-Hussainy et al. (1966) defines a gas pseudo-pressure function (ψ) that accounts for pressure-dependent gas properties (i.e. gas compressibility and viscosity).

$$\psi(P_f) = \int_0^{P_f}\frac{2P_f}{\mu_g Z}\partial P_f \tag{4.5}$$

Substituting Eq. 4.5 into Eq. 4.4 gives

$$\nabla^2\psi(P_f) = \frac{\varphi_f}{K_f}\frac{\mu_g\tilde{C}_t}{k_{rg}(t)}\frac{\partial\psi}{\partial t} \tag{4.6}$$

Several authors (Rahman et al., 2006b; Moghadam et al., 2011; Tabatabaie et al., 2013) have introduced the concept of a material balance pseudo-time function (t_a) in dealing with gas flow to account for time-dependent gas properties such as gas viscosity and compressibility. Similarly, t_a is introduced in Eq. 4.7 to account for the change in k_{rg}, $\tilde{C}_t$, and gas viscosity with time.

$$t_a = \int_0^t \frac{k_{rg}(t)}{\mu_g\widetilde{C_t}}\,\partial t \tag{4.7}$$

Finally, the governing equation describing linear two-phase flow in the fracture system is given by

$$\frac{\partial^2\psi(P_f)}{\partial y^2} = \frac{\varphi_f}{K_f}\frac{\partial\psi}{\partial t_a} \tag{4.8}$$

4.2.2.3 Dynamic Relative Permeability Function

Ezulike and Dehghanpour (2014b) developed a procedure for obtaining relative permeability of the effective fracture network as an explicit function of time from flowback data. The procedure considers the effective fracture network as the control volume, and assumes that water production during flowback period comes from the effective fracture network. Therefore, water production with time causes drop in average water saturation in the effective fracture network, which in turn causes a corresponding non-linear increase in hydrocarbon saturation and relative permeability in the fracture network. Detailed description of the DRP is presented in the Appendix B. The authors analyzed field data from tight oil and gas reservoirs, and shale gas reservoirs. They found that the general form of this DPR function is given by

$$k_{rg}(t) = \frac{\beta_1}{1+(\beta_2 t)^{-\beta_3}} \tag{4.9}$$

where k_{rg} is the relative gas permeability for the effective fracture system. β_1, β_2, β_3 are the parameters controlling the rate of water saturation drop in fractures (i.e. fracture clean-up rate).

The values of β_1, β_2, and β_3 can be obtained from history-matching of the flowback data. Here, the DRP function is used in Eq. 4.7 to account for two-phase transient flow in the fracture network.

4.2.2.4 A Flowing Material Balance Equation for Early Gas Production

The flowing MBE for two-phase flowback during EGP is derived by combining Eqs. 4.2 and 4.8. Eq. 4.10 shows the final form of the flowing MBE in this study. Detailed derivation is presented in Appendix C.

$$\frac{\psi(P_i)-\psi(P_{wf})}{q_g{}^*} = \frac{1}{C_{st}} t_a + \frac{1}{C_{st}} Y_D \quad (4.10)$$

where C_{st} is the fracture storage coefficient. $C_{st} = \frac{V_{fi} Z_i}{2P_i}$. Y_D is a dimensionless fracture parameter, $Y_D = \frac{\varphi_f}{K_f} \frac{Y_e{}^2}{3}$. $q_g{}^*$ is the equivalent gas rate, $q_g{}^* = \frac{1}{k_{rg}(t)} \left[q_g B_{gi} + q_w B_w\right]$.

Eq. 4.10 is the final analytical equation describing EGP region in shale gas wells with an extended shut-in period. It is analogous to the rate transient model for early-time single-phase water flow in tight reservoirs (Abbasi et al. 2012; 2014). Theoretically, a plot of the rate normalized pseudo-pressure (RNP) (i.e. $\frac{\psi(P_i)-\psi(P_{wf})}{q_g{}^*}$) vs. t_a should yield a straight line with slope of $\frac{1}{C_{st}}$ and intercept of $\frac{1}{C_{st}} Y_D$. The initial volume of the effective fracture network (V_{fi}) can be calculated from the line slope. The ratio of y-axis intercept and the line slope gives the value of Y_D, which is a function of fracture porosity (φ_f), K_f, and Y_e.

4.3 Analysis Procedure

Below is the analysis procedure for two-phase flowback data analysis in gas shales, using the flowing MBE:

1. Obtain two-phase flowback data (i.e. production rates, pressure, and cumulative production profiles).

2. Construct diagnostic plots to identify flowback regimes: EGP and LGP.

3. Calculate DRP for gas phase following the steps outlined by Ezulike and Dehghanpour (2014b).

4. Calculate ${q_g}^*$ from production rates and DRP.

5. Calculate $\widetilde{C_t}$ from cumulative production profiles.

6. Compute t_a using an appropriate numerical integration technique.

7. Plot RNP vs. t_a corresponding to EGP region.

8. Determine the slope and y-axis intercept of the RNP plot.

9. Calculate C_{st} and V_{fi} from the line slope: $C_{st} = \frac{1}{\text{slope}} = \frac{V_{fi} Z_i}{2P_i}$.

10. Calculate Y_D from the line slope and intercept: $Y_D = \frac{\text{y−axis intercept}}{\text{slope}} = \frac{\varphi_f}{K_f} \frac{{Y_e}^2}{3}$.

4.4 Field Application and Results Discussion

In this section, the proposed analytical model is applied on Wells D and F of the target well pad. The BHP data is obtained from the casing pressure measured at surface using Gray's correlation in the IHS Harmony software. Also, the estimated reservoir and fracture parameters from the RNP plots are briefly discussed.

4.4.1 Field Application

Several questions must be considered while analyzing field data using Eq. 4.10: 1) What is the value of S_{gi}? The actual initial gas saturation in the effective fractures after the shut-in period is unknown in field cases. 2) What is the value of $\frac{1}{V_{fi}} \frac{\partial V_f}{\partial P_f}$? In the proposed model, the effective fracture system has an irregular fracture geometry which includes secondary fractures and pre-existing natural fractures. The value of $\frac{1}{V_{fi}} \frac{\partial V_f}{\partial P_f}$ cannot be obtained either from field or lab data.

A new parameter, leak-off percentage, is introduced in the iteration process to obtain the optimal values of S_{gi} and $\frac{1}{V_{fi}} \frac{\partial V_f}{\partial P_f}$. The leak-off percentage represents the percentage of the TIV lost into the formation (i.e. fractures and matrix) and does not create effective fracture network. The leak-off percentage can be calculated from the pressure decline data (Rogers et al.).

V_{fi} can be estimated using 1) TIV and the leak-off percentage (i.e., V_{fi} = (1- leak-off percentage) × TIV), and 2) the slope of the RNP plot. Here, the values of S_{gi}, leak-off percentage, together with $\frac{1}{V_{fi}}\frac{\partial V_f}{\partial P_f}$ are varied simultaneously to obtain the optimum V_{fi}. The goal-seek function is to minimize the difference between the V_{fi} calculated from both methods.

Figures. 4.2a and 4.2b are RNP plots that shows the field application of the flowing MBE. The change in P_f in the MBE is represented using the change in BHP. The key calculation results are summarized in Appendix D. The plots of RNP vs. t_a show a good linear relationship (i.e. $R^2 > 0.9$), in agreement with the derived analytical equation. Table 4.1 summarizes the outputs from the RNP plots for the two wells.

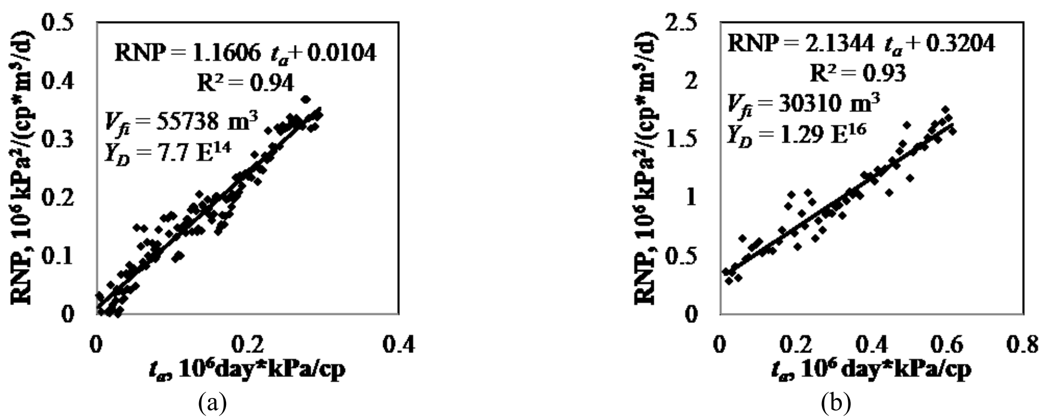

Figure 4.2: Analysis of EGP data using the flowing MBE: RNP vs. t_a for (a) Well D and (b) Well F of the target pad in the HRB.

Table 4.1: Reservoir and fracture parameters estimated from the RNP plots.

Estimated Parameters	Well D	Well F	Unit
Initial Free Gas Saturation (S_{gi})	14.7	25.5	%
Leak-Off Percentage	20	31	%
Fracture Closure Term ($\frac{1}{V_{fi}}\frac{\partial V_f}{\partial P_f}$)	$1.18*10^{-5}$	$2.96*10^{-6}$	kPa^{-1}
Effective Fracture Volume (V_{fi})	55,738	30,310	m^3
Dimensionless Fracture Parameter (Y_D)	$7.7*10^{14}$	$1.29*10^{16}$	-

4.4.2 Results Discussion

S_{gi}: The results of the analysis show significant S_{gi} in the fracture network. The S_{gi} obtained is the average gas saturation initially in the effective fracture network, including secondary and natural fractures. S_{gi} for wells D and F are 14.7 % and 25.5 %, respectively. This is in agreement with findings from the numerical simulation studies in Chapter 2 which show the gradual build-up of gas by forced and counter-current imbibition during the shut-in period (Figure 2.8). This initial free gas in the fracture network is responsible for the instant gas breakthrough observed in many fractured shale gas wells.

Leak-Off Percentage: The leak-off percentage shows the relative volume of fracturing fluid loss into the natural fractures or the matrix during the fracturing operations and the shut-in period. The results show the estimated fluid losses for Wells D and F are 20 % and 31 % of the TIV, respectively. The HR shales, due to its high quartz content, are characterized by a high number of pre-existing natural fractures (Anderson et al., 2013). A significant amount of the fracturing fluid is lost into the existing fractures while a portion is also imbibed into the shale matrix. These two factors and also the gravity segregation may be responsible for the poor water load recovery observed in many shale reservoirs.

$\frac{1}{V_{fi}}\frac{\partial V_f}{\partial P_f}$: $\frac{1}{V_{fi}}\frac{\partial V_f}{\partial P_f}$ is the relative change in effective fracture volume per unit change in fracture pressure. The calculated $\frac{1}{V_{fi}}\frac{\partial V_f}{\partial P_f}$ for Wells D and F are 1.18×10^{-5} kPa^{-1} and 2.96×10^{-6} kPa^{-1}, respectively. The HR shales have a high amount of pre-existing natural fractures (Anderson et al., 2013). Microseismic data from a similar pad drilled in the HRB show extremely complex geometry of the fracture network due to significant amount of pre-existing natural fractures (Virues et al., 2016a). These unpropped natural fractures in the effective fracture network may be one of the reasons for the high value of $\frac{1}{V_{fi}}\frac{\partial V_f}{\partial P_f}$.

V_{fi}: V_{fi} is calculated from the slope of RNP plot. The calculated V_{fi} for Wells D and F are 55,738 m^3 and 31,310 m^3, respectively. The estimated V_{fi} is the total fracture volume contributing to fluid flow, including all active secondary and natural fractures. It may also include fractures from adjacent wells in cases where severe inter-well communication occurs.

Y_D: Y_D is a function of φ_f, K_f, and Y_e. It comes from the ratio of y-axis intercept and the slope of the RNP plot. However, because of the simplifications and assumptions in the conceptual model, the estimated Y_D can only give a qualitative interpretation of the flow capacity of the fractures in comparison to other wells and cannot be used to estimate actual K_f and/or Y_e. The estimation of K_f using early-time data is challenging because of the underlying assumptions in the analytical model.

$V_{fi}S_{gi}$: $V_{fi}S_{gi}$ is calculated from the estimated values of V_{fi} and S_{gi}. For Wells D and F, $V_{fi}S_{gi}$ are estimated to be 8,208 m^3 and 7,731 m^3, respectively, under reservoir conditions; or 1,915 Mm^3 and 1,803.7 Mm^3, respectively, under surface conditions. Flowback profiles show that respectively 1672.4 Mm^3 and 747.2 Mm^3 of gas are produced during EGP phase from Wells D and F, which indicate that 87 % and 41.4 % of the free gas are produced before significant amount of gas influx from the matrix system.

4.5 Limitations

Figures 4.2a and 4.2b show acceptable linear relationships between RNP and t_a, with $R^2 >$ 0.9. However, the data points in Figures 4.2a do not strictly follow the linear relationship, as predicted in Eq. 4.10. In fact, the data points tend to represent a curve with an inflexion point. This is because of the simplifying assumptions made when solving the diffusivity equation. In the calculation procedure presented in Appendix B, the gas formation volume factor is assumed constant during EGP (i.e. $B_g = B_{gi}$) to explicitly solve for ψ and t_a. However, as $B_{gi}/B_g < 1$, such simplification results in overestimation of $q_g{}^*$, and consequently, underestimation of RNP.

Several assumptions are made to simplify and solve the diffusivity equation, such as 1) 1D linear flow in fractures, 2) absence of gravity segregation, 3) negligible fluid influx from the matrix, 4) negligible gas desorption from fracture-matrix interface, and 5) negligible effects of secondary fractures during early-time flowback period. Some assumptions might be further relaxed using advanced mathematical techniques, for example, introducing Langmuir Isotherm to account for gas desorption effect. Furthermore, the effective fracture network is assumed as an arbitrary "two-phase tank" with uniform properties. Although this approximation has an obvious advantage in accounting for the complex fracture geometry, it indeed reduces the accuracy when describing the fracture closure effect. In our analysis, $\frac{1}{V_{fi}}\frac{\partial V_f}{\partial P_f}$ is assumed to be constant during EGP. In fact, the effective fracture network contains hydraulic, secondary and natural fractures which have different geomechanical properties. For example, compared to natural and secondary fractures, hydraulic fractures are less sensitive to the pressure drop due to the existence of high-strength proppants. Existence of natural and secondary fractures may result in changes in $\frac{1}{V_{fi}}\frac{\partial V_f}{\partial P_f}$ with space and/or with time. Therefore, a more accurate fracture closure model with characterization of natural and secondary fractures is suggested for future studies.

4.6 Summary

In this chapter, a flowing material balance equation is developed to describe two-phase flowback during Early Gas Production in shale gas reservoirs. The model assumes that 1) the effective fracture network is initially saturated with free gas and water, and 2) linear flow of gas and water from fracture tip to the wellbore occurs in the fractures. The closed-tank material balance equation derived in Chapter 2 is coupled with a two-phase diffusivity equation to describe early-time transient flow signatures.

The flowing material balance equation is solved by introducing a new pseudo-time function which accounts for the changes in gas relative permeability and gas properties with time. The model gives estimates of the initial volume of the effective fracture network and a dimensionless fracture parameter which measures the flow capacity of the effective fracture network. Finally, the field application is demonstrated by applying the proposed model on the flowback data from two wells completed in the Horn River Basin.

Nomenclature

B	=	formation volume factor, std. volume/res. volume
B_g	=	gas formation volume factor
B_{gi}	=	gas formation volume factor at initial condition
B_w	=	water formation volume factor
B_{wi}	=	water formation volume factor at initial condition
c	=	compressibility, 1/Pa
c_g	=	gas compressibility, 1/Pa
c_w	=	water compressibility, 1/Pa
C_{st}	=	storage coefficient, 1/Pa
$\tilde{C}_t$	=	effective compressibility, 1/Pa
G	=	volume of gas, std. m^3
G_{fi}	=	volume of gas initially in the fractures, std. m^3
G_p	=	cumulative gas production, std. m^3

k_r	=	relative permeability
k_{rg}	=	gas relative permeability
k_{rw}	=	water relative permeability
K	=	permeability, md
K_f	=	fracture permeability, md
L_F	=	fracture spacing, m
P	=	pressure, Pa
P_f	=	fracture pressure, Pa
P_g	=	gas pressure, Pa
P_i	=	initial reservoir pressure, Pa
P_w	=	water pressure, Pa
P_{wf}	=	wellbore flowing pressure, Pa
q	=	rate, m^3/d
q_g	=	producing gas rate, m^3/d
q_g^*	=	equivalent gas rate, m^3/d
q_t	=	total producing rate, m^3/d
q_w	=	producing water rate, m^3/d
S	=	saturation
S_g	=	gas saturation
S_{gi}	=	initial gas saturation
S_w	=	water saturation
S_{wi}	=	initial water saturation

t	=	time, hrs
t_a	=	pseudo time, kPa*hrs/cp
V	=	volume, res. m^3
V_f	=	volume of effective fractures, res. m^3
V_{fi}	=	volume of effective fractures at initial condition, res. m^3
V_g	=	volume of gas in fractures, res. m^3
V_w	=	volume of water in fractures, res. m^3
W	=	volume of water, std. m^3
W_{fi}	=	volume of water initially in fractures, std. m^3
W_p	=	cumulative water production, std. m^3
X_e	=	horizontal length of a MFHW, m
Y_D	=	dimensionless fracture parameter
Y_e	=	equivalent half-length of effective fractures, m
Z	=	gas compressibility factor
Z_i	=	gas compressibility factor at initial conditions
β	=	cleanup indices
φ	=	porosity
φ_f	=	porosity for the fracture system
ψ	=	gas pseudo-pressure, kPa^2/cp
ρ	=	density, kg/m^3
ρ_g	=	gas density, kg/m^3
ρ_g^o	=	gas density at surface condition, kg/m^3
ρ_g^R	=	gas density at reservoir condition, kg/m^3
μ	=	viscosity, cp
μ_g	=	gas viscosity, cp
μ_w	=	water viscosity, cp
$\mathcal{S}_f$	=	fracture stiffness, psi
Δ	=	change

Chapter 5: Effectiveness and Time Variation of Induced Fracture Volume: Lessons from Water Flowback Analysis

This chapter is a modified version of the article Xu et al. (2017) published in *Fuel*. I was responsible for analyzing field data, forming key concepts, developing analytical and numerical models, writing and editing manuscripts. My co-authors assisted in discussing model outputs, reviewing manuscripts, and securing company approvals for publication. The original article was modified by changing the voice from plural first person (we) to singular first person (I). The introduction section was revised to connect with previous chapters and highlight the focus of this chapter. Section 5.2 was modified to remove some repetitive parts that have been presented in Chapter 3.

5.1 Introduction

The closed-tank models presented in Chapters 3 and 4 assume negligible fluid influx from the matrix to the fracture network. Therefore, they are not applicable to the data measured during LGP when fluid influx from the matrix becomes significant. Furthermore, the closed-tank models estimate the initial volume of effective fracture network (V_{fi}) from the EGP data, which are usually recorded during several hundred hours after opening the wells. Thus, the estimated V_{fi} cannot represent the effective fracture volume at later times and/or during the production phase. Flowback period connects the stimulation phase (when the BHP can reach 8,000 psi) with the production phase (when the BHP is usually 1,000 - 2,000 psi). Currently, there are several key questions regarding the hydraulic fracturing operations: Will the effective fracture volume change during flowback? If yes, what are the reasons behind it? What are the potential impacts on hydrocarbon production?

This chapter extends the closed-tank MBE by developing an open-tank MBE for analyzing the rate and pressure data measured during LGP. The open-tank model also considers the effective fracture network as a tank of arbitrary geometry, but includes fluid (gas + water) influx from the matrix as an additional drive mechanism. It estimates the fracture-matrix interface area of the effective fracture network (A_{mf}) in a manner similar to water influx models in conventional reservoirs (Van Everdingen and Hurst, 1949; Ahmed, 2010). The open-tank MBE is verified against a 2D synthetic case using the CMG software, and is applied on the target well pad. Finally, a volumetric comparative analysis is performed based on the model outputs to investigate the change of effective fracture volume during flowback period.

The rest of this chapter is organized as follows: Section 5.2 clarifies the limitations of the closed-tank MBE presented in Chapter 3. Section 5.3 derives the open-tank MBE. Section 5.4 validates the open-tank model against a numerical case using the CMG software. Section 5.5 proposes a workflow for two-phase flowback data analysis in gas shales. Section 5.6 demonstrates field application of the open-tank model and discusses the model outputs based on a comprehensive volumetric analysis. Section 5.7 lists the limitations of the open-tank model, and Section 5.8 summarizes this chapter.

5.2 Limitations of the Closed-Tank Model

Chapter 3 presents a closed-tank MBE to estimate V_{fi} by using EGP data. The control volume is the effective fracture network of arbitrary geometry. Three drive mechanisms during EGP (i.e. expansion of initial gas in fractures, expansion of initial water in fractures, and fracture closure) are considered in the MBE. Eq. 3.10 is the final form of the closed-tank MBE. Detailed derivation is presented in Section 3.2.

Figure 5.1 shows the results of analyzing the flowback data of the target pad using Eq. 3.10. It should be noted that both the initial gas saturation in fractures (S_{gi}) and the fracture compressibility (c_f) are unknown in field cases. It should also be noted that c_f describes fracture closure effect and is similar to the $\frac{A_f}{S_f}\frac{1}{G_{fi}B_{gi}}$ term in Eq. 3.10. Here, the *Solver* module in Excel is used to find the optimal values of S_{gi} and c_f. The objective function is to obtain the maximum R^2 of the straight line for the EGP part of the data. Eqs. 5.1 - 5.4 describe the search spaces (i.e. constraints) for the unknown parameters. These search spaces are chosen based on literature review (Aguilera, 2008; Makhanov et al., 2014; Ezulike et al., 2016). The Generalized Reduced

Gradient (GRG) nonlinear solving method is used since the optimization process includes multiple variants. The results of optimization are presented in Figure 5.1.

$$10^{-5}\ \text{psia}^{-1} < c_f < 10^{-4}\ \text{psia}^{-1} \tag{5.1}$$

$$5\ \% < S_{gi} < 30\ \% \tag{5.2}$$

$$20\ \%\ \text{TIV} < V_{fi} < 100\%\ \text{TIV} \tag{5.3}$$

$$0 < G_{fi} < G_p^{*} \tag{5.4}$$

where TIV is the total volume of water injected into the formation. G_{fi} is the volume of initial free gas in the effective fracture network, at standard conditions. G_p^* is the volume of initial gas in the effective fracture network, obtained from the p/Z plot (see Figure 2.13).

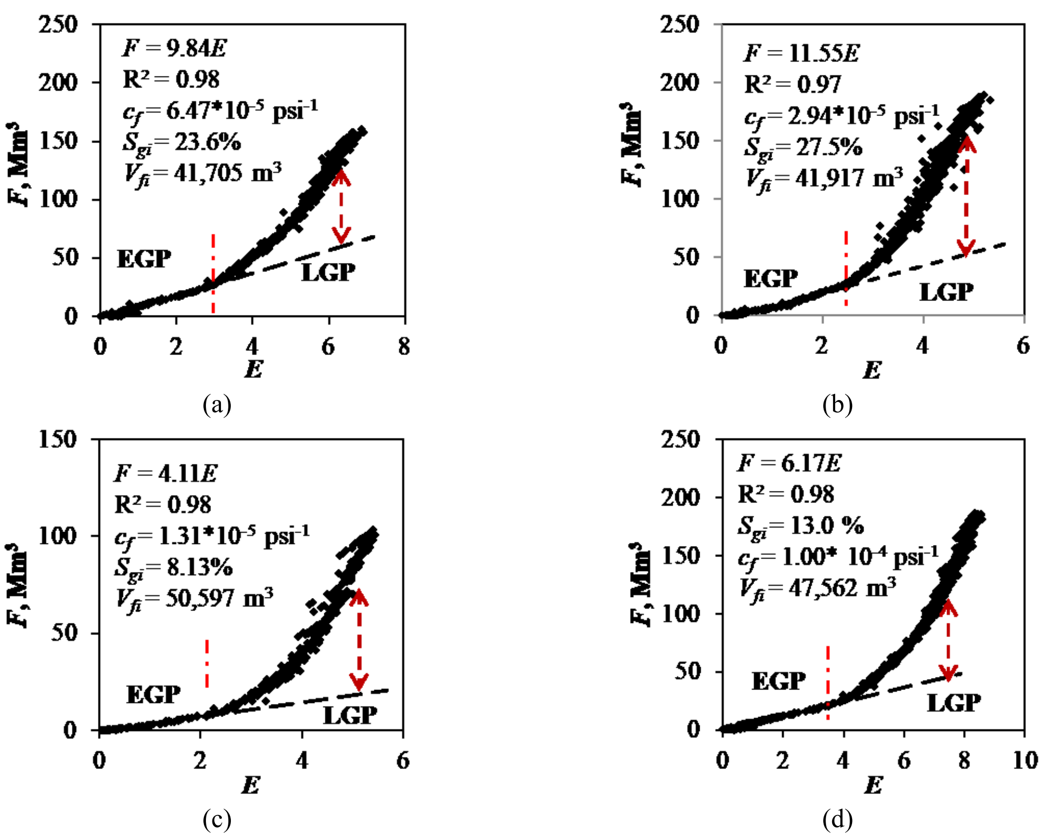

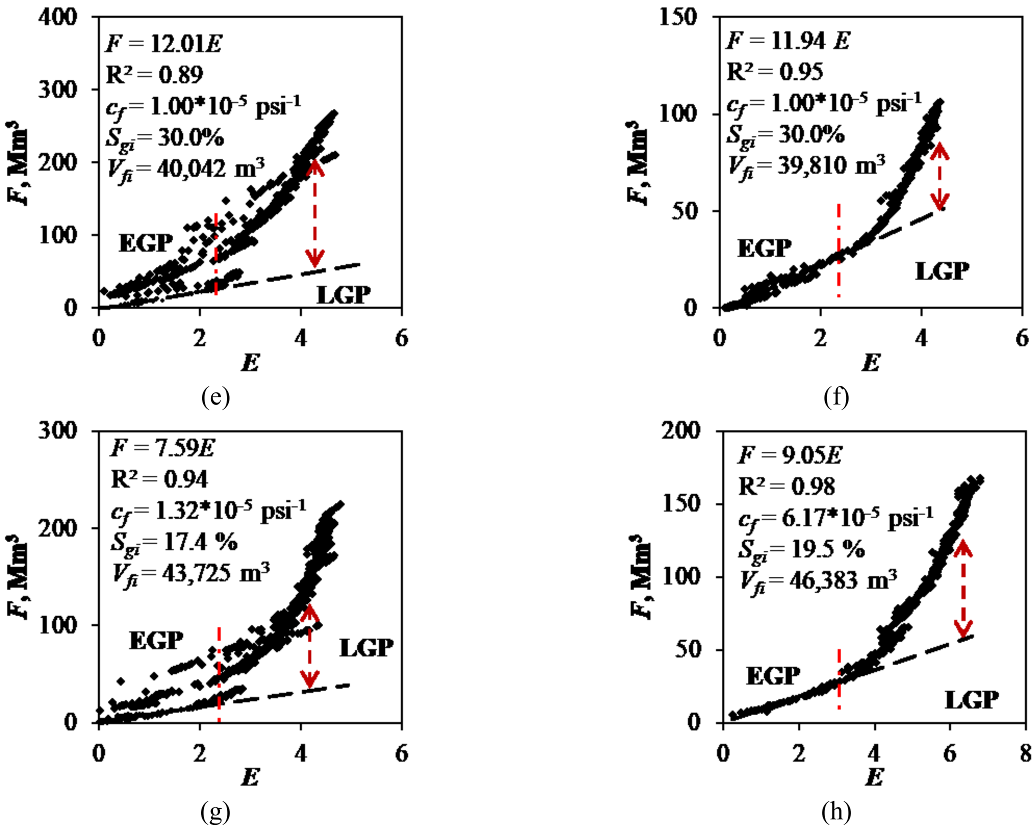

Figure 5.1: Application of the closed-tank MBE on the target well pad in the HRB. Plot (a) to (h) corresponds to Wells A to H, respectively. The plot of *F* vs. *E* for all wells shows a straight line passing through the origin during EGP, followed by an upward deviation during LGP.

Based on Eq. 3.10, during EGP, F vs. E should be a straight line passing through the origin. During LGP, however, the plot of F vs. E shows an upward deviation from the initial straight line (shown by red arrows in Figure 5.1). Figure 5.1 indicates that the closed-tank MBE is not applicable for LGP. The simulation study presented in Chapter 2 proves that a significant amount of gas from the matrix kicks into the effective fracture network during LGP, resulting in an increase in average gas saturation in fractures, an increase in gas flow rate, and consequently an increase in the GWR. In simple, the effective fracture network no longer behaves like a "closed tank" during LGP phase. Instead, it behaves like an "open tank" receiving fluid influx from the surrounding matrix. In the subsequent sections, the closed-tank MBE will be extended to an open-tank one by accounting for fluid influx from matrix during LGP.

5.3 Open-Tank Material Balance Equation: An Extension of the Closed-Tank Model

This section derives an open-tank MBE to analyze rate and pressure data during LGP by incorporating fluid influx from the matrix as a drive mechanism. The effects of water and gas influx from the matrix are described in Sections 5.3.1 and 5.3.2, respectively. The open-tank MBE is analogous to the models developed for conventional gas reservoirs with water influx (Van Everdingen and Hurst, 1949; Ahmed, 2010). It estimates the A_{mf} of a fracture network from the rate and pressure data measured during LGP.

The control volume of the open-tank model is the effective fracture network, which includes all hydraulic, secondary and natural fractures contributing to flow towards the wellbore. During LGP, the drive mechanisms for gas and water production include 1) expansion of gas in fractures, 2) expansion of water in fractures, 3) fracture closure, 4) gas influx from the matrix, and 5) water influx from the matrix. Previous studies show that early-time gas production primarily comes from the free gas stored in the pore space. Gas production from other sources, such as desorption gas and solution gas, is negligible during early time (Cipolla et al., 2010; Yu and Sepehrnoori, 2014). Therefore, only free gas production is considered in our model.

The open-tank MBE, which incorporates the effects of gas and water influx from the matrix, is given by

$$G_pB_g + W_pB_w = G_{fi}B_{gi}\left[\left(\frac{B_g}{B_{gi}} - 1\right) + \frac{(1-S_{gi})c_w + c_f}{S_{gi}}\Delta P_f\right] + G_{in}B_g + W_{in}B_w \qquad (5.5)$$

where G_p and W_p are the cumulative gas and water production, respectively. B_g and B_w are the gas and water formation volume factor, respectively. B_{gi} is the gas formation volume factor at initial conditions. c_w and c_f are water and fracture compressibility, respectively. G_{in} and W_{in} are the cumulative gas and water influx from the matrix at standard conditions, respectively.

Similar to Eq. 3.7, one can simplify Eq. 5.5 using Underground Withdrawal (F) and Expansion Coefficient (E):

$$F = G_{fi}B_{gi}[E] + G_{in}B_g + W_{in}B_w \qquad (5.6)$$

where $F = G_pB_g + W_pB_w$ and $E = \left(\frac{B_g}{B_{gi}} - 1\right) + \frac{(1-S_{gi})c_w + c_f}{S_{gi}}\Delta P_f$.

When fluid influx from the matrix is negligible (i.e. $G_{in}B_g+W_{in}B_w = 0$), Eq. 5.6 simplifies to Eq. 3.10. The open-tank MBE explains the flowback signatures observed in Figure 5.1. During EGP, the effective fracture network behaves like a "closed tank" with negligible fluid support from the matrix. Therefore, the plot of F vs. E shows a straight line passing through the origin with the slope of $G_{fi}B_{gi}$. During LGP, the effective fracture network behaves like an "open tank" receiving significant fluid support from the surrounding matrix. Therefore, the plot of F vs. E shows an upward deviation from the initial straight line. Assuming constant c_f values during flowback, the upward deviations (shown by the red arrows in Figure 5.1) represent cumulative fluid (gas + water) influx from the matrix into the effective fracture network.

5.3.1 Water Influx from the Matrix

During hydraulic fracturing and the following shut-in periods, part of the fracturing water leaks off into the matrix (Holditch, 1979). In low-permeability gas reservoirs (such as shales and tight sandstones) with sub-irreducible water saturation, the formation imbibes the water in a sponge-like fashion (Bennion et al., 1994). The imbibed water increases the water saturation in the matrix. At saturations lower than the irreducible water saturation, water can be assumed to be immobile. However, several challenging questions remain to be answered: How much water imbibes into the matrix? What will be the corresponding water saturation in the invaded zone of matrix? Will the imbibed water become mobile and recoverable? Previous studies show that the imbibed water volume is related to capillary pressure, rock mineralogy, depositional environment, as well as pore structure (Makhanov et al., 2014; Shen et al., 2016). It is generally believed that in water-wet shales, the imbibed water can hardly be recovered, mainly because of the capillary pressure effect. Bertoncello (2014) conducted core flood experiments on shale samples to investigate the recovery of the imbibed water. To mimic the fracturing and flowback processes, water was first injected into a gas-saturated core plug for 51 days. Then, the water injection was stopped and gas was injected from the other side of the core. The results show that the injected water could not be recovered during the flowback process.

The HR shales in this study are expected to be water-wet with initial water saturation of less than 25 % (B.C. Oil & Gas Commission, 2014). Mercury Injection Capillary Pressure (MICP) data and nitrogen adsorption-desorption experiments show that the majority of pores are in the size range of 2-10 nm (Harris and Dong, 2013). The high capillary pressure associated with such tiny pores is the main reason for severe water trapping in shale matrix, evidenced by the low water recovery (< 25 %) (Abbasi, 2013; Makhanov et al., 2014; Ghanbari et al., 2016). Therefore, in this study, it is assumed that the imbibed water is trapped in the matrix and is immobile, and thus, water influx from the matrix is negligible (i.e. $W_{in}B_w = 0$).

5.3.2 Gas Influx from the Matrix

Figure 5.2 schematically illustrates a stimulated reservoir volume with an irregular effective fracture network. The irregular fracture network can be simplified using a series of slit-like fractures, as shown in the inset plot. Solid arrows indicate that the direction of gas flow from the matrix to each fracture segment is perpendicular to the fracture plane.

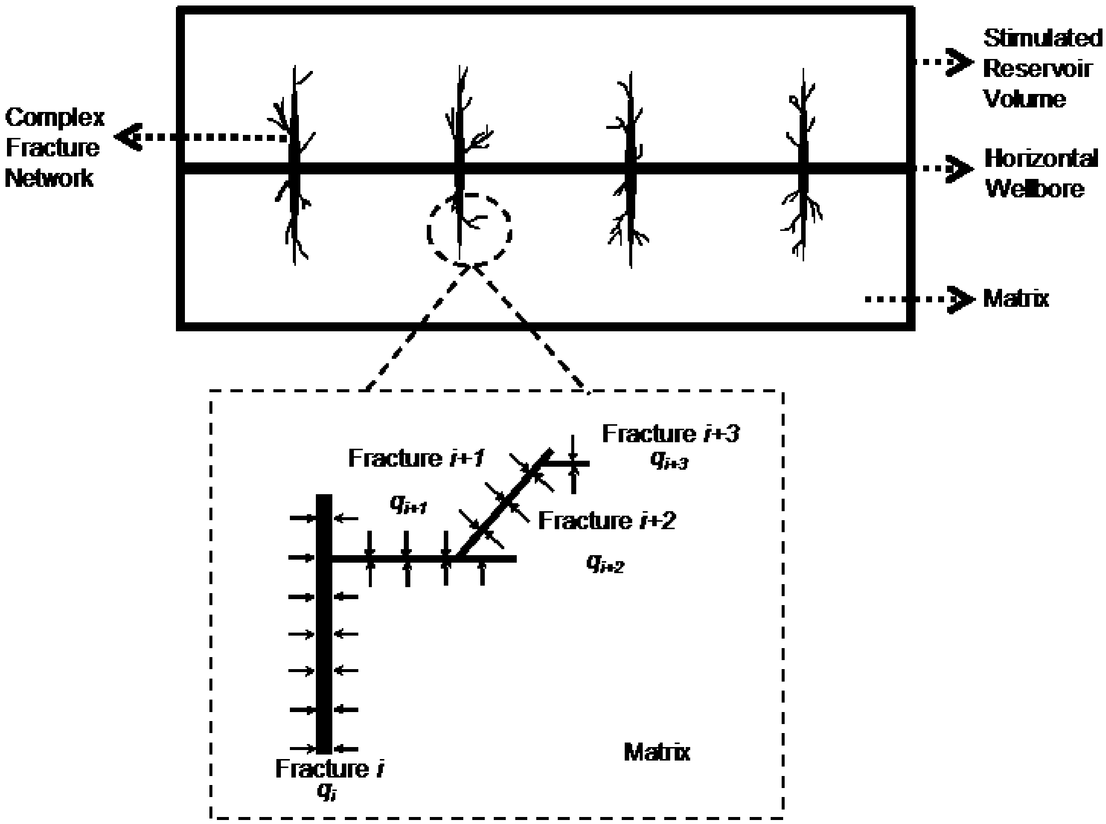

Figure 5.2: Schematic of gas influx from the matrix to an irregular effective fracture network. The effective fracture network is simplified using a series of slit-like fractures in the inset plot. Solid arrows indicate the direction of gas flow from the matrix to the effective fracture network. (Modified from Zolfaghari et al., 2015).

During LGP, gas flows from the matrix to the effective fracture network due to the pressure gradient between the two media. As shown in Figure 5.2, total rate of gas influx (q_{in}) to the effective fracture network is the sum of the gas flow rate to each fracture segment (q_i), which is given by Darcy's Law:

$$q_{in} = \sum q_i = \sum (\frac{k_g A}{\mu_g} \nabla P_m)_i = \sum (\frac{k_{rg} k_m A}{\mu_g} \nabla P_m)_i \tag{5.7}$$

where k_m and k_g are the absolute matrix permeability and the gas effective permeability, respectively. k_{rg} is the gas relative permeability, defined as the ratio of k_g to k_m, $k_{rg} = k_g/k_m$. μ_g is the gas viscosity. A_i is the fracture-matrix interface area of the i^{th} fracture segment. ∇P_m is the pressure gradient between the matrix and the effective fracture network, at the fracture-matrix interface.

Relative permeability describes the ability of a porous medium to transmit one phase in the presence of another phase, and is usually described as a function of water saturation. In the proposed model, all imbibed water is assumed to be trapped in the matrix during flowback (see discussion in Section 5.3.1). Therefore, water saturation in the matrix and the corresponding relative permeability remain constant during flowback period. With further assumption that ∇P_m for all fractures is the same, Eq. 5.7 becomes

$$q_{in} = \sum\left(\frac{k_{rg}k_mA}{\mu_g}\nabla P_m\right)_i = \frac{k_{rg}k_m}{\mu_g}\sum A_i\nabla P_m = \frac{k_{rg}k_m}{\mu_g}A_{mf}\nabla P_m \tag{5.8}$$

where A_{mf} is the fracture-matrix interface area of the irregular effective fracture network, $A_{mf} = \sum A_i$.

Eq. 5.8 indicates that q_{in} primarily depends on A_{mf}. Based on the assumptions, q_{in} for an irregular-shaped fracture network is the same as that for a regular-shaped fracture network with the same A_{mf}. Thus, it is reasonable to model gas influx effect from the matrix using a regular fracture geometry. Here, the simplest gas diffusivity equation (El-Banbi and Wattenbarger, 1998; Bello, 2009) is modified to calculate G_{in}.

The diffusivity equation for 1D, single-phase gas flow is given by

$$\frac{\partial^2 m(P_m)}{\partial x^2} = \frac{\phi_m}{k_m}\frac{\partial m(P_m)}{\partial t_a} \tag{5.9}$$

where P_m and ϕ_m are the matrix pressure and porosity, respectively. m and t_a are the pseudo-pressure and pseudo-time functions defined for pressure- and time-dependent gas properties, respectively (Agarwal et al., 1999; Mattar and Anderson, 2005):

$$m(P_m) = \int_0^{P_m}\frac{2P_m}{\mu_g Z}dP_m \tag{5.10}$$

$$t_a = \int_0^t\left(\frac{1}{\mu_g c_t}\right)_m dt \tag{5.11}$$

where Z is the gas compressibility factor, c_t is the total compressibility of the effective fracture system.

Eq. 5.11 should be modified to account for the existence of water in the matrix, which includes both initial formation water and the imbibed water. Although water is assumed to be immobile in the matrix in our model, it occupies part of the pore space and affects the relative permeability of gas phase. Eq. 5.9 is modified by introducing the gas saturation (S_g) and k_{rg} in the matrix:

$$\frac{\partial^2 m(P_m)}{\partial x^2} = \frac{\phi_m S_g}{k_m k_{rg}} \frac{\partial m(P_m)}{\partial t_a} \tag{5.12}$$

Assuming constant $\mu_g c_t$ during flowback period, Eq. 5.12 becomes

$$\frac{\partial^2 m(P_m)}{\partial x^2} = \frac{\phi_m S_g \mu_g c_t}{k_m k_{rg}} \frac{\partial m(P_m)}{\partial t} \tag{5.13}$$

Eq. 5.13 is solved using constant fracture pressure boundary conditions. Detailed derivation is presented in Appendix E.

The dimensionless gas influx rate (q_D) in Laplace space is given by

$$\overline{q_D} = \frac{1}{\sqrt{s}} tanh(\sqrt{s}\,) \tag{5.14}$$

where s corresponds to the dimensionless time, t_D. t_D and q_D are defined as

$$t_D = \frac{k_m k_{rg}}{\phi_m S_g \mu_g c_t} \frac{1}{\left(\frac{L}{2}\right)^2} t \tag{5.15}$$

$$q_D = \frac{q_{in}^{SC} T P_{sc} L}{T_{sc} k_g A_{mf} \,[m(P_i) - m(P_f)]} \tag{5.16}$$

where P_{SC} and T_{SC} represent standard pressure and temperature, respectively. q_{in}^{SC} the is rate of gas influx at standard conditions.

To calculate q_{in}^{SC}, Eq. 5.16 should be numerically inverted from Laplace space to real time space using Stehfest's algorithm (Stehfest, 1970). Finally, G_{in} is estimated by integrating q_{in}^{SC} over time:

$$G_{in} = \int_0^t q_{in}^{sc} dt \tag{5.17}$$

It is worth noting that fracture interference is neglected in deriving the equations. This is because fracture interference is rarely observed during flowback period, since 1) the duration of the flowback period is short, and 2) the shale matrix has ultra-low permeability for pressure transmission (Meyer et al., 2010; Clarkson and Williams-Kovacs, 2013).

5.4 Numerical Validation

In this section, the proposed open-tank model is verified against a 2D numerical model in the CMG software. It should be noted that since the closed-tank MBE presented in Chapter 3 is a simplified scenario of the open-tank model (i.e. when cumulative fluid influx is negligible at early-time flowback), the numerical model also verifies the closed-tank MBE. That is to say, the contents of Section 3.3 have been moved and combined here.

5.4.1 Model Configuration

Figure 5.3a shows the 3D view of the numerical model, which has dimensions of 100 m × 200 m × 20 m. The numerical model simulates part of a stimulated reservoir with a horizontal well and four fractures. The fractures are placed perpendicular to the wellbore with a spacing of 25 m. Local Grid Refinement (LGR) is used to capture the fluid flow characteristics near the fracture-matrix interface. To illustrate an irregular effective fracture network, different aperture sizes and different fracture half-lengths are assigned for the four fractures. Although grid refinement is used near the fracture face throughout whole reservoir length (200 m), only the highlighted parts are assigned the fracture properties and are considered as "fractures" (shown as pink lines in Figure 5.3b). The V_{fi} and A_{mf} of the designed fractures are calculated to be 46 m^3 and 20,000 m^2, respectively.

Table 3.1 lists the basic reservoir and fracture properties used in the simulation model. Figure 5.4 shows the gas PVT properties, capillary pressure and relative permeability functions used in the numerical model. The capillary pressure (Figure 5.4b) for the shale matrix is calculated using an empirical correlation proposed by Gdanski et al. (2009). The relative permeability curves for the shale matrix (Figure 5.4c) are provided by Nexen Energy ULC operating the target formation. Figure 5.4d shows the linear relative permeability relationship for the fracture system used in the numerical model.

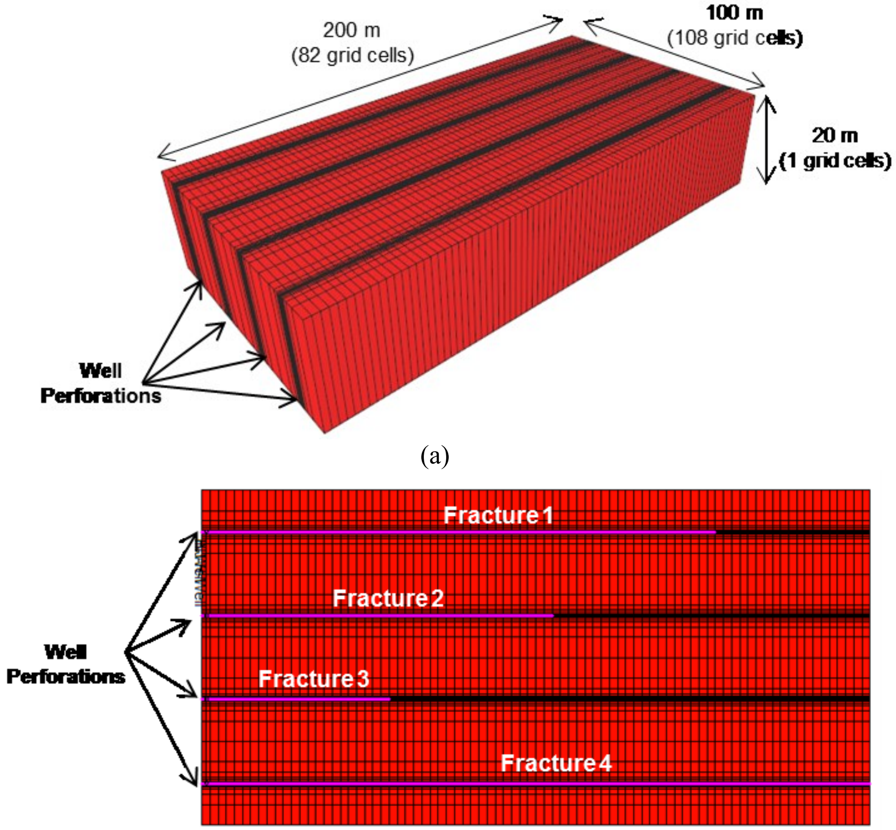

(a)

(b)

Figure 5.3: (a) 3D and (b) 2D view of the numerical model. The pink lines highlight the four fractures with different half-lengths

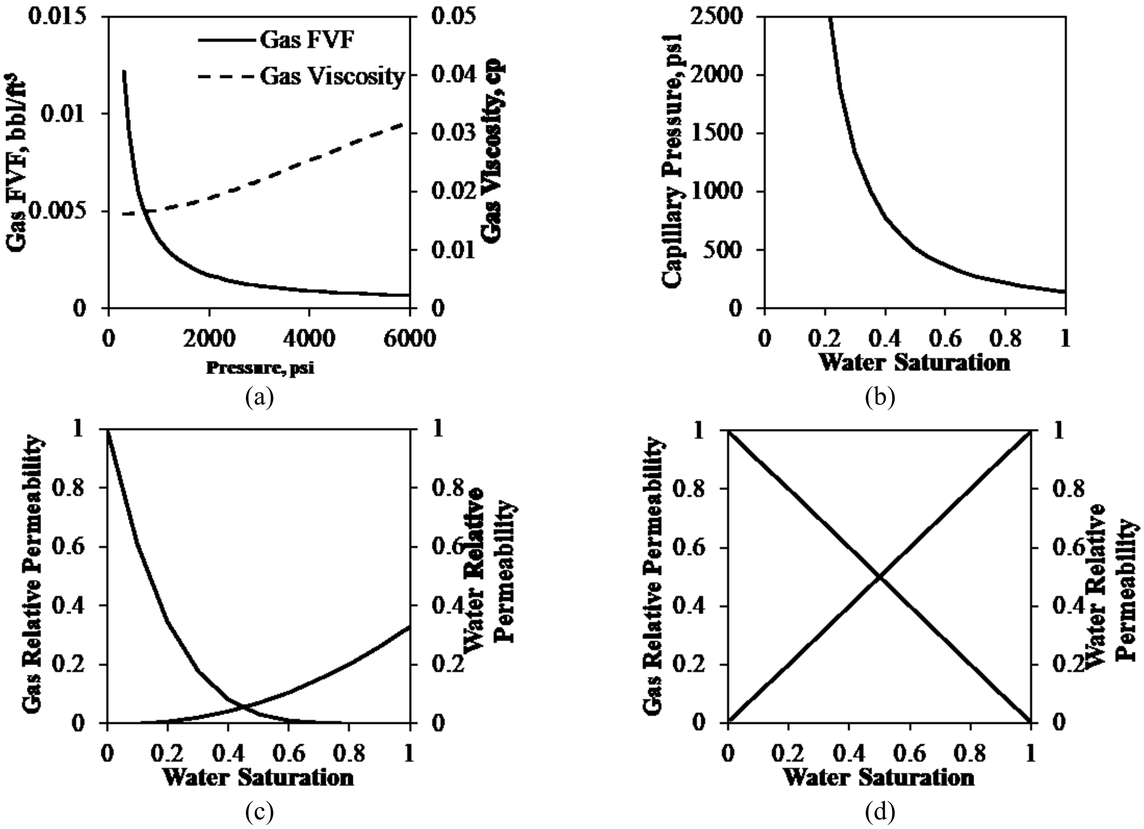

Figure 5.4: Reservoir and fluid properties used in the numerical model: (a) Gas PVT properties, (b) capillary pressure for shale matrix, (c) relative permeability for matrix, and (d) relative permeability for fractures.

Table 5.1: Reservoir and fracture parameters used in the numerical simulation model.

Parameters	Value	Unit	Parameters	Value	Unit
Initial Reservoir Pressure	3000	psi	Aperture of Fracture 1	10	mm
Reservoir Temperature	300	F	Aperture of Fracture 2	5	mm
Initial Water Saturation	0.2	-	Aperture of Fracture 3	2	mm
Rock Compressibility	10^{-5}	psi^{-1}	Aperture of Fracture 4	1	mm
Fracture Porosity	0.8	-	Half-Length of Fracture 1	150	m
Fracture Permeability	2000	mD	Half-Length of Fracture 2	100	m
Matrix Porosity	0.08		Half-Length of Fracture 3	50	m
Matrix Permeability	0.0005	mD	Half-Length of Fracture 4	200	m

5.4.2 Model Initialization

The shut-in and flowback processes are simulated following a similar approach presented in Chapter 2. The four fractures are initially filled with water and an injection well with four perforation cells is used to increase the BHP to a maximum of 7,000 psi. The injection period lasts for 5 days. A total of 400 bbl of water is injected into the formation. Then the well is shut for 30 days for pressure and fluid redistribution. During the shut-in period, gas saturation in the fractures increases gradually due to counter-current imbibition. By the end of shut-in period, the average gas saturation in the fracture network reaches to 46.2 % (i.e. S_{gi} = 46.2 %). Then, the production well is opened at a constant flow rate of 50,000 ft^3/d for one month. Rate and pressure data are hourly recorded during flowback.

5.4.3 Simulation Results

Figure 5.5 shows the GWR and *p/Z* plots of the simulated flowback data. In the *p/Z* plot, *p* is the average fracture pressure. Similar to the field observations and numerical results discussed in Chapter 2, the diagnostic plots suggest two flow regimes: EGP phase with decreasing GWR and a sharp linear drop of p/Z value, and LGP phase with increasing GWR and a gradual decline of p/Z value.

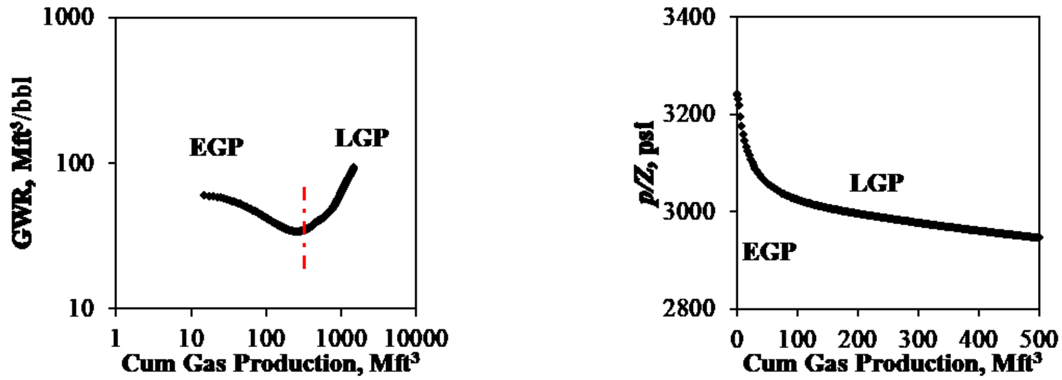

(a) (b)

Figure 5.5: Diagnostic plots of the simulated flowback data: (a) GWR plot and (b) *p/Z* plot. The diagnostic plots show two different flow regimes: EGP and LGP.

5.4.4 Validation of the Open-Tank Model

The open-tank model is verified by comparing the F values calculated from the simulated flowback data and from the open-tank MBE. Figures 5.6a and 5.6b show the plot of F vs. E on Cartesian and logarithmic coordinates, respectively. The black dots in Figures 5.6 are the F values calculated from the simulated rate and pressure data by using $F = G_pB_g+W_pB_w$. The profile of E during flowback period is calculated from the P_f profile and fluid properties. Similar to Figure 5.1, Figures 5.6a shows that the plot of F vs. E initially shows a straight line passing through the origin during EGP, followed by an upward deviation during LGP. The red dots in Figures 5.6 represent the F values calculated from the proposed open-tank MBE. $G_{fi}B_{gi}$ is first calculated using $G_{fi}B_{gi} = V_{fi}\emptyset_f S_{gi}$. After 30 days shut-in, $G_{fi}B_{gi}$ turns out to be 17 m^3. Then, the values of $G_{in}B_g$ is assumed to be zero during the EGP phase; while during the LGP phase, $G_{in}B_g$ is calculated with the assigned A_{mf} using Eqs. 5.9 - 5.17. Finally, Eq. 5.6 is used to calculate the F values from the estimated $G_{fi}B_{gi}$ and $G_{in}B_g$.

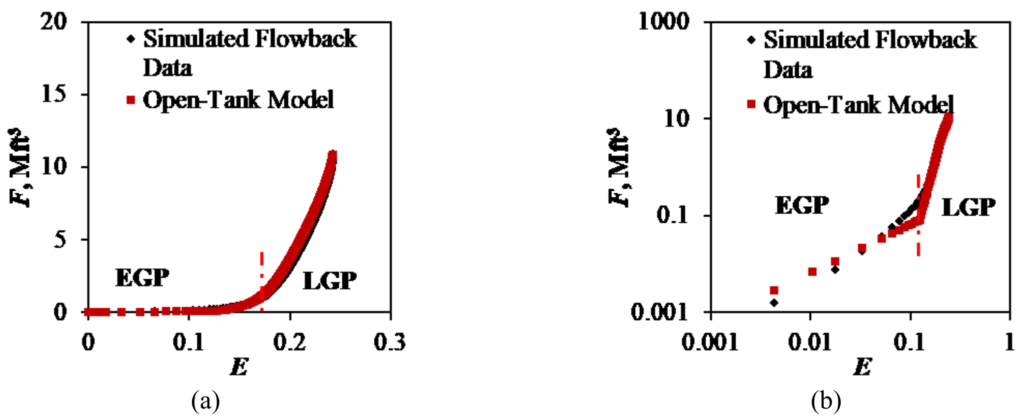

Figure 5.6: Validation of the open-tank MBE against a 2D numerical case. (a) The *F* vs. *E* plot shows a good match between the simulated flowback data and the open-tank model, and (b) Log-log plot of *F* vs. *E* shows some discrepancies at the transition period between EGP and LGP.

Figure 5.6a shows a good match between the black and red dots, in both EGP and LGP. However, Figure 5.6b shows that there are some discrepancies during the transition period between EGP and LGP. The discrepancies might be due to the simplification of the open-tank model. In the proposed model, it is assumed that once water is imbibed into the shale matrix, it will be trapped in the matrix and can no longer be recovered. However, this assumption is invalid in the numerical simulation. The relative permeability functions used in the simulation cannot fully capture the water trapping behavior in shale matrix. In other words, some of the imbibed water in the matrix might flow back to fractures, resulting in the discrepancies observed in Figure 5.6b. In general, Figure 5.6 shows that the *F* values calculated from the open-tank MBE matches well with the ones calculated from the simulated flowback data, and thus verifies the open-tank MBE.

5.5 Workflow

A workflow is proposed to analyze two-phase (gas + water) rate and pressure data during flowback period in gas shales. The workflow is summarized as below.

1. Obtain two-phase flowback data for the target well (i.e. casing pressure, BHP, rates, and cumulative production profiles).

2. Identify flow regimes (i.e. EGP and LGP) by constructing diagnostic plots (such as GWR plots, p/Z plots).

3. Calculate F from the cumulative production profiles using Eq. 3.8.

4. Calculate E using Eq. 3.9.

5. Plot F vs. E on Cartesian coordinates.

6. Analysis of EGP data:

a. Determine the initial line slope of the material balance plot (step 5). Interpret the line slope as $G_{fi}B_{gi}$.

b. Calculate V_{fi} using Eq. 3.10.

7. Analysis of LGP data:

a. Calculate $m(P_f)$, t_D, and $\overline{q_D}$ using Eq. 5.10, Eq. 5.15, and Eq. 5.14, respectively.

b. Inverse $\overline{q_D}$ to real-time space using Stehfest's algorithm (Stehfest, 1970).

c. Assume a value for A_{mf}.

d. Calculate q_{in}^{SC} and G_{in} using Eq. 5.16 and Eq. 5.17, respectively.

e. Calculate $G_{in}B_g$ for each time period based on the BHP profile.

f. Calculate two-phase production index (F') from the semi-analytical model using the estimated $G_{fi}B_{gi}$ (step 6a), E (step 4) and $G_{in}B_g$ (step 7e), $F' = G_{fi}B_{gi}[E]+G_{in}B_g$.

g. Plot F' vs. E on Cartesian coordinates.

h. Iteratively adjust A_{mf} until the best match is obtained between the values of F (step 3) and F' (step 7f).

5.6 Field Application and Results Discussion

In this section, the proposed workflow is first applied on the target well pad. Then, a comparative analysis is conducted to investigate the change of effective fracture volume with time during flowback.

5.6.1 Field Applications

The proposed workflow is applied on six wells (i.e. Wells A, B, C, D, F, and H) of the target well pad. Wells E and G are not included due to poor data quality. The BHP profile, which is calculated from the measured casing pressure using Gray's correlation (Gray, 1978), is used to approximate the average fracture pressure, as done similarly in previous studies (Xu et al., 2015; Fu et al., 2017).

Calculating t_D using Eq. 5.15 requires prior knowledge of ϕ_m, k_m, k_{rg}, and S_g (or S_w), which are unknown for field cases. ϕ_m and k_m are basic rock properties describing the ability of the shale matrix to store and transmit the fluids, respectively. However, for gas shales, it is usually difficult to measure the ϕ_m and k_m values accurately (Heller et al., 2014). Hall et al. (2011) measured the ϕ_m and k_m values for core samples from five wells in the MU formation. Total porosity (including clay-bound water) varies from 1.4 % to 10.9 %, with average value of 6.3 %. The effective matrix permeability varies from 1.04×10^{-10} md to 1.99×10^{-4} md, with average value of 3.59×10^{-7} md. Furthermore, the relationship between k_{rg} and S_g (or S_w) for unconventional rocks is not fully understood due to their low permeability, torturous pore structure, mix-wet behavior, as well as complex fluid flow mechanisms (Javadpour, 2009).

In this study, the four unknown parameters (ϕ_m, k_m, k_{rg}, and S_g) are lumped into two groups, k_mk_{rg} and ϕ_mS_g. k_mk_{rg} and ϕ_mS_g are considered as two unknown variables in the iteration process. Based on the experimental results and geological survey of the HR shales (Hall et al., 2011; Chalmers et al., 2012; Harris and Dong, 2013), the search spaces for k_mk_{rg} and ϕ_mS_g are set to be 5 - 50 nD and 3 - 8 %, respectively. The initial guesses for k_mk_{rg} and ϕ_mS_g are set to be 25 nD and 5 %, respectively. The GRG nonlinear solving method in the *Solver* module is used to obtain the optimal values of k_mk_{rg}, ϕ_mS_g, and the corresponding A_{mf}.

Figure 5.7 presents the results of applying the proposed workflow on six wells of the target pad. The black and red dots represent the two-phase (gas + water) production index calculated from the production data (F) and that from the semi-analytical solution (F'), respectively. The outputs of the workflow include 1) V_{fi} and c_f from EGP part of the data and 2) k_mk_g, ϕ_mS_g and A_{mf}

from the LGP part of the data. Table 5.2 summarizes the outputs from the material balance analysis. The physical meaning and the values of these outputs are discussed below.

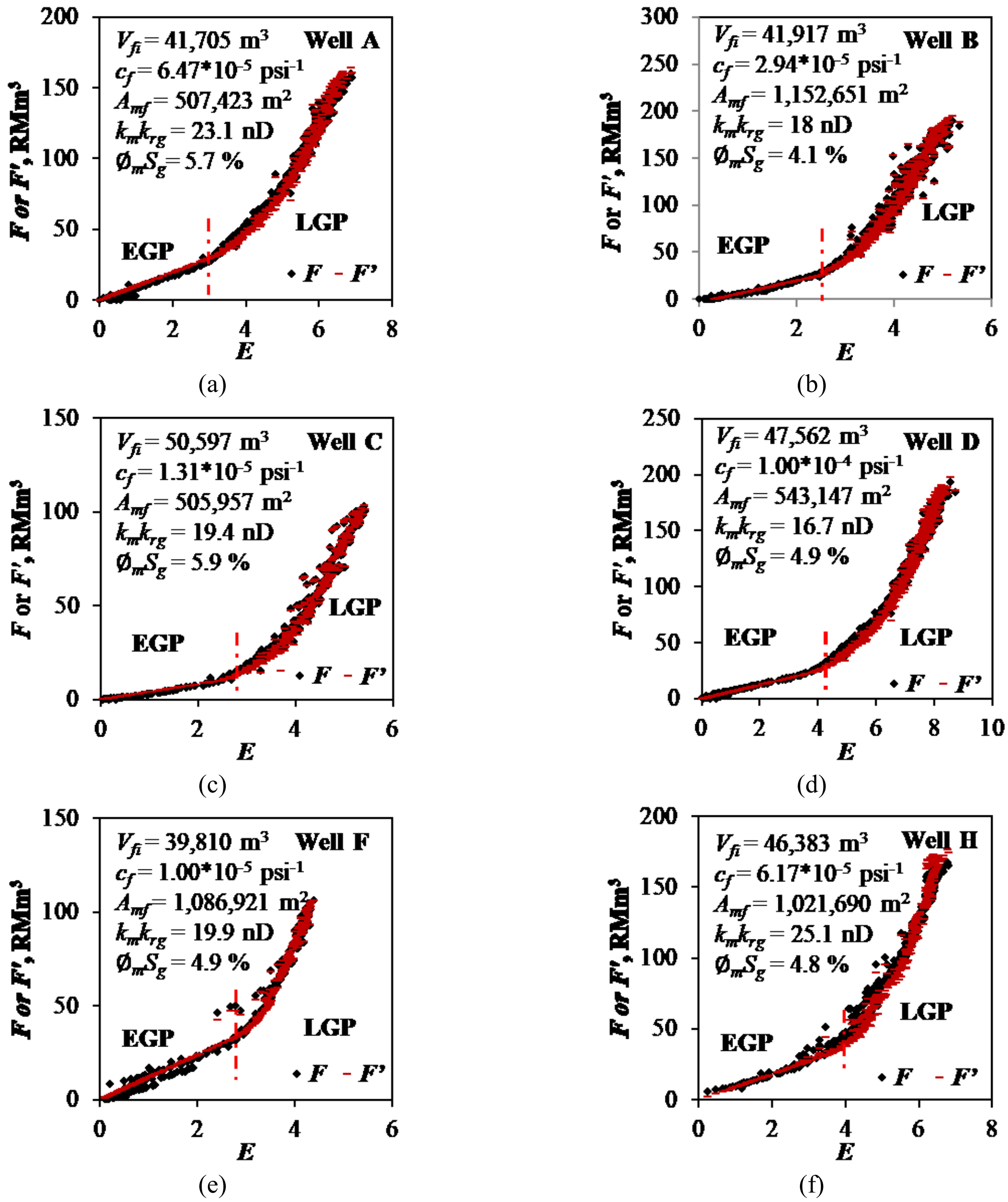

Figure 5.7: The results of applying the proposed workflow on six wells (Wells A, B, C, D, F and H) of the target pad in the HRB. The black points are two-phase production (*F*) calculated from the field data from the target pad. The red points are the calculated two-phase production index (*F'*) calculated from the semi-analytical model. The outputs of the analysis include: 1) V_{fi} and c_f from EGP, and 2) $k_m k_g$, $\phi_m S_g$, and A_{mf} from LGP.

Table 5.2: The values of estimated reservoir and fracture parameters for the target pad.

Well ID	V_{fi} (m^3)	c_f (10^{-5} psi^{-1})	$k_m k_{rg}$ (nD)	$\emptyset_m S_g$ (%)	A_{mf} (m^2)
A	41,705	6.47	23.1	5.7	507,423
B	41,917	2.94	18.0	4.1	1,152,651
C	50,597	1.31	19.4	5.9	505,957
D	47,562	10.00	16.7	4.9	543,147
E	40,042	1.00	-	-	-
F	39,810	1.00	19.9	4.9	1,086,921
G	43,725	1.32	-		-
H	46,383	6.17	25.1	4.8	1,021,690

V_{fi}: V_{fi} represents the initial volume of the effective fracture network at the onset of flowback. As discussed before, the effective fracture network includes all the connected fractures in flow communication with the wellbore, without differentiating their origin or morphology. It may also include fractures from adjacent wells when there is severe inter-well communication (Xu et al., 2016). For the target pad, Wells C and F have the maximum and minimum V_{fi} of 50,597 m^3 and 39,810 m^3, respectively.

c_f: c_f is defined as $\frac{1}{V_{fi}}\frac{dV_f}{dP_f}$, which is the normalized change of the effective fracture volume per unit change in fracture pressure. For the target pad, c_f is within the range of 10^{-5}-10^{-4} psi^{-1}. Well D has the highest c_f value of 10^{-4} psi^{-1}; while Wells E and F have the lowest c_f value of 10^{-5} psi^{-1}. The high c_f values (compared with matrix compressibility which is usually 10^{-7}-10^{-6} psi^{-1}) suggest that the effective fracture volume is very sensitive to the change in fracture pressure. This result is consistent with the results of Ezulike et al. (2016) who concluded that fracture closure accounts for 70 - 90 % of the total drive mechanisms during the first 100 hrs of flowback in tight sandstone and shale gas wells.

$k_m k_{rg}$ and $\emptyset_m S_g$: The estimated values of $k_m k_{rg}$ and $\emptyset_m S_g$ for the target pad are in the range if 18 - 25 nD and 4 - 6 %, respectively. In the proposed model, the shale matrix is assumed to be homogeneous and isotropic with constant values of $k_m k_{rg}$ and $\emptyset_m S_g$. In reality, however, the shale matrix is usually heterogeneous and anisotropic. Therefore, the estimated $k_m k_{rg}$ and $\emptyset_m S_g$ values actually represent the "average gas effective permeability" and "average effective gas porosity" of the shale matrix.

A_{mf}: Table 5.2 lists the estimated A_{mf} for six wells of the target pad. Since A_{mf} is estimated from the cumulative fluid influx from matrix to the fracture network (i.e. upward deviations in Figure 5.1), it represents an "effective fracture-matrix interface area" that allows gas flow from the matrix to the fracture system. In other words, the estimated A_{mf} does not include the interface area of the fractures that do not receive gas influx from matrix due to permeability jail effect, gravity segregation in fractures, and water trapping in matrix. Due to their ultra-low permeability and torturous pore structure, shales exhibit a unique behavior called permeability jail effect (Wattenbarger and Alkouh, 2013). Within a certain water saturation range, the flow conductances of both water and hydrocarbon phase are very low (relative permeability < 0.02). Bertocello et al. (2014) showed that when water saturation exceeds 40 %, the gas relative permeability in shales is negligible. Furthermore, experimental and simulation studies indicate that the fracturing water could accumulate at the bottom of long and vertical fractures due to gravity segregation (Parmar et al., 2012; Ghanbari and Dehghanpour, 2016). The accumulated bottom water, which can hardly be drained by gas, could also prevent gas flow from the matrix. For the target pad, Well B has the maximum A_{mf} of 1.15×10^6 m^2; while Well C has the minimum A_{mf} of 5.05×10^5 m^2. The values of A_{mf} will be discussed in detail in the next section.

5.6.2 Change of Effective Fracture Volume with Time

Table 5.3 lists the values of V_{fi}, c_f, A_{mf}, TIV and cumulative water volume recovered during flowback period (W_p^*) for the target pad. Based on these data, this section presents a volumetric comparative analysis to investigate the change of effective fracture volume with time during flowback period.

Figure 5.8 shows the casing pressure and BHP profiles during flowback for Well B of the target pad. The casing pressure is measured at the surface while the BHP is calculated from the casing pressure using Gray's correlation (Gray, 1978). Both casing and BHP profiles show a fast drop during EGP and remain relatively constant during LGP.

Table 5.3: The values of TIV, W_p^*, V_{fi}, V_{f_EGP}, V_{f_LGP}, HFE, $\Delta V_{f\_EGP}/V_{fi}$, and TLR for the target pad.

Well ID	TIV (m³)	W_p^* (m³)	V_{fi} (m³)	c_f (10^{-5} psi^{-1})	A_{mf} (m²)	V_{f_EGP} (m³)	V_{f_LGP} (m³)	V'_{f_LGP} (m³)	HFE (%)	$\Delta\frac{V_{f\_EGP}}{V_{fi}}$ (%)	TLR (%)
A	60,590	6,125	41,705	6.47	507,423	31,404	28,942	373	68.8	24.7	10.1
B	66,246	4,749	41,917	2.94	1,152,651	37,297	36,458	640	63.3	11.0	7.2
C	75,504	3,152	50,597	1.31	505,957	48,549	48,033	362	67.0	4.1	4.2
D	69,673	6,421	47,562	10.00	543,147	33,705	28,081	342	68.2	29.1	9.2
E	54,217	2,330	40,042	1.00	-	39,507	38,546	-	73.9	3.3	4.3
F	43,927	4,355	39,810	1.00	1,086,921	38,372	38,221	846	90.6	3.6	11.4
G	58,678	5,020	43,725	1.32	-	41,926	41,606	-	74.5	4.1	8.6
H	54,217	4,389	46,383	6.17	1,021,690	36,123	34,246	615	85.6	22.2	8.1

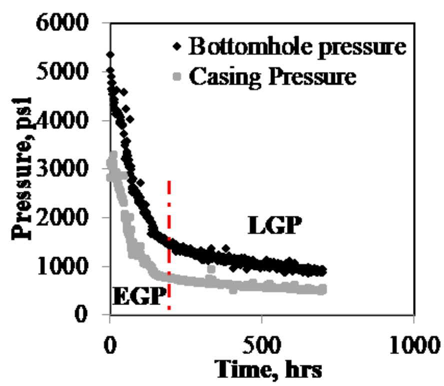

Figure 5.8: Casing pressure and BHP profiles for Well B of the target pad during flowback period. Both casing pressure and BHP profiles show quick pressure drop during EGP, followed by a plateau during LGP.

With the c_f value obtained from analysis of the EGP data, the effective fracture volume at the end of EGP (V_{f_EGP}) and at the end of LGP (V_{f_LGP}) can be calculated using Eqs. 5.18 and 5.19, respectively:

$$V_{f\_\text{EGP}} = V_{fi} - c_f \Delta P_{f\_\text{EGP}} \tag{5.18}$$

$$V_{f\_\mathrm{LGP}} = V_{fi} - c_f(\Delta P_{f\_\mathrm{EGP}} + \Delta P_{f\_\mathrm{LGP}}) \tag{5.19}$$

where $\Delta P_{f\_\mathrm{EGP}}$ and $\Delta P_{f\_\mathrm{EGP}}$ represents the bottomhole pressure drop during EGP and LGP phases, respectively. Table 5.3 lists the values of V_{f_EGP} and V_{f_LGP} for the target pad.

Previous studies have investigated the aperture (i.e. width) of fractures using various methods. Perkins and Kern (1961) found that the aperture of the hydraulic fractures depends on the proppant properties, pumping rates and volume, fracturing fluid viscosity, as well as rock properties. They investigated the aperture of hydraulic fractures in the fracture propagation process under different conditions. The results show that the aperture of hydraulic fractures is at millimetre to centimeter scale. Gale et al. (2014) compiled the aperture distribution of natural fractures from cores and outcrops in six shale plays. The results show that the size of fracture aperture ranges from 30 µm to 10 cm and most fractures in shales have aperture size of 30 µm to 1 mm. Zolfaghari et al. (2016) estimated the fracture aperture size distribution for the HR shales using flowback salt concentration profiles. Their results show that the majority of fractures have aperture sizes of 1 - 2 mm. Here, I assume that the effective fracture network, which includes both hydraulic and natural fractures, has an average aperture size of 1 mm, and roughly calculate the effective fracture volume for LGP (V'_{f_LGP}) using $V'_{f\_\mathrm{LGP}} = \frac{1}{2} w_f A_{mf}$. Table 5.3 lists the values V'_{f_LGP} for six wells of the target pad.

Figure 5.9 compares the values of TIV, W_p^*, V_{fi}, V_{f_EGP}, V_{f_LGP} and V'_{f_LGP} on a bar chart. For all wells, TIV > $V_{fi} > V_{f\_\mathrm{EGP}} \approx V_{f\_\mathrm{LGP}} > W_p^* > V'_{f\_\mathrm{LGP}}$. This observation is discussed below in detail.

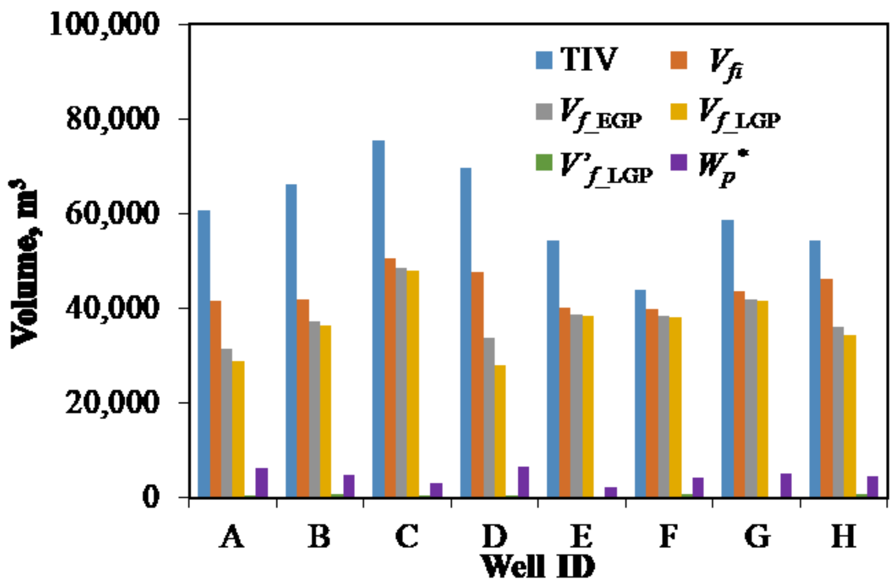

Figure 5.9: Comparative analysis between TIV, W_p^*, V_{fi}, V_{f_EGP}, V_{f_LGP}, and $V_{f}'{}_{\_LGP}$ for the target pad. The comparative analysis shows that TIV > V_{fi} > V_{f_EGP} ≈ V_{f_LGP} > W_p^* > $V_{f}'{}_{\_LGP}$.

V_{fi} versus TIV: Interestingly, the estimated V_{fi} is smaller than TIV. This is because part of the fracturing fluid might 1) leak off into the matrix due to forced and spontaneous imbibition during fracturing and shut-in periods (Holditch, 1979; Dehghanpour, 2012; 2013), and 2) be trapped in ineffective fractures poorly connected to the wellbore (Wattenbarger and Alkouh, 2013; Sharma and Manchanda, 2015). HFE, which is defined as V_{fi}/TIV, represents the effective fracture volume created per unit volume of fracturing water injected into the formation. HFE is a function of rock and fracturing fluid properties, fracture geometry, pumping rate, and pressure gradient between fracture and matrix (Penny et al., 1985; Yarushina et al., 2013). Table 5.3 lists the HFE values for the target pad. The average HFE for the target pad is 74 %, while Wells B and F have the minimum and the maximum HFE of 63.3 % and 90.6 %, respectively.

V_{f_EGP} versus V_{fi}: The estimated V_{f_EGP} is less than V_{fi}. This result indicates that the effective fracture volume may shrink due to the pressure depletion during EGP. The difference between V_{fi} and V_{f_EGP} may represent the change in the volume of the effective fracture network during EGP (ΔV_{f_EGP}), $\Delta V_{f\_EGP} = V_{fi} - V_{f\_EGP}$. $\Delta V_{f\_EGP}/V_{fi}$ represents the fraction of effective fracture loss during EGP. Table 5.3 shows that up to 30 % of the V_{fi} is lost during EGP. It should be noted that although

the effective fracture volume significantly reduces during EGP, most fractures remain partially open due to their rough surfaces and the existence of proppants. Compared with the shale matrix, these fractures still have a good permeability and conductivity and contribute to fluid flow.

V_{f_EGP} *versus* V_{f_LGP}: The values of V_{f_EGP} and V_{f_LGP}, both estimated from the compressibility relationship, are similar for the target pad. This result indicates that the effective fracture volume remains relatively constant during LGP. As evident from Figure 5.8, the pressure support from the matrix system significantly slows down the fracture pressure drop, and in turn, leads to insignificant fracture closure during LGP.

W_p^* *versus TIV*: For all eight wells, W_p^* is significantly less than TIV. TLR, which is defined as W_p^*/TIV, represents the relative amount of recoverable fracturing fluids. Table 5.3 shows that for the target pad, TLR is only ~10 %. Wells F and C have the maximum and the minimum TLR values of 11.9 % and 4.2 %, respectively. The results indicate that a significant amount of the fracturing water remains in the formation. The fate of the remaining fracturing fluid and its potential effects on hydrocarbon production have been discussed in previous studies (Engelder et al., 2014; Sharma and Manchanda, 2015; Ghanbari and Dehghanpour, 2016).

V'_{f_LGP} *versus* V_{f_LGP}: The values of V'_{f_LGP} is relatively low and do not match the calculated V_{f_LGP} values. V'_{f_LGP} is calculated from the estimated A_{mf} and an assumed average w_f of 1 mm. The estimated A_{mf} represents the "effective fracture-matrix surface area" that receives gas influx from the surrounding matrix. Therefore, the unexpectedly low values of V'_{f_LGP} suggests that the effective fracture-matrix interface area is relatively low. In other words, although the fracturing operation creates a large fracture network, only a small portion of this network contributes to fluid flow during LGP. A significant part of the fracture network may not contribute to matrix-fracture flow communication, mainly due to the permeability damage caused by extensive water leak off. According to Motealleh and Bryant (2009), in unconventional rocks, a small increase in water saturation could result in a significant reduction in gas relative permeability. The leaked-off water could form pendular rings (i.e. liquid bridges) at the grain contacts, reducing the area open to gas flow, and consequently reducing the effective permeability for gas phase. It should be noted that the leaked-off water, although increases the water saturation in the matrix, is immobile due to high capillary pressure of the shale matrix, as discussed in Section 5.3.1. This phenomenon is more pronounced in low-porosity rocks (porosity less than 20 %) since the pendular rings at pore throats might completely block the flow paths and reduce the connectivity of the gas phase. The difference between V'_{f_LGP} and V_{f_LGP} values indicates a significance of ineffective fractures during late-time production, which may be responsible for the low water recovery as well as the low gas production observed in many shale gas wells.

5.7 Limitations

The limitations of the proposed open-tank model are presented below.

First, the effective fracture network is assumed as a "two-phase tank" of arbitrary geometry with uniform properties (i.e. pressure, saturation, and compressibility). Although this assumption has a great advantage in describing irregular fracture geometries, it simplifies the fracture closure behavior. In reality, the effective fracture network contains hydraulic, secondary, and natural fractures. The geomechanical properties of different fractures might lead to different c_f values. For example, compared to the hydraulic fractures, most natural fractures close more easily at increased effective pressure and should have higher values of c_f due to lack of proppants. Future studies should develop a more accurate method for estimating average c_f value for the effective fracture system.

Second, the proposed model assumes negligible water influx from the matrix (i.e. $W_pB_w = 0$). In principle, according to Eq. 5.6, the upward deviations in Figure 5.1 represent cumulative fluid influx from the matrix (i.e. $W_pB_w+G_{in}B_g$). Neglecting water influx effect from the matrix could lead to an overestimation of $G_{in}B_g$ which in turn results in an overestimation of A_{mf}.

Third, the outputs of the open-tank model have uncertainties, which come from 1) the uncertainties associated with the input parameters, and 2) the history matching process. First, the accurate values of c_f, S_{gi}, k_mk_{rg}, and $\emptyset_m S_g$ in the proposed model are unknown in field applications. In this study, a search space is selected for each unknown based on extensive literature review. Although the reasonable ranges are used, the uncertainties in the model inputs may result in uncertainties in the model outputs. Such uncertainties can be reduced with accurate reservoir and fracture properties from geological surveys as well as experimental studies (such as core analysis). Besides, the analysis procedure is essentially a history matching process with several unknown parameters varying simultaneously to get the optimal solution set. Different objective functions, different search spaces and different initial guesses could lead to different model outputs. Advanced reservoir and fracture estimation techniques could help to restrict the model outputs and reduce the outputs uncertainties. For example, Xu et al. (2016b) suggested using microseismic interpretation results as benchmarks to screen out reservoir and fracture estimates from flowback data analysis.

In addition, there are uncertainties/limitations associated with the numerical model. Although we assign four fractures with different apertures and lengths to represent an irregular fracture system, the numerical model may not fully capture fluid flow drive mechanisms within a more complex fracture network (such as orthogonal or fractal fracture patterns). Besides, the numerical model does not investigate the effects different operational parameters (such as TIV, shut-in time, injection rate) on V_{fi}.

Finally, it is worth noting that the EGP phase may not always be observed during flowback period. The duration of EGP depends on many parameters including reservoir types, initial reservoir conditions, shut-in time, and flowback rate. Besides, this early-time flow regime might be masked by wellbore storage effect or operational strategies (such as frequent shut-in and choke size changes). In such cases, estimation of V_{fi} using the EGP data may be challenging.

5.8 Summary

This chapter extended the previous closed-tank material balance model presented in Chapter 3 to an open-tank one, validated the open-tank model against a 2D numerical case, proposed a workflow for two-phase (gas + water) flowback data analysis in gas shales, applied the workflow on an eight-well pad completed in the Horn River Basin, and conducted a volumetric comparative analysis to investigate the change of effective fracture volume with time during flowback period.

The analysis results show that up to 75 % of the injected water during hydraulic fracturing process are effective in creating the effective fracture volume. During Early Gas Production phase, the fracture pressure quickly drops from the initial reservoir pressure of around 5,000 psi to production pressure of around 1,000 psi within several hundred hours. As a result, up to 30 % of the induced fracture volume may be closed. During Late Gas Production phase, the matrix system provides sufficient pressure support which keeps the fracture pressure relatively constant and reduces the rate of fracture closure. However, volumetric comparative analysis indicates that a significant part of the effective fracture network may not contribute to long-time gas production due to poor flow communication between the fracture and the matrix systems. Possible reasons include water blockage, permeability jail effect, and gravity segregation.

In summary, the results of this chapter highlight the loss of effective fracture volume during early-time flowback period. The results also suggest that although shales usually have low leak-off rate due to their low permeability, the lost water might cause severe water blockage and significant reduction in well productivity.

Nomenclature

A_{mf}	=	fracture-matrix interface area, m^2
B_g	=	gas formation volume factor, std. volume/res. volume
B_{gi}	=	gas formation volume factor at initial condition, std. volume/res. volume
B_w	=	water formation volume factor, std. volume/res. volume
c_f	=	fracture compressibility, 1/psi
c_t	=	total compressibility, 1/psi
c_w	=	water compressibility, 1/psi
E	=	expansion coefficient
F	=	underground withdrawal, res. m^3
G_{fi}	=	volume of gas initially in the fractures, std. m^3

G_{in}	=	volume of gas influx, std. m^3
G_p	=	cumulative gas production, std. m^3
k_m	=	matrix permeability, D
k_{rg}	=	gas relative permeability
L	=	fracture spacing, cm
m	=	pseudo-pressure function, atm^2/cp
m_D	=	dimensionless gas pseudo-pressure
P_f	=	average fracture pressure, psi
P_i	=	initial reservoir pressure, psi
P_m	=	matrix pressure, psi
P_{sc}	=	standard pressure, psi
q_{in}	=	rate of gas influx at reservoir conditions, res. m^3/d
q_{in}^{SC}	=	rate of gas influx at standard conditions, std. m^3/d
s	=	Laplace operator
S_{gi}	=	initial gas saturation in the effective fracture network
S_w	=	water saturation in the matrix
t	=	time, s
t_a	=	pseudo-time function, atm*s/cp
t_D	=	dimensionless time
T	=	reservoir temperature, K
T_{sc}	=	standard temperature, K
V_{fi}	=	initial effective fracture volume, m^3

W_{in}	=	cumulative water influx, std. m^3
W_p	=	cumulative water production, std. m^3
W_p^*	=	cumulative water production during flowback period, std. m^3
x_D	=	dimensionless distance
Z	=	gas compressibility factor
ϕ_m	=	matrix porosity
μ_g	=	gas viscosity, cp
Δ	=	change
∇	=	gradient

Chapter 6: Estimating the Compressibility of Hydraulic Fractures

This chapter is a modified version of a manuscript that is currently under review in *Engineering Geology*. The manuscript was modified by changing the voice from plural first person (we) to singular first person (I).

6.1 Introduction

Fracture compressibility (c_f) is a term that is analogous to the well-known "formation compressibility" in reservoir engineering. It describes the change in fracture pore volume resulting from the change in effective pressure (P_e). Terzaghi (1923) is first define P_e as the difference between the confining pressure (P_c) and the pore pressure (P_p). This definition is widely accepted in the field of soil and rock mechanics (Jaeger et al., 2007). In cemented rocks, σ_c is partially taken by the rock skeleton. Biot (1941) defined σ_e as $\sigma_e = \sigma_c - \beta P_p$, where β is called Biot's coefficient that describes the volumetric changes in the pore spaces due to the rock grain deformation. The value of β ranges between 0 (for solid rock without pores) and 1 (for extremely porous rocks), and can be either a static or dynamic value (Nermoen et al., 2013; He et al., 2016; Yuan et al., 2017; Saberi and Jenson, 2018).

c_f is a key parameter for modeling fracture closure and estimating fracture volume loss in fractured reservoirs. Aguilera (1999) developed a series of type curves to estimate c_f of natural fractures. In his work, the c_f values are within the range of 10^{-3} - 10^{-6} psi^{-1}, depending on 1) the value of P_e applied on the fractures, 2) the percentage of secondary mineralization within the fractures, and 3) the relative volume of fractures and vugs. c_f also plays a significant role in production forecast and estimation of ultimate hydrocarbon recovery. Aguilera (2006; 2008) showed that neglecting c_f (and the change in c_f during production) leads to overestimation of gas in place and recovery factor in saturated naturally-fractured reservoirs.

Recent studies show that fracture closure is the primary drive mechanism during early-time flowback period in unconventional reservoirs stimulated by hydraulic fracturing operations (Ezulike et al., 2016; Xu et al., 2017). Flowback period is between the injection phase when the fracturing fluid pressure could reach up to 8,000 psi and the production phase when the BHP is about 1,000-2,000 psi. The excessive pressure drop during flowback period is one key reason for severe fracture volume loss. Xu et al. (2017) analyzed the flowback rate and pressure data from eight HR shale gas wells and found that up to 30 % of the induced fracture volume is lost during early-time water flowback. The fracture closure behavior is often described using c_f in material balance analysis. Xu et al. (2015; 2016a) applied two-phase material balance analysis on flowback data from eight shale gas wells to estimate initial effective fracture volume. They considered c_f as an unknown parameter determined by history matching of the flowback data. The results show that the estimated c_f could be 10 times higher than water compressibility and have similar magnitude as gas compressibility. Monte-Carlo simulation conducted by Ezulike et al. (2016) showed that the estimated effective fracture volume is very sensitive to c_f. Fu et al. (2017) estimated c_f for seven wells completed in the Woodford Formation using the Diagnostic Fracture Injection Tests (DFIT) data and Aguilera's type curves. However, Aguilera's type curves are originally designed for c_f estimation of natural fractures, not induced hydraulic fractures. Unlike natural fractures, the induced hydraulic fractures usually contain high-strength proppants that may significantly change the fracture closure behavior. Besides, the method proposed by Fu et al. (2017) requires fracture porosity as an input parameter, which is usually unknown in field cases.

Reliable estimation of c_f is essential for calculating induced fracture volume, evaluating the change in fracture volume, and forecasting long-time hydrocarbon recovery for hydraulically-fractured reservoirs. However, estimating c_f in unconventional reservoirs is challenging due to complex fracture geometry and complex mechanisms for fracture closure. During hydraulic fracturing operations, the fracturing fluids (usually slick water) are pumped with proppants (solid, high-strength particles such as sands) to create fractures for fluid flow. In theory, the created hydraulic fractures should be perpendicular to the minimum in-situ stress direction (Economides and Nolte, 1989). However, recent techniques such as microseismic imaging show that the created fracture network usually has complex geometry due to the complex stress conditions underground and pre-existing natural fractures interacting with hydraulic fractures (Weng et al., 2011; Wu et al., 2012; Xu et al., 2016b). Ann induced hydraulic fracture may penetrate, dilate, or activate a pre-existing natural fracture, depending on the aperture and orientation of the natural fracture and the injection rate of the fracturing fluids (Maxwell, 2011; Cheng et al., 2015). Besides, fracture closure is a complex process, partly due to the non-uniform distribution of proppants inside the fracture network. For instance, most hydraulic fractures remain partially open even at high P_e values due to the presence of high-strength proppants. However, the induced fracture network also includes pre-existing natural fractures and hydraulic fractures without proppants. The closure behavior of these unppfoped fractures is primarily controlled by the asperities on the fracture surfaces (Bandis et al., 1983; Duan et al., 2000; Wang and Sharma, 2017). In addition, slickwater fracturing also introduce partially propped fractures in shales. Experimental studies showed that proppants settle and form a proppant back at the bottom of a vertical fracture (Kern et al., 1959; Sahai et al., 2014; Alotaibi and Miskimins, 2015). Analytical and numerical models have been developed to investigate the closure behavior of such partially propped fractures. Wang and Sharmar (2018) show that the unpropped section will close first at low P_e; while the propped section remain open even at high values of P_e. Simulation studies by Liu (Liu, 2017) show that as a partially propped fracture closes, the unpropped and propped sections are connected by an arch.

This chapter proposes an analytical model for estimating c_f and understanding fracture closure in hydraulically-fractured unconventional reservoirs. The induced fractures are divided into two groups: unpropped and propped fractures. c_f of unpropped fractures is estimated from the results of fracture conductivity measurements; while c_f of propped fractures is derived from the Hertzian contact theory (Hertz, 1882). For unpropped fractures, the proposed model is applied on 32 samples from the HR and the Barnett shales, and the results are compared with those from Aguilera's type curves (Aguilera, 1999). For propped fractures, sensitivity analyses are conducted to investigate the effects of proppant parameters on estimated c_f. Finally, c_f values of five synthetic fracture networks with different volume percentage of unpropped and propped fractures are calculated and compared to understand the roles of unpropped and propped fractures during the fracture closure process.

The rest of this chapter include five sections: Section 6.2 derives the mathematical model for estimating c_f in hydraulically-fractured reservoirs; Section 6.3 demonstrates the applications of the proposed model; Section 6.4 discusses the results; Section 6.5 lists the limitations of the proposed model; and Section 6.6 summarizes this chapter.

6.2 Fracture Compressibility Model

Zimmerman et al. (1986) defined four compressibilities for a porous rock, each of which relates the change in either pore volume (V_p) or bulk volume (V_b) with respect to the change in either P_p or P_c. The pore compressibility (c_{pp}) is defined as the change in V_p of rock per unit change in P_p:

$$c_{pp} = \frac{1}{V_p}\left(\frac{dV_p}{dP_p}\right)_{P_c} \tag{6.1}$$

In petroleum engineering, c_{pp} is often called "formation compressibility" and is widely used in reservoir analysis. (Zimmerman, 1991; Ahmed, 2010).

Similar to formation compressibility, c_f can be defined as the change in V_p of a fracture per unit change in P_e:

$$c_f = -\frac{1}{V_f}\frac{dV_f}{dP_e} \tag{6.2}$$

where V_f represents the V_p of the fracture. Treating the fracture as an elastic material, P_e is the difference between the P_c and the fluid pressure in the fractures: $P_e = P_c - P_f$.

V_f can be geometrically defined by

$$V_f = \frac{1}{2}A_f w_f \phi_f \tag{6.3}$$

where A_f, w_f, and ϕ_f are the fracture-matrix interface area, fracture aperture and fracture porosity, respectively.

Substituting Eq. 6.3 into Eq. 6.2, one get:

$$c_f = -\frac{1}{\frac{1}{2}A_f w_f \phi_f}\frac{d\left(\frac{1}{2}A_f w_f \phi_f\right)}{dP_e} = -\frac{1}{A_f w_f \phi_f}\frac{d\left(A_f w_f \phi_f\right)}{dP_e} \tag{6.4}$$

Assuming that A_f does not change with P_e and applying the chain rule gives

$$c_f = -\frac{1}{A_f w_f \phi_f}\frac{d(A_f w_f \phi_f)}{dP_e} = -\frac{1}{\phi_f}\frac{d\phi_f}{dP_e} - \frac{1}{w_f}\frac{dw_f}{dP_e} \tag{6.5}$$

Eq. 6.5 shows that c_f consists of two parts. $-\frac{1}{\phi_f}\frac{d\phi_f}{dP_e}$ and $-\frac{1}{w_f}\frac{dw_f}{dP_e}$ describe the rate of change in fracture porosity and fracture aperture due to the change in P_e, respectively. Sections 6.2.1 and 6.2.2 will introduce models for estimating c_f of unpropped and propped fractures, respectively.

6.2.1 Unpropped Fractures

The closure of an unpropped fracture is controlled by the asperities (i.e. roughness) on the fracture surfaces (Bandis et al., 1983; Duan et al., 2000). As P_e increases, w_f decreases, increasing the contact area of asperities on the opposing fracture surfaces. The increase in contact area induces additional contact stresses, which will affect the fracture closure behavior as P_e increases further (Wang and Sharma, 2017). However, in field practice, direct measurement of c_f is challenging since it is impossible to obtain accurate profiles of asperities on fracture faces. In this study, c_f is estimated indirectly by using the measured data of fracture conductivity.

Seidel et al. (1992) derived the relationship between c_f and fracture permeability of coal cleats using matchstick geometry:

$$\frac{k_f}{k_{f0}} = e^{-3\overline{c_f}(P-P_0)} \tag{6.6}$$

where P and P_0 are the pressure of interest and the reference pressure, respectively. k_f and k_{f0} are the fracture permeability at P and P_0, respectively. $\overline{c_f}$ is the average fracture compressibility within the pressure range of P_0 to P. When $P - P_0$ is infinitely small, $\overline{c_f}$ represents the c_f at P. The relationship (Eq. 6.6) is proven to work for fractures in shales by matching the measured fracture permeability data of samples from five shale reservoirs (Chen et al., 2015; 2016).

Multiplying both sides of Eq. 6.6 by fracture aperture ratio ($\frac{w_f}{w_{f0}}$) gives

$$\frac{C_f}{C_{f0}} = \frac{k_f}{k_{f0}}\frac{w_f}{w_{f0}} = e^{-3\overline{c_f}(P-P_0)} \times \frac{w_f}{w_{f0}} \tag{6.7}$$

where C_f and C_{f0} are the fracture conductivity measured by laboratory tests at P and P_0, respectively. w_f and w_{f0} are the fracture aperture at P and P_0, respectively.

Taking the logarithm of both sides of Eq. 6.7 gives

$$\ln\left(\frac{C_f}{C_{f0}}\right) = -3\overline{c_f}(P - P_0) + \ln(\frac{w_f}{w_{f0}}) \tag{6.8}$$

Eq. 6.8 predicts a linear relationship to between $\ln\left(\frac{C_f}{C_{f0}}\right)$ and (P - P_0). It indicates that the slope and intercept of a plot of $\ln\left(\frac{C_f}{C_{f0}}\right)$ vs. (P - P_0) are $3\overline{c_f}$ and $\ln(\frac{w_f}{w_{f0}})$, respectively. In this study, Eq. 6.8 is used to estimate c_f of unpropped fractures.

6.2.2 Propped Fractures

Figure 6.1 schematically illustrates the closure process of a propped fracture. Grey circles represent the proppants inside the fracture. Black rectangles and triangles represent some random asperities on facture surfaces. Figure 6.1a shows the schematic of the fracture when $P_e = 0$ (i.e. $P_c = P_f$). Proppants of different sizes are loosely placed inside the fracture. Figure 6.1b shows the schematic of the fracture when $P_e > 0$ (i.e. $P_c < P_f$). As P_e increases, w_f decreases. Consequently, the proppant density inside the fracture increases due to the reduced fracture pore volume. Furthermore, some proppants near the fracture surfaces may embed into the rock. As the fracture is assumed to be an elastic material, proppant crushing during the fracture closure process is neglected.

To mathematically describe the fracture closure behavior, the propped fracture in Figure 6.1 is simplified using a "sandwich" model shown in Figure 6.2. Previous studies show that the closure of a propped fracture is mainly controlled by the proppants (Li et al., 2015). Therefore, the random asperities on the fracture surfaces are neglected and the fracture surfaces are modeled using two smooth planes. All proppants are assumed to be identical spheres of radius r. The proppants inside the fractures are simplified into three parts: one layer of proppant pack in the middle of the fracture, and two layers of indenters, each of which lies between the proppant pack and the fracture surface. The proppant pack is assumed to be a porous elastic material with

Young's modulus, initial porosity, and initial thickness of E_{pp}, ϕ_i, and h_i, respectively. The indenter layers are made up of semi-spherical, elastic proppants that are uniformly placed on the top and bottom of the proppant pack. Figures 6.2a and 6.2b show the schematic of the simplified fracture when $P_e = 0$ and $P_e > 0$, respectively. At $P_e = 0$, $w_{fi} = h_i + 2r$. As P_e increases, the fracture closes with its aperture reduces from w_{fi} to w_f. Consequently, the proppant pack is compacted. h_i and ϕ_i decrease to h and ϕ, respectively. Furthermore, the indenter layers embed into the rock matrix with depth of δ.

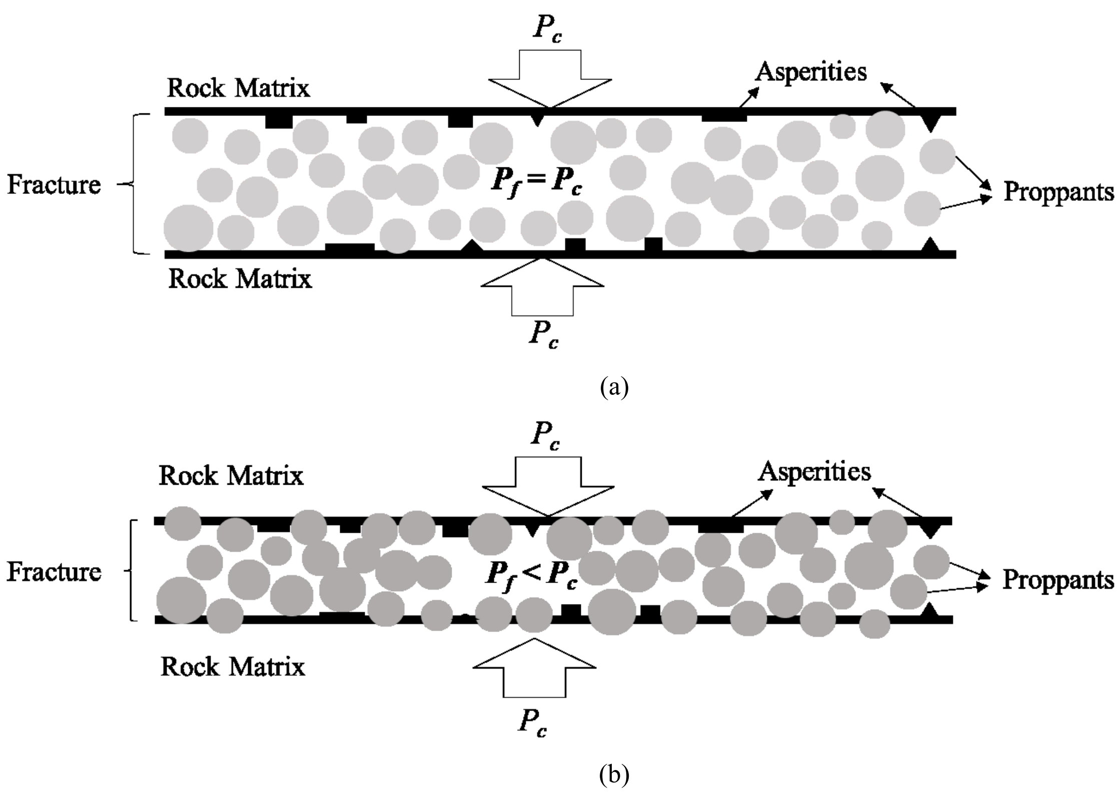

Figure 6.1: Closure process of a propped fracture. Grey circles represent proppants of different sizes. Black rectangles and triangles represent the random asperities on the fracture surfaces. (a) The fracture is subject to zero P_e (i.e. $P_f = P_c$). (b) The schematic of the fracture when $P_e > 0$ (i.e. $P_f < P_c$). As P_e increases, the fracture aperture reduces. The density of proppants increases due to reduced fracture pore volume. Some proppants near the fracture surfaces embed into the rock matrix. Not to scale.

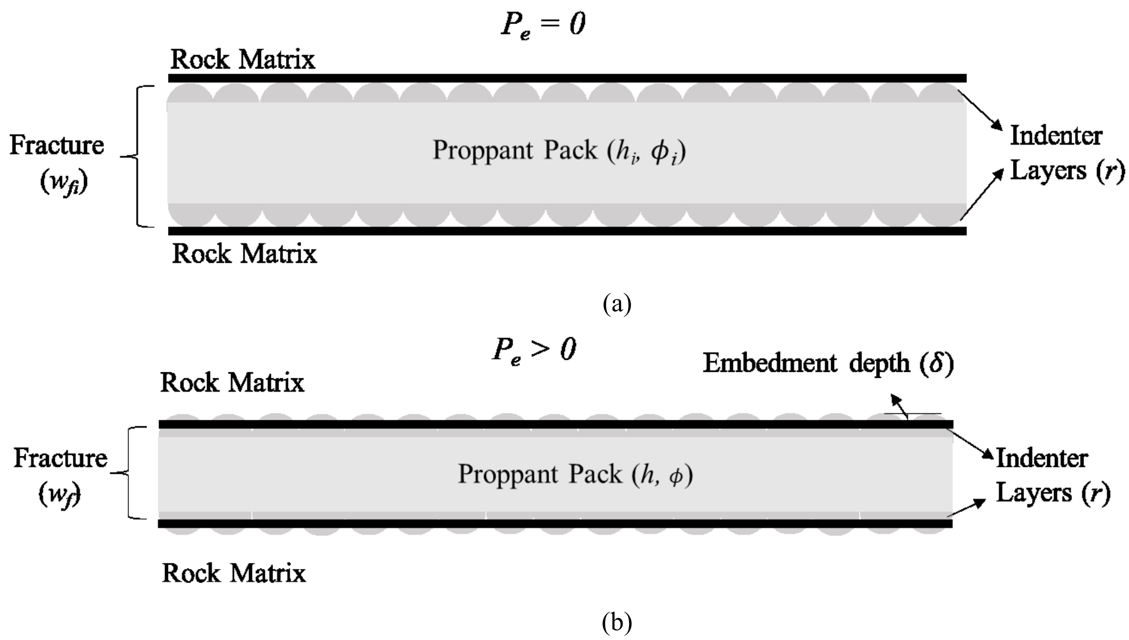

Figure 6.2: Closure process of a simplified propped fracture. The fracture surfaces are modeled as two smooth planes. The proppants inside the fractures are modeled using one layer of proppant pack and two layers of indenters. (a) The fracture is subject to zero P_e. (b) The fracture is at $P_e > 0$. As P_e increases, the proppant pack is compacted with reduced porosity (ϕ) and reduced height (h). The proppant layers are uniformly embed into the rock matrix with depth of δ. Not to scale.

6.2.2.1 Fracture Aperture Change

Based on Figure 6.2b,

$$w_f = h + 2r - 2\delta \tag{6.9}$$

Assuming that proppant embedment into the rock matrix is an elastic deformation process, δ can be modeled using the Hertzian contact theory (Hertz, 1882).

$$\delta = r(\frac{3P_e}{E^*})^{\frac{2}{3}} \tag{6.10}$$

$$\frac{1}{E^*} = \frac{1-v_s^2}{E_s} + \frac{1-v_r^2}{E_r} \tag{6.11}$$

where E_s and E_r are the Young's modulus of the indenters and the rock matrix, respectively. v_s and v_r are the Poisson's ratio of the indenters and the rock matrix, respectively. E^* is an equivalent Young's modulus that describes the mechanical interaction between the indenter and the rock matrix. Detailed derivation is presented in Appendix F.

h can be modeled by

$$h = h_i - \frac{P_e}{E_{pp}} h_i \tag{6.12}$$

Substituting Eqs. 6.10 and 6.12 into Eq. 6.9 gives

$$w_f = h_i - \frac{P_e}{E_{pp}} h_i + 2r - 2r(\frac{3P_e}{E^*})^{\frac{2}{3}} \tag{6.13}$$

Thus, $-\frac{1}{w_f}\frac{dw_f}{dP_e}$ is given by

$$-\frac{1}{w_f}\frac{dw_f}{dP_e} = \frac{1}{w_f}\frac{h_i}{E_{pp}} + \frac{4r}{w_f E^*}\left(\frac{3P_e}{E^*}\right)^{-\frac{1}{3}} \tag{6.14}$$

Eq. 6.14 describes the rate of change in fracture aperture with respect to the change in P_e.

6.2.2.2 Fracture Porosity Change

Gangi (1978) proposed a model for porosity change in a rock. In this study, Gangi's model is used to describe the porosity change in the proppant pack:

$$\phi(P_e) = \frac{\phi_i[1-C_0(\frac{P_e}{E_0})^{\frac{2}{3}}]^3}{1-\phi_i+\phi_i[1-C_0(\frac{P_e}{E_0})^{\frac{2}{3}}]^3} \tag{6.15}$$

$$E_0 = \frac{E_s}{3(1-v_s^2)}, \quad C_0 = 1 + \frac{r}{r_p} \tag{6.16}$$

where r/r_p is the ratio between the grain size and the pore radius, the value of which depends on the packing format of the proppant pack. E_0 is an equivalent Young's modulus that describes the mechanical interaction of two spherical proppants in contact inside the proppant pack. Assuming that the proppants are quartz sands with E_s = 72 GPa and v_s = 0.2, the calculated E_0 turns out to be 40 GPa.

The values of P_e during flowback are usually in the magnitude of several thousands psi, which is way lower than the calculated E_0 (i.e. $P_e << E_0$). Therefore, Eq. 6.15 simplifies to

$$\phi(P_e) = \phi_i[1 - C_0(\frac{P_e}{E_0})^{\frac{2}{3}}]^3 \tag{6.17}$$

Assuming $\phi_f \approx \phi$ (i.e. fracture porosity can be approximated using proppant pack porosity), $-\frac{1}{\phi_f}\frac{d\phi_f}{dP_e}$ is given by

$$-\frac{1}{\phi_f}\frac{d\phi_f}{dP_e} = -\frac{1}{\phi}\frac{d\phi}{dP_e} = \frac{2C_0}{P_e}\frac{\left(\frac{P_e}{E_0}\right)^{\frac{2}{3}}}{1-C_0\left(\frac{P_e}{E_0}\right)^{\frac{2}{3}}} \tag{6.18}$$

Eq. 6.18 describes the rate of change in fracture porosity with respect to the change in P_e.

6.2.2.3 Final Equation of Fracture Compressibility

Substituting Eqs. 6.14 and 6.18 into Eq. 6.5 gives the final equation for estimating c_f.

$$c_f = \frac{1}{w_f}\frac{h_i}{E_{pp}} + \frac{4r}{w_f E^*}(\frac{3P_e}{E^*})^{-\frac{1}{3}} + \frac{2C_0}{P_e}\frac{\left(\frac{P_e}{E_0}\right)^{\frac{2}{3}}}{1-C_0\left(\frac{P_e}{E_0}\right)^{\frac{2}{3}}} \tag{6.19}$$

Eq. 6.19 shows that c_f of a propped fracture is a function of P_e, w_f, r, C_0, and Young's moduli and Poisson's ratios of rock, proppants, and proppant pack (i.e. E_r, v_r, E_s, v_s, and E_{pp}). The effects of w_f, r and C_0 on estimated c_f will be investigated and discussed in Section 6.3.

It should be noted that there is an underlying assumption in the aforementioned derivation - The fracture is filled with multiple layers of proppants. In other words, despite for the two indenters layers, there are still sufficient proppants that form a proppant pack (i.e. $w_f > 2r$ and $h_i > 0$). If the fracture is filled with only one layer of proppants with no proppant pack (i.e. $w_f = 2r$ and $h_i = 0$), Eq. 6.19 becomes

$$c_f = \frac{2}{E^*}(\frac{3P_e}{E^*})^{-\frac{1}{3}} \tag{6.20}$$

Eq. 6.20 suggests that c_f of fractures with single layer of proppants is independent of w_f, r, E_{pp}, and C_0.

6.2.3 Complex Fracture Network

In field practice, the induced fracture network after hydraulic fracturing has both unpropped and propped fractures. Here, a workflow is proposed for estimating c_f of a complex fracture network.

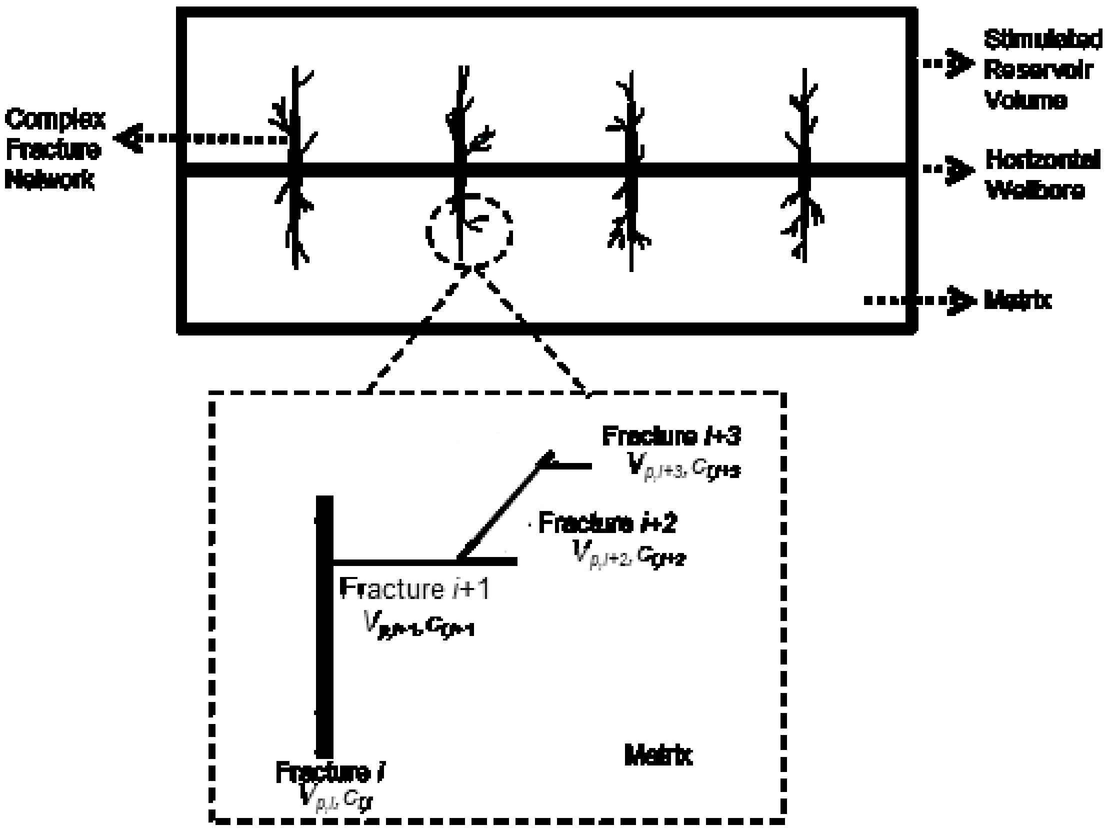

Figure 6.3: Schematic of a fracture network in a hydraulically-fractured reservoir. The complex fracture network is simplified using a series of slit-like fracture segments in the inset plot. The i^{th} fracture segment has its pore volume and compressibility of $V_{p,i}$ and $c_{f,i}$, respectively. Not to scale. (Modified from Zolfaghari et al., 2015).

Figure 6.3 depicts a complex fracture network, which is simplified using a series of slit-like fracture segments (as shown in the inset plot). The i^{th} fracture segment has pore volume and compressibility of $V_{f,i}$ and $c_{f,i}$, respectively. Total pore volume of the fracture network is the sum of the pore volume of all fracture segments: $V_f = \sum V_{f,i}$. Due to the high conductivity of fractures, the pressure gradient inside the fracture network can be assumed negligible. Therefore, the complex fracture network is treated as a "tank" with uniform P_f distribution during flowback period, as done similarly in previous studies (Patzek et al., 2013; Edwards et al., 2015; Ezulike et al., 2016; Fu et al., 2017; Xu et al., 2015; 2016a; 2017).

Thus, c_f of a fracture network can be expressed as

$$c_f = -\frac{1}{V_f}\frac{dV_f}{d\overline{P_e}} = -\frac{1}{V_f}\frac{d\sum V_{f,i}}{d(\overline{P_c - P_f})} \tag{6.21}$$

where the fracture network is assumed to subject to an average effective pressure of $\overline{P_e}$.

Due to the complexity of fracture geometry and the anisotropy of in-situ stress field, P_c for different fracture segments might be different. For example, the induced hydraulic fractures are usually perpendicular to the minimum horizontal stress direction (Economides and Nolte, 1989). Therefore, P_c for hydraulic fractures is the minimum in-situ stress (i.e. $P_c = \sigma_{min}$). However, most natural fractures are formed in response to the paleostresses (i.e. ancient stresses) that are unrelated to the in-situ stresses (Rezaee, 2015). Therefore, in such cases, P_c for natural fractures may be different from that for hydraulic fractures (i.e. $P_c \neq \sigma_{min}$).

It is challenging to estimate c_f when P_c is unknown. Here, an "average confining pressure" ($\overline{P_c}$) is introduced to solve for Eq. 6.21. As discussed before, P_c for each fracture segment depends on the in-situ stress conditions and the fracture orientation, both of which do not change during fracture closure process. Therefore, it is plausible to assume that P_c for each fracture segment remain constant during the fracture closure process. Consequently, $\overline{P_c}$ for the fracture network also remains constant.

Thus, Eq. 6.21 simplifies to

$$c_f = -\frac{1}{V_f}\frac{d\sum V_{f,i}}{d(\overline{P_c} - P_f)} = -\sum\frac{1}{V_f}\frac{dV_{f,i}}{d(\overline{P_c} - P_f)} = \sum\frac{V_{f,i}}{V_f}\left(-\frac{1}{V_{f,i}}\frac{dV_{f,i}}{dP_f}\right) = \sum c_{f,i}\frac{V_{f,i}}{V_f} \tag{6.22}$$

Eq. 6.22 shows that c_f of a fracture network is the volumetric average of c_f for all fracture segments. When estimating c_f using Eq. 6.22, $c_{f,i}$, $V_{f,i}$ and V_f should be updated at each pressure step since they are functions of pressure. Figure 6.4 presents the workflow to estimate c_f of a fracture network at P_e.

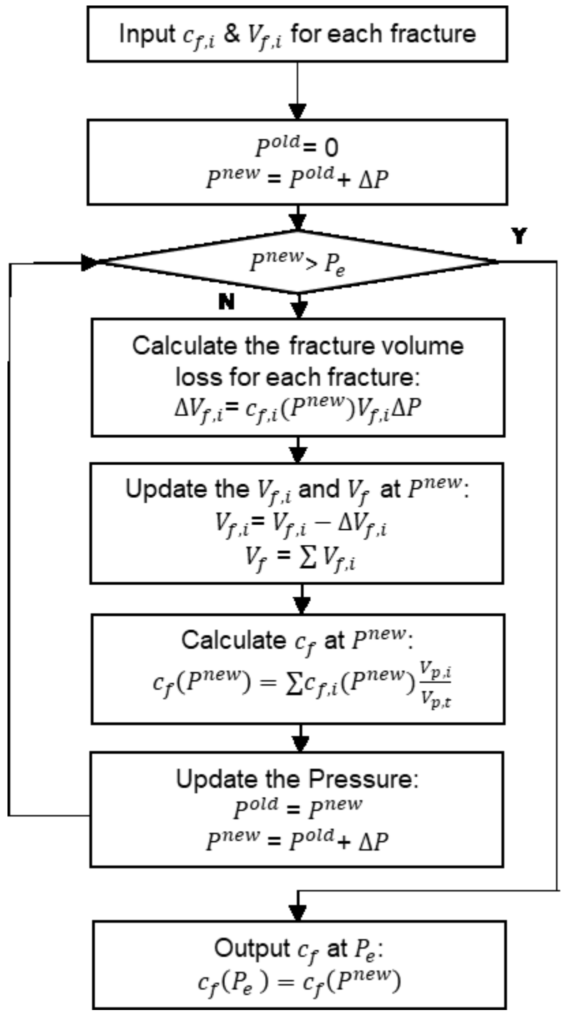

Figure 6.4: Workflow to estimate c_f of a fracture network.

6.3 Applications

In this section, Eq. 6.8 is first used to estimate the c_f values of unpropped fractures using the fracture conductivity measurements of 34 samples from two shale reservoirs. Then, sensitivity analyses are conducted to investigate the effects of different proppant parameters (i.e. proppant size, number of proppant layers, and proppant packing format) on estimated c_f for the propped fractures.

6.3.1 Unpropped Fractures

Terra Tek conducted fracture conductivity measurements for 12 unpropped fractures in the HR shale samples, as presented in Table 6.1. Zhange et al. (2014) conducted fracture conductivity tests for 22 unpropped fractures in the Barnett shale samples, and their results are presented in Table 6.2. The HR shale reservoir is located in British Columbia, Canada; while the Barnett shale reservoir is located in Texas, United States. Appendix G provide a brief description about the materials, experiment setup, and experiment procedures. It should be noted that for some fractures, the conductivity values at high pressure were not measured due to complete closure of the fractures and/or failure of the samples. In this section, Eq. 6.8 is applied on the 34 samples to calculate the $\overline{c_f}$ values from the measured fracture conductivity data.

Table 6.1: Results of fracture conductivity tests for 12 unpropped fractures in the HR shale samples (Experiments conducted by Terra Tek)

	Fracture Conductivity (md-ft)						
Pressure (psi) / Sample ID	500	1,000	2,000	4,000	6,000	8,000	10,000
A	120.441	74.386	40.126	10.275	5.407	2.000	0.846
B	34.077	4.761	0.164	0.008	0.002	0.002	0.001
C	333.815	189.608	156.148	78.074	51.048	30.867	6.554
D	127.979	65.818	29.534	15.357	7.889	3.599	1.526
E	60.336	17.489	2.277	0.129	0.226	0.013	0.010
F	4.006	2.462	1.057	0.253	0.104	0.032	0.009
G	32.271	21.985	9.003	4.154	1.599	0.669	0.289
H	14.628	0.806	0.074	0.008	0.001	0.000	-
I	2.312	0.297	0.084	0.018	0.005	0.000	-
J	25.794	19.600	14.097	9.100	4.934	3.255	2.245
K	8.771	4.127	1.396	0.326	0.134	0.073	-
L	525.680	210.272	79.348	22.732	7.378	3.223	0.930

Table 6.2: Results of fracture conductivity tests for 22 unpropped fractures in the Barnett shale samples (from Zhang et al., 2014)

	Fracture Conductivity (md-ft)				
Pressure (psi) / Sample ID	500	1,000	2,000	3,000	4,000
A	4.00	1.80	1.10	0.40	0.00
B	32.90	14.80	5.80	3.80	2.40
C	34.70	18.40	4.90	1.10	0.30
D	60.90	20.00	3.80	0.80	0.20
E	26.70	13.80	4.50	2.00	1.00
F	246.94	90.90	26.30	4.20	0.70
G	609.70	61.80	14.20	2.00	0.50
H	375.50	179.10	17.00	3.90	0.80
I	777.40	201.40	19.90	7.20	2.50
J	68.70	37.60	10.20	0.60	-
K	8.40	2.10	0.50	0.30	-
L	13.70	5.30	2.20	1.20	-
M	16.40	7.70	3.00	1.20	-
N	18.10	4.30	1.00	0.20	-
O	25.70	13.20	7.20	1.50	-
P	32.80	7.90	2.00	0.20	-
Q	43.80	10.20	1.80	0.30	-
R	854.30	131.00	15.80	2.80	0.30
S	389.30	102.00	9.00	1.10	0.20
T	232.20	66.20	10.50	2.00	0.40
U	43.80	10.20	1.80	0.30	0.10
V	678.80	273.10	57.50	11.00	2.60

Figure 6.5 shows the application of Eq. 6.8 on the 34 shale samples. Figures 6.5a presents the plot of $\ln\left(\frac{C_f}{C_{f0}}\right)$ vs. (P - P_0) for the 12 HR samples. We choose the minimum pressure in Table 6.1 as the reference pressure, P_0 = 500 psi. A general linear relationship between $\ln\left(\frac{C_f}{C_{f0}}\right)$ and (P - P_0) is observed in most of the samples (i.e. all samples except for Samples B and E), as predicted by Eq. 6.8. However, Samples B and E do not follow the straight-line relationship (marked as outliers in Figure 6.5a). The values of $\ln\left(\frac{C_f}{C_{f0}}\right)$ drops fast with (P - P_0) when $0 < (P - P_0) < 3{,}000$

psi, but gradually flattens when (P - P_0) is higher than 3,000 psi. This result suggest that the proposed model (Eq. 6.8) is applicable to ten of the HR samples analyzed within the pressure range of 500 to 10,000 psi. For Samples B and E, the proposed model fails to give a representative $\overline{c_f}$ estimation. Figure 6.5b presents the plot of $\ln\left(\frac{c_f}{c_{f0}}\right)$ vs. (P - P_0) for the 22 samples from the Barnett shales. Similar to the HR shales, we select the minimum pressure in Table 6.2 as the reference pressure, P_0 = 500 psi. with the assumption of P_0 = 500 psi. For all 22 samples analyzed, the values of $\ln\left(\frac{c_f}{c_{f0}}\right)$ decreases linearly with increasing (P - P_0), as predicted by Eq. 6.8. This result suggest that the proposed model (Eq. 6.8) is applicable to all Barnett samples within the pressure range of 500 to 3,000 psi.

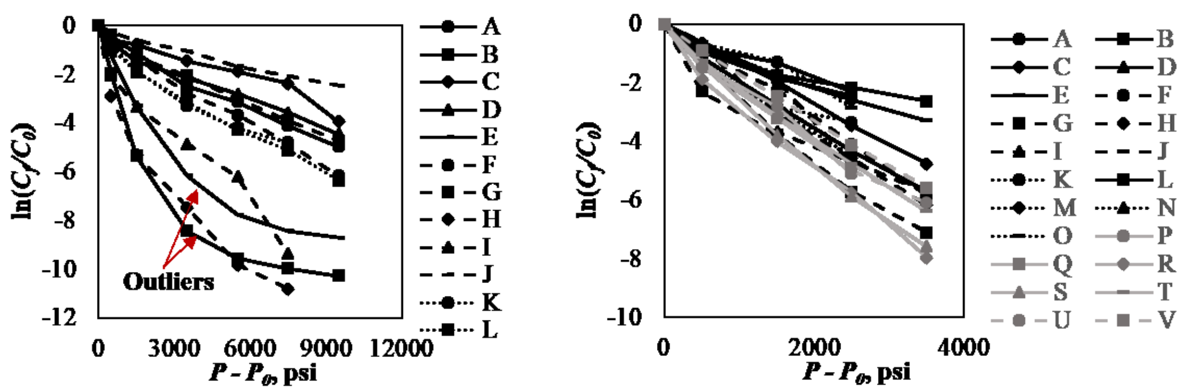

(a) (b)

Figure 6.5: Plot of ln (C_f/C_0) vs. (P - P_0) for (a) 12 samples from the HRB, and (b) 22 samples from the Barnett shales. The P_0 for both cases are set to be 500 psi.

Table 6.3: Calculated $\overline{c_f}$ values for 34 Unpropped Fractures in the HR and the Barnett Shale Samples

HR Shale Samples		Barnett Shale Samples			
Sample ID	Calculated $\overline{c_f}$ (10^{-4} psi^{-1})	Sample ID	Calculated $\overline{c_f}$ (10^{-4} psi^{-1})	Sample ID	Calculated $\overline{c_f}$ (10^{-4} psi^{-1})
A	1.70	A	2.85	M	3.40
B	-	B	2.38	N	5.77
C	1.18	C	4.57	O	3.59
D	1.43	D	5.39	P	6.48
E	-	E	3.12	Q	6.45
F	2.09	F	5.48	R	7.24
G	1.61	G	6.40	S	7.24
H	4.42	H	5.97	T	5.97
I	3.60	I	5.39	U	5.74
J	0.85	J	6.20	V	5.30
K	2.09	K	4.31		
L	2.08	L	3.11		

The $\overline{c_f}$ values presented are a "representative c_f" applicable for the pressure range analyzed. The pressure ranges are 500 - 9,500 psi for the HR samples, and 500 - 3,500 psi for the Barnett samples, respectively.

Overall, Figure 6.5 suggests that the proposed model is applicable for most of the shale samples analyzed in this study. According to Eq. 6.8, $\overline{c_f}$ is related to the slope of ln$\left(\frac{C_f}{C_{fo}}\right)$ vs. (P - P_0) plots. Therefore, I construct a best-fit line for each sample and calculate the representative values of $\overline{c_f}$ using the line slope. Samples B and E from the HR shales are excluded in the calculation since they do not follow a linear relationship in Figure 6.5. Table 6.3 summarizes the calculated $\overline{c_f}$ values for the 34 samples from the two shale reservoirs.

6.3.2 Propped Fractures

Eq. 6.19 presents the equation for estimating c_f of a propped fracture. However, the proposed model has several assumptions such as 1) fracture closure is an elastic deformation process and 2) the proppants in the fractures are identical. Besides, there are limited data source of accurate c_f measurements form laboratory or field tests. Most of the experiments focuses on measuring the fracture aperture and conductivity loss during fracture closure process (Fredd et al. 2001; Alramahi and Sundberg 2012; Huo et al. 2014; Zhang et al. 2014; Jansen et al. 2015; Perez Pena et al., 2016). Therefore, it is challenging to validate the proposed model against available experiment results. In this section, a series of sensitivity analyses is conducted to investigate the controlling parameters of c_f for propped fractures. The effects of proppant size, number of proppant layers, and proppant packing format are investigated.

First, an ideal fracture is constructed as the *Base Case*. Table 6.4 lists the properties of the rock, the proppants, and the proppant pack for *Base Case*. w_f is assumed to be 2 mm based on literature review (Gale et al., 2014; Wu et al., 2017; Edwards and Celia, 2018; Liu et al., 2018). E_r and v_r are obtained from the Unconfined Compressive Strength (UCS) tests conducted on the HR shale samples. 40/70 mesh quartz sands are assumed as proppants in our analysis, since they are because 40/70 mesh sands are used in the hydraulic fracturing operations of the HR formations. Therefore, the proppants are assumed as quartz crystals with have Young's modulus of 72 GPa and Poisson's ratio of 0.2. It should be noted that since Eq. 6.18 assumes identical spherical proppants, the average radius of the 40/70 mesh proppants (i.e. r = 316 µm) is used in the calculation. E_{pp} and C_0 are assumed to be 20 GPa and 2, respectively.

Table 6.4: Properties of the rock, the proppant and the proppant pack for the *Base Case*.

Parameter	Value	Unit
Young's Modulus of Rock Matrix (E_r)	28	GPa
Poisson's Ratio of Rock Matrix (v_r)	0.15	-
Young's Modulus of Proppants (E_s)	72	GPa
Poisson's Ratio of Proppants (v_s)	0.2	-
Proppant Size	40/70	Mesh
Average Proppant Radius (r)	316	µm
Proppant Packing Format (C_0)	2	mm
Young's Modulus of Proppant Pack (E_{pp})	20	GPa
Fracture Aperture (w_f)	2	mm

To investigate the effect of proppant size on c_f, four types of quartz sands commonly used in hydraulic fracturing operations are assumed as proppants in the sensitivity analysis: 16/30 mesh sands with r = 890 µm, 20/40 mesh sands with r = 630 µm, 40/70 mesh sands with r = 316 µm (*Base Case*), and 70/140 mesh sands with r = 139 µm. Other parameters for the rock, the proppant and the proppant pack are the same as those for the *Base Case*. Figure 6.6a shows that for all cases, the calculated c_f decreases non-linearly when P_e increases from 100 to 5,000 psi. The c_f drops sharply at low values of P_e (i.e. P_e < 1,000 psi), and shows a gradual decline when P_e > 1,000 psi.

Figure 6.6a also shows that the calculated c_f decreases with decreasing proppant size. This is because decreasing r leads to less δ, resulting in lower values of $-\frac{1}{w_f}\frac{dw_f}{dP_e}$ and c_f, as shown in Eqs. 6.10 and 6.19,

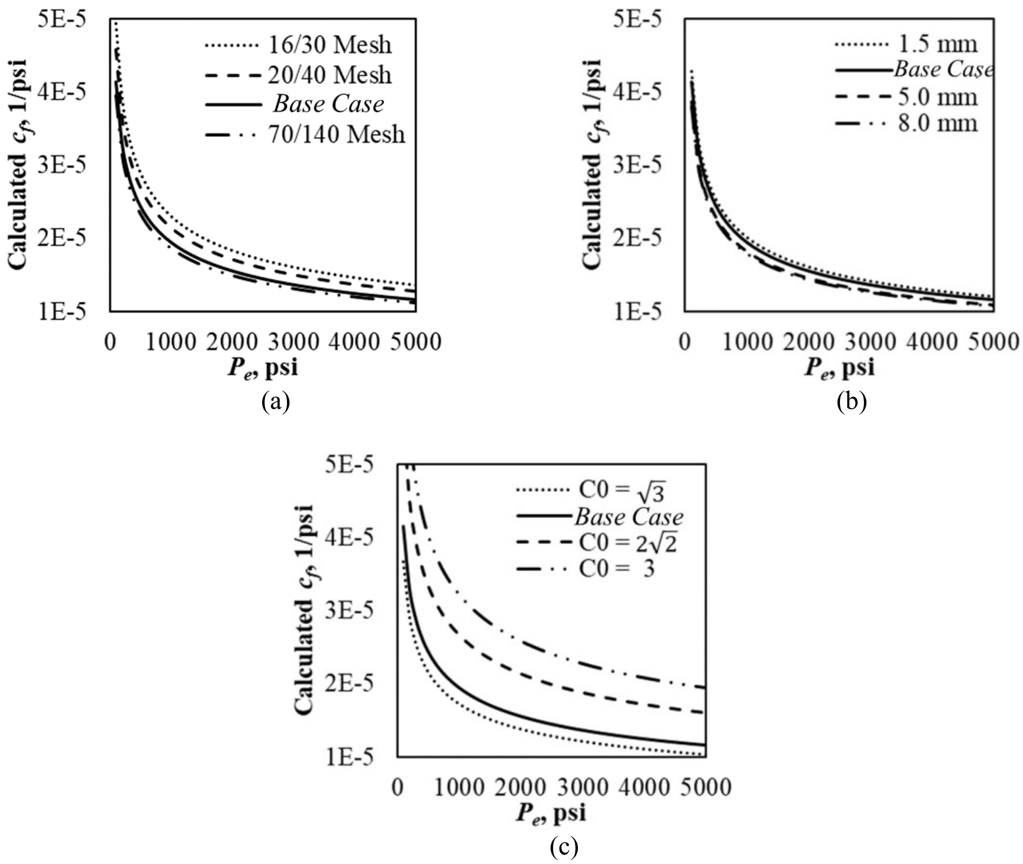

Figure 6.6: Sensitivity analysis to investigate the effects of different proppant parameters on estimate c_f for a propped fracture. (a) Effect of proppant size on the calculated c_f. c_f decreases with smaller proppants; (b) Effect of the number of proppant layers on the calculated c_f. The number of proppant layers plays a minor role on c_f estimation; (c) Effect of proppant packing format on the calculated c_f. c_f increases with denser packing format.

Second, the effect of number of proppant layers on c_f estimation is investigated. According to Eq. 6.19, the number proppant layers is related to w_f, since the fractures with a wider w_f hold a thicker proppant pack that contain more layers of proppants. In this study, four fractures with different values of w_f are constructed, and their c_f values are calculated and compared: w_f = 1.5 mm, w_f = 2 mm (*Base Case*), w_f = 5 mm, and w_f = 8 mm. Other parameters for the rock, the proppant and the proppant pack are the same as those for the *Base Case*. Figure 6.6b shows that increasing the number of proppant layers (i.e. increasing w_f) decreases the calculated c_f. This is because increasing w_f leads to lower values of $-\frac{1}{w_f}\frac{dw_f}{dP_{eff}}$ and c_f, as shown in Eqs. 6.14 and 6.19.

Finally, to investigate the effect of proppant packing format on the calculated c_f, four fractures with different C_0 values are calculated and compared: $C_0 = \sqrt{3}$, $C_0 = 2$ (*Base Case*), $C_0 = 2\sqrt{2}$, and $C_0 = 3$. Other parameters for the rock, the proppant and the proppant pack are the same as those for the *Base Case*. Figure 6.6c shows that fractures with denser packing format has higher c_f values. According to Eqs. 6.16 and 6.19, denser packing format indicates higher values of r/r_p and C_0, and consequently result in higher values of $-\frac{1}{\phi_f}\frac{d\phi_f}{dP_e}$ and c_f.

The sensitivity analysis suggest that the porosity change inside the fractures dominant the calculated c_f values. Eq. 6.5 shows that c_f consists of two parts: $-\frac{1}{\phi_f}\frac{d\phi_f}{dP_e}$ and $-\frac{1}{w_f}\frac{dw_f}{dP_{eff}}$. Variations in the proppant size and the number of proppant layers is related to the change in fracture aperture; while variation in proppant packing format is related to the change in fracture porosity. Comparison among Figures 6.6a, 6.6b, and 6.6c suggests that the calculated c_f is primarily controlled by fracture porosity change, while the fracture aperture change plays a secondary role.

The sensitivity analysis also suggests the feasibility for simplifying the proposed model. Eq. 6.19 shows that the c_f depends on four parameters, w_f, h_i, $\underline{E_{pp}}$, and C_0. However, the accurate values of these parameters are usually unknown in field practices. This largely restricts the application of the proposed model, and could introduce uncertainties in the model outputs. Figure 6.6b suggests that the number of proppant layers plays an insignificant role in c_f estimation. As discussed before, the number of proppant layers is linked with height of the proppant pack in the proposed model. Therefore, I neglect the effect of the proppant pack compaction (i.e. $h = h_i$) and revisit the proposed model in Section 6.2.2. Eq. 6.23 shows the simplified model for estimating c_f of propped fractures. Detailed derivation is presented in Appendix H.

$$c_f = \frac{4r}{w_{fi} - 2r(\frac{3P_e}{E^*})^{\frac{2}{3}}} (\frac{3P_e}{E^{*2}})^{-\frac{1}{3}} + \frac{2C_0}{P_e} \frac{\left(\frac{P_e}{E_0}\right)^{\frac{2}{3}}}{1 - C_0\left(\frac{P_e}{E_0}\right)^{\frac{2}{3}}} \tag{6.23}$$

Compared to Eq. 6.19, Eq. 6.23 has only two unknown parameters (i.e. w_{fi} and C_0) and is more applicable for field practices. Further simplification of Eq. 6.23 for practical use of the proposed model will be the focus of our future study.

6.4 Discussions

In this section, Eq. 6.8 is first used to calculate the step-wise c_f for the unpropped fractures in Section 6.3.1. The results are compared with Aguilera's type curves for natural fractures (Aguilera, 1999). Besides, the c_f values of five fracture networks with different pore volume percentages of propped and propped fractures are calculated and compared to investigate the roles of unpropped and propped fractures during the fracture closure process.

6.4.1 Calculate Step-Wise Compressilbity of Unpropped Fractures

Table 6.5: Calculated step-wise c_f of the unpropped fractures for 12 HR shale samples.

	Calculated c_f (10^{-4} psi^{-1})					
Pressure (psi) / Sample ID	500-1,000	1,000-2,000	2,000-4,000	4,000-6,000	6,000-8,000	8,000-10,000
A	3.21	2.06	2.27	1.07	1.66	1.43
B	13.12	11.22	5.14	1.90	0.68	0.48
C	3.73	0.65	1.16	0.71	0.84	2.58
D	4.43	2.67	1.09	1.11	1.31	1.43
E	8.26	6.80	4.79	2.69	1.10	0.48
F	3.24	2.82	2.38	1.49	1.95	2.20
G	2.56	2.98	1.29	1.59	1.45	1.40
H	19.34	7.98	3.62	3.92	1.63	-
I	13.67	4.23	2.55	2.25	5.26	-
J	1.83	1.10	0.73	1.02	0.69	0.62
K	5.03	3.61	2.42	1.48	1.00	-
L	6.11	3.25	2.08	1.88	1.38	2.07
Average	7.04	4.11	2.46	1.76	1.58	1.41

Table 6.6: Calculated step-wise c_f of the unpropped fractures for the 22 Barnett shale samples.

Sample ID \ Pressure (psi)	Calculated c_f (10^{-4} psi^{-1}) 500 -1,000	1,000 - 2,000	2,000 - 3,000	3,000 - 4,000
A	5.32	1.64	3.37	-
B	5.33	3.12	1.41	1.53
C	4.23	4.41	4.98	4.33
D	7.42	5.54	5.19	4.62
E	4.40	3.74	2.70	2.31
F	6.66	4.13	6.11	5.97
G	15.26	4.90	6.53	4.62
H	4.94	7.85	4.91	5.28
I	9.00	7.72	3.39	3.53
J	4.02	4.35	9.44	-
K	9.24	4.78	1.70	-
L	6.33	2.93	2.02	-
M	5.04	3.14	3.05	-
N	9.58	4.86	5.36	-
O	4.44	2.02	5.23	-
P	9.49	4.58	7.68	-
Q	9.71	5.78	5.97	-
R	12.50	7.05	5.77	7.45
S	8.93	8.09	7.01	5.68
T	8.37	6.14	5.53	5.36
U	9.71	5.78	5.97	3.66
V	6.07	5.19	5.51	4.81
Average	7.55	4.90	4.95	4.55

Section 6.3.1 gives an estimation of $\overline{c_f}$ for 32 of the 34 fractures analyzed. However, Samples B and E from the HR shales can not be represented by a single value of $\overline{c_f}$ within the given pressure range (i.e. 500 to 10,000 psi). This problem can be solved by discretizing the given pressure range into different pressure steps and estimate step-wise c_f values using Eq. 6.8. The step-wise c_f explicitly shows that c_f is a function of pressure values, and is more accurate in fracture closure estimation. Here, I discretize the pressure range and calculate the step-wise c_f for all 34 samples. For the 12 HR samples, the given pressure range (i.e. 500 psi to 10,000 psi) is divided into six pressure steps; while for the Barnet samples, the given pressure range (i.e. 500 psi to 4,000 psi) is divided into four pressure steps. The step-wise c_f values are estimated using Eq. 6.8. Tables 6.5 and 6.6 summarize the calculated step-wise c_f of the HR and the Barnett shale samples, respectively. The average c_f value at each pressure step for formation is also included.

6.4.2 Comparing the calculated step-wise compressibility of the unpropped fractures with Aguilera's Type Curves

Aguilera (1999) proposed a series of type curves (Figure 6.7) to estimate c_f values of natural fractures based on 1) correlations between P_c and fracture permeability (Jones, 1982), 2) Tkhostov's discussion on secondary porosity (Tkhostov, 1970), and 3) his own observation on secondary mineralization. Figure 6.7 shows the type curves for c_f as a function of P_e, the percentage of secondary mineralization in the fractures (indicated by "*Miner*"), and the percentage of fracture porosity to total porosity (indicated by "*Ratio*").

Figure 6.7 compares the average step-wise c_f values calculated from the proposed model (Tables 6.4 and 6.5) with those from Aguilera's type curves. The dotted and the dashed lines in represent average step-wise c_f values of the unpropped fractures from the HR and the Barnett shale samples, respectively.

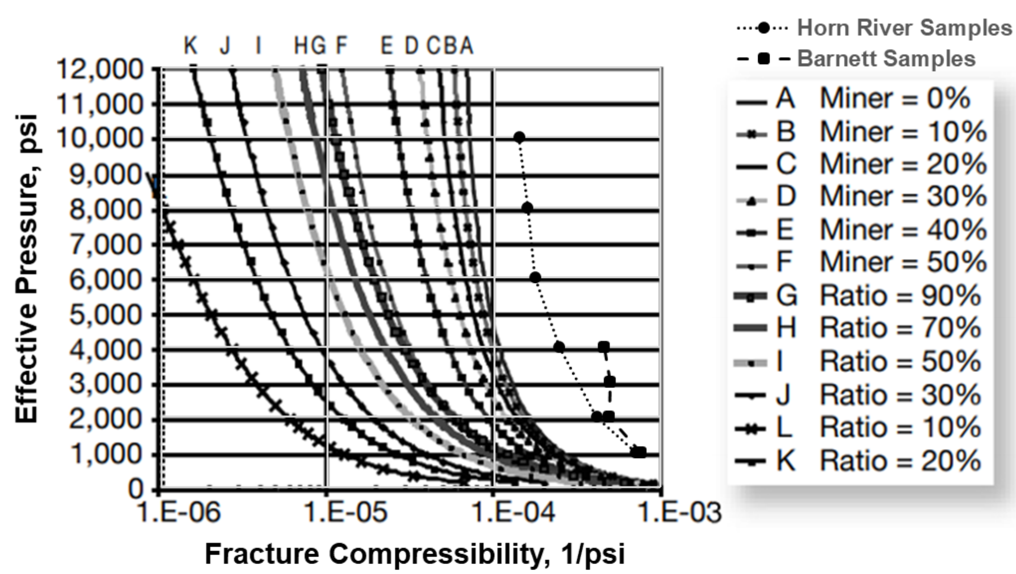

Figure 6.7: Comparison between the c_f values calculated from the proposed model with the ones from Aguilera's type curves (Aguilera, 2006). The dotted and dashed lines represent the average step-wise c_f values of the unpropped fractures from the HR samples and the Barnett shale samples, respectively. The c_f values calculated from the proposed model are higher than those from Aguilera's type curves.

Figure 6.7 shows that c_f calculated using the proposed model follows similar trends as Aguilera's type curves. The c_f decreases non-linearly with increasing P_e. The c_f values decreases sharply at low values of P_e. The rate of decline decreases as at high values of P_e. However, the calculated c_f values for both shale reservoirs are higher compared with Aguilera's results. The difference might be due to the different rocks used in the analysis. Aguilera's work is based on experimental studies of carbonates; while the proposed model focuses on shale samples. Shales have lower values of uniaxial compressive strength compared to sandstones and carbonates, especially when they are rich in clay contents and organic matters (Hoek and Brown, 1997; Chang et al., 2006). Besides, many shales show ductile behavior due to the high clay minerals and organic material (Abouelresh and Slatt, 2012). Therefore, the shales are less likely to sustain an open fracture with increasing P_e. (Gross, 1995; Gale et al., 2014).

6.4.3 Roles of Unpropped and Propped Fractures during Fracture Closure Process

A real hydraulic fracture network consists of both propped and unpropped fractures. Here, I calculate and discuss the c_f values of five irregular fracture networks, which have the same total pore volume, but with different ratios for propped and unpropped fractures. The objective is to investigate the roles of unpropped and propped fractures during the fracture closure process.

Five arbitrary fracture networks with both propped and unpropped fractures are constructed. All fracture networks have identical initial fracture pore volume of 50,000 m^3. However, the initial pore volume for the propped fractures for the five networks are set to be 5,000 m^3, 12,500 m^3; 25,000 m^3, 37,500 m^3 and 45,000 m^3, respectively. That is to say, the volume percentage of the propped fractures to the total fracture network are 10 %, 25 % 50 %, 75 %, and 90 %, respectively. The calculated c_f of the HR samples (Figure 6.7, HR shales) and that of the *Base Case* (Figure 6.6, *Base Case*) are used as c_f of the unpropped and the propped fractures in the synthetic fracture networks, respectively.

Figure 6.8 compares the c_f curves of five fracture networks calculated using the algorithm described in Figure 6.4, with those of unpropped and propped fractures. c_f of the unpropped fractures is two orders of magnitude higher than that of the propped fractures. The values of c_f are higher for fracture network with more unpropped fractures. Furthermore, c_f of the fracture network follows similar trend as that of unpropped fractures at low P_e, but approaches that of propped fractures at high P_e. This result suggests that during fluid depletion period, the unpropped fractures play a dominant role at early times when P_e is relatively low, but the propped fractures play a dominant role at late times when P_e becomes relatively high. Furthermore, Figure 6.8 suggests that a small portion of unpropped fractures could significantly increase c_f of the fracture network, especially at low P_e. This results implies that one would expect more severe fracture closure during early-time flowback in reservoirs with well-developed natural fractures (which are usually unpropped). The severe fracture closure in such reservoirs might lead to excessive fracture volume loss, resulting in low hydrocarbon recovery.

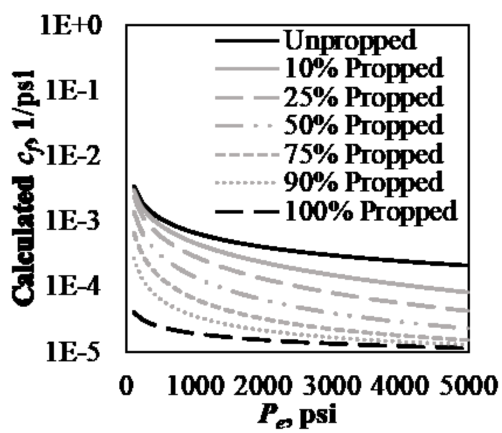

Figure 6.8: Calculated c_f vs. P_e for five synthetic fracture networks, together with those of unpropped and propped fractures. c_f of the fracture networks follow similar trend as that of the unpropped fractures at low P_e, but approaches that of the propped fractures at high P_e.

6.5 Limitations

The limitations of the proposed model for estimating c_f of a hydraulically-fractured reservoir is summarized as follows:

First, the proposed model assumes the fracture closure as an elastic process. Plastic deformation and rock/proppant failure at high P_e (such as stress-hardening effect and proppant crushing) are ngelected in the proposed model. These assumptions might not hold true under in-situ conditions. Proppant embedment tests show that in soft formations such as clay-rich shales, the indentation of proppants into the rock matrix could not be fully recovered after unloading the samples (Alramahi and Sundberg, 2012). According to Eqs. 6.11 and 6.19, neglecting rock plastic deformation results in overestimation of E_s and E^*, and consequently in underestimation of c_f. On the other hand, experimental studies show the occurrence of brittle failure, such as proppant crushing and formation of tensile fractures at the rock-proppant and the proppant-proppant contact, during the fracture closure process (Cooke, 1977; Reinicke, 2009; Ingraham et al., 2015). In such cases, the created rock and proppant chips may fill the pore space inside the proppant pack, and the proposed model may overestimate c_f due to underestimation in E_{pp}.

Second, all proppants are assumed as identical spheres in the proposed model. Although this assumption reduces the complexity of the final analytical solution, it may not fully capture the properties of the proppants in field practice. The injected proppants during hydraulic fracturing operations usually have different sizes and shapes that may affect the mechanical properties of the proppant pack. When packing granular materials with different sizes, small grains tend to occupy the pore space between the large grains (Taiebat et al., 2017). In such cases, the proposed model may overestimate c_f due to underestimation in E_{pp}. In addition, the sphericity of the proppants might also affect the values of c_f. Previous studies show that proppants with lower sphericity and roundness yield lower porosity of the proppant pack (Liang et al., 2016). This limitation can be addressed by incorporating proppant size distribution in the proposed model.

Third, the proposed model assumes two indenter layers of r. Therefore, the model cannot capture the fracture closure behavior when the indenter layers fully embed into the rock matrix. In reality, multiple layers of proppants may embed into the rock matrix at high values of P_e. A more general and representative model for capturing proppant embedment into the rock matrix could be one focus of future study.

Finally, proppant movement and rearrangement are neglected in the proposed model. During flowback process, the proppants may be carried by the fracturing fluids and hydrocarbon flowing towards the wellbore, leading to concentration reduction and non-uniform distribution of the proppants inside the fractures. This may further enhance fracture closure due to lack of proppant support, and in turn increase the value of c_f.

6.6 Summary

Previous studies show that fracture closure is a key drive mechanism for production in hydraulically-fractured unconventional reservoirs, especially during early-time flowback period. Fracture compressibility, which describes the pore volume change inside the fractures due to the change in effective pressure, is often used to describe fracture closure behavior and to quantify fracture volume loss in hydraulically-fractured reservoirs. This chapter proposes a mathematical model to estimate fracture compressibility for hydraulically-fractured wells. The induced fracture network is divided into unpropped and propped fractures. The compressibility of unpropped fractures is calculated from the fracture conductivity measurements; while that of propped fractures is calculated based on Hertzian contact theory. A workflow is provided to estimate the compressibility of a complex fracture network. Sensitivity analyses are conducted to investigate different proppant parameters on fracture compressibility.

The results from this chapter show that the fracture compressibility consists two parts: the rate of porosity change and the rate of fracture aperture change due to the change in effective pressure. The rate of porosity change, which is controlled by proppant packing format, dominates the fracture compressibility values; while the rate of aperture change plays a secondary role. The results highlight the importance of proppants in reducing fracture compressibility values and resisting fracture closure. The compressibility of an unpropped fracture is about two orders of magnitude higher than that of a propped fracture. For a fracture network with both propped and unpropped fractures, the unpropped fractures controls the closure behavior at low effective pressure; while the propped fractures dominate the fracture closure at high effective pressure. The results also suggest that the severe fracture volume loss during early-time flowback is due to the closure of unpropped fractures.

Nomenclature

A_f	=	fracture surface area, m^2
c_f	=	fracture compressibility, 1/psi
$c_{f,i}$	=	compressibility of the i^{th} fracture, 1/psi

$\overline{c_f}$ = average fracture compressibility, 1/psi

c_{pp} = pore compressibility, 1/psi

C_f = fracture conductivity, md-ft

C_{f0} = fracture conductivity at reference pressure, md-ft

E_{pp} = Young's modulus of the proppant pack, psi

E_r = Young's modulus of the rock, psi

E_s = Young's modulus of the proppant, psi

h = height of the proppant pack, m

h_i = initial height of the proppant pack, m

k_f = fracture permeability, md

k_{f0} = fracture permeability at reference pressure, md

P = pressure, psi

P_0 = reference pressure, psi

P_c = confining pressure, psi

P_e = effective pressure, psi

$\overline{P_e}$ = average effective pressure, psi

P_f = fracture pressure, psi

P_p = pore pressure, psi

r = proppant radius, m

r_p = pore radius, m

v_r = Poisson's ratio of the rock, psi

v_s = Poisson's ratio of the proppant, psi

V_b	=	bulk volume, m^3
V_f	=	pore volume of fracture, m^3
$V_{f,i}$	=	pore volume of the i^{th} fracture, m^3
V_p	=	pore volume, m^3
w_f	=	average fracture aperture, m
w_{f0}	=	average fracture aperture at reference pressure, m
ϕ	=	porosity of the proppant pack
ϕ_f	=	fracture porosity
ϕ_i	=	initial porosity of the proppant pack
σ_{min}	=	minimum in-situ stress, psi
δ	=	indentation depth into rock matrix, m
Δ	=	change

Chapter 7: Conclusions and Recommendations

This study presents qualitative and quantitative analyses of gas and water rate and pressure data during flowback period from eight multi-fractured horizontal wells completed in the Horn River Basin. The primary goal of this study is to provide a protocol for fracture characterization by using flowback data in hydraulically-fractured gas shales wells. Compared to microseismic monitoring and fiber optics, flowback data analysis is an easy, fast, and inexpensive tool for fracture characterization. In this dissertation, various methods, including diagnostic analysis, numerical simulation, material balance analysis, and comparative analysis to capture the fluid flow signatures, identifies flow regimes, understand the fluid flow physics and drive mechanisms, estimate key fracture parameters, and investigate the change of fracture volume during flowback period. Furthermore, a mathematical model is developed to estimate fracture compressibility of hydraulically-fractured unconventional reservoirs. This chapter summarizes the key conclusions of this research study and presents recommendations for future work.

7.1 Conclusions

The key conclusions from this study can be summarized as follows:

Chapter 2

1. The Horn River wells analyzed in this study show immediate two-phase (gas + water) production once they are opened for flowback. The immediate gas production comes from the free gas saturated in the fracture network before flowback, which is due to counter-current imbibition during the extended shut-in period.

2. The Horn River wells analyzed in this study shows a unique V-shape Gas Water Ratio. Based on this signature, two flow regimes are identified: Early Gas Production with a decreasing Gas Water Ratio trend, and Later Gas Production with an increasing Gas Water Ratio trend.

3. The change in fluid saturations in the fracture network is the primary reason responsible for the two phase flow regimes observed. The gas saturation in fractures decreases during Early Gas Production phase; but increases during Late Gas Production Phase.

4. The material balance analysis suggest that the Early Gas Production phase indicates "fracture depletion" with negligible fluid communication with matrix. The Late Gas Production phase indicates significant pressure and fluid communication between fracture and matrix systems. The transition between the two flow regimes indicates the start of matrix depletion.

5. The effective fracture network can be modeled as a "two-phase tank" with arbitrary geometry during flowback period. During Early Gas Production phase, main drive mechanisms include expansion of free gas and water expansion in fractures, and fracture closure. During Late Gas Production phase, main drive mechanisms include expansion of free gas and water in fractures, fracture closure, and gas and water influx from the matrix.

Chapters 3 and 4

1. A closed-tank material balance model is developed to describe the two-phase flowback during Early Gas Production data. The model estimates the initial volume of the effective fracture network using the flowback rate and pressure profiles.

2. Volumetric analysis of the Horn River wells shows that most of the injected water is effective in creating the fractures. However, a significant portion of it is left in the formation and cannot be recovered during flowback. In addition, low water recovery suggest that most of the effective fractures comes from natural and secondary fractures. Also, application results show that wells flower earlier help clean the wellbore and might drain the fluids from the drainage area adjacent wells.

3. A flowing material balance model is developed by coupling the closed-tank material balance model with two-phase linear diffusivity equation. The outputs of the model include 1) fracture storage coefficient, which is a function of initial fracture volume, and 2) a

dimensionless fracture parameter, which is a function of fracture porosity and fracture permeability.

Chapter 5

1. An open-tank material balance model is derived to describe the flowback signatures during Late Gas Production. The model estimates the effective fracture-matrix interface area for long-time production.

2. A workflow is proposed to analyze two-phase flowback data in gas shales. The workflow include diagnostic analysis, flow regime identification, and material balance analysis.

3. Volumetric analysis suggest that fracture closure is the key drive mechanism during early-time flowback period. The excessive pressure drop causes a significant portion of the effective fracture volume to be lost during early-time flowback.

4. Comparative analysis suggests that a large portion of the effective fracture volume created during hydraulic fracturing may not contribute to fluid flow for long-time production. This result is supported by the low water recovery observed in the Horn River wells analyzed.

Chapter 6

1. An analytical model is developed to estimate fracture compressibility of hydraulically-fractured reservoirs. The model shows that the fracture compressibility consists of two parts: the rate of change in fracture porosity and fracture aperture with respect to the change in effective pressure.

2. Proppants play a significant role in resisting fracture closure. The propped fractures have compressibility values that are two orders of magnitude lower than those of the unpropped fractures.

3. Among various proppant parameters, proppant packing format is a key parameter controlling fracture compressibility values.

4. The compressibility of a fracture network is dominated by the unpropped fractures at low effective pressure, but is dominated by propped fractures at high effective pressure.

5. Severe fracture volume loss, low water recovery, and low hydrocarbon recovery are expected in hydraulically-fractured reservoirs with significant amount of re-activated natural fractures.

7.2 Recommendations

The following recommendations might be helpful to improve the results from this research and to extent this research and in future studies.

1. The proposed models in Chapters 3, 4, and 5 assume that each well produces from its own drainage area without considering inter-well communication. Future studies could take the well communication effect into account and extend the proposed models for flowback data analysis in a well pad or a "well group".

2. The proposed models in Chapters 3, 4, and 5 simplify the complex fracture network as a two-phase "tank", and describe the fracture closure behavoir using a fracture compressibility term. The proposed models neglect the geomechanical effects and assume constant fracture compressibility values during flowback period. Future studies could consider the change in fracture compressibility with time, especially during different flow regimes.

3. The proposed model in Chapter 5 assumes negligible water influx from the matrix during flowback period. Further studies can improve the model results by taking into account the water (both fracturing fluid and formation water) flow from the matrix to the fractures.

4. The proposed models in Chapters 5 and 6 assume shale matrix as a homogenous and isotropic continuum with constant propoerties (such as porosity, permeability, Young's modulus, and Poisson's ratio). In reality, shale is an anisotropic material. Future studies could include the heterogeneous and anisotropic properties of shale matrix using numerical methods and investigate the effects of anisotropic parameters on model outputs.

5. The proposed model in Chapter 5 considers the fracture compressibility and initial gas saturation as two unknown parameters. Future studies could reduce uncertainties of the model outputs by narrowing the search spaces for the two unknowns and/or by combining the outputs from independent fracture characterization techniques. For example, the fracture half-length from the microseismic interpretation could be used as constraints to screen out the outputs from flowback models.

6. The proposed model in Chapter 6 qualitatively explains the controlling parameters of fracture compressibility in propped fractures. However, there is lack of validation for the proposed model. Also, the unknown parameters restrict its applications for engineering studies. Future studies could focus on 1) validation of the proposed compressibility model using numerical simulation, and 2) simplification of the proposed model by reducing the number of unknown parameters.

7. The proposed model in Chapter 6 assumes that the fracture network is subject to an average effective pressure, without considering the direction/distributions of the fracture segments. The directions of fracture segments affect the effective pressure each fracture segment is subject to, and thus affect the average compressibility of the effective fracture network. Using numerical methods to investigate the effect of fracture distribution on the average fracture compressibility could be one focus for future study.

8. Future studies could also focus on 1) incorporating the fracture compressibility model in pressure/rate transient models for production and flowback data analysis in hydraulically-fractured unconventional reservoirs, and 2) investigating the effects of operational parameters on effective fracture network to optimize the designs of future fracturing operations.

9. Future studies could also focus on using results from other fracture characterization techniques (e.g. PTA/RTA, chemical analysis, microseismic imaging, and discrete fracture network model) to validate the flowback models. Comparison of fracture parameters from different methods helps the industry to better understand the stimulated reservoir.

Bibliography

Abbasi, M. A., Dehghanpour, H, Hawkes, R. V. 2012. Flowback Analysis for Fracture Characterization. Presented at the SPE Unconventional Resources Conference Canada, Calgary, Alberta, Canada, 30 October-1 November. SPE-162661-MS.

Abbasi M. A. 2013. *A Comparative Study of Flowback Rate and Pressure Transient Behavior in Multi fractured Horizontal Wells.* MSc. thesis, University of Alberta, Edmonton, Alberta.

Abbasi, M. A., Ezulike, D. O., Dehghanpour, H., Hawkes, R. V. 2014. A Comparative Study of Flowback Rate and Pressure Transient Behavior in Multifractured Horizontal Wells Completed in Tight Gas and Oil Reservoirs. *Journal of Natural Gas Science and Engineering* 17: 82-93.

Abouelresh, M., Slatt, R. M., 2012. Lithofacies and Sequence Stratigraphy of the Barnett Shale in East-Central Forth Worth Basin, Texas. *AAPG Bulletin*, 96 (1): 1–22.

Adefidipe, O. A., Dehghanpour, H., Virues, C. J. 2014. Immediate Gas Production from Shale Gas Wells: A Two-Phase Flowback Model. Presented at the SPE Unconventional Resources Conference, the Woodlands, Texas, U.S.A., 1-3 April. SPE-168982-MS.

Agarwal, R. G., Gardner, D. C., Kleinsteiber, S. W., Fussell, D. D. 1999. Analyzing Well Production Data Using Combined-Type-Curve and Decline-Curve-Analysis Concepts. *SPE Reservoir Evaluation & Engineering*, 2 (5): 478–486. SPE-57916-PA.

Aguilera, R. 1999. Recovery Factors and Reserves in Naturally Fractured Reservoirs. *Journal of Canadian Petroleum Technology*, 38 (07). PETSOC-99-07-DA.

Aguilera, R. 2006. Effect of Fracture Compressibility on Oil Recovery from Stress-Sensitive Naturally Fractured Reservoirs. *Journal of Canadian Petroleum Technology* 45 (12). PETSOC-06-12-01.

Aguilera, R. 2008. Effect of Fracture Compressibility on Gas-in-Place Calculations of Stress-Sensitive Naturally Fractured Reservoirs. *SPE Reservoir Evaluation & Engineering*, 11 (02): 307-310. SPE-100451-PA.

Ahmed, T. 2010. Reservoir Engineering Handbook (Fourth Edition). Gulf Professional Publishing.

Alkouh, A., McKetta, S., Wattenbarger, R. A. 2014. Estimation of Effective-Fracture Volume Using Water-Flowback and Production Data for Shale-Gas Wells. *Journal of Canadian Petroleum Technology*, 53 (05): 290-303. SPE-166279-PA.

Alotaibi, M. A., Miskimins, J. L. 2015. Slickwater Proppant Transport in Complex Fractures: New Experimental Findings & Scalable Correlation. Presented at the SPE Annual Technical Conference and Exhibition, Houston, Texas, U.S.A., 28-30 September. SPE-174828-MS.

Alramahi, B., Sundberg, M. I. 2012. Proppant Embedment and Conductivity of Hydraulic Fractures in Shales. Presented at the 46th U.S. Rock Mechanics/Geomechanics Symposium, Chicago, Illinois, 24-27 June. ARMA-2012-291.

Al-Hussainy, R., Ramey, H. J., Crawford, P. B. 1966. The Flow of Real Gases through Porous Media. *Journal of Petroleum Technology*, 18 (05): 624-636. SPE-1243-A-PA.

Anderson, D. M., Turco, F., Virues, C. J. J., Chin, A. 2013. Application of Rate Transient Analysis Workflow in Unconventional Reservoirs: Horn River Shale Gas Case Study. Presented at the SPE Unconventional Resources Conference and Exhibition-Asia Pacific, Brisbane, Australia, 11-13 November. SPE-167042-MS.

Arthur, J.D., B. Bohm, M. Layne. 2008. Hydraulic Fracturing Considerations for Natural Gas Wells of the Marcellus Shale. Presented at the GWPC Annual Forum in Cincinnati, OH. September 2008.

Anderson, D. M., Turco, F., Virues, C. J. J., Chin, A. 2013. Application of Rate Transient Analysis Workflow in Unconventional Reservoirs: Horn River Shale Gas Case Study. Presented at the SPE Unconventional Resources Conference and Exhibition-Asia Pacific, Brisbane, Australia, 11-13 November. SPE-167042-MS.

ASD Reports. *Spending on Proppants for Unconventional Oil & Gas to Total $8.85bn in 2014*. https://www.asdreports.com/news-2928/spending-proppants-unconventional-oil-gas-total-885bn-2014-according-new-study-asdreports.

Bai, M., Green, S., Suarez-Rivera, R. 2005. Effect of Leakoff Variation on Fracturing Efficiency for Tight Shale Gas Reservoirs. Presented at the 40th U.S. Symposium on Rock Mechanics (USRMS), 25-29 June, Anchorage, Alaska, U.S.A. ARMA-05-697.

Bandis, S.C., Lumsden A.C., Barton N.R., 1983. Fundamentals of Rock Joint Deformation. *International Journal of Rock Mechanics and Mining Sciences & Geomechanics Abstracts*, 20 (6): 249-268.

Bearinger, D. 2013. Message in a Bottle. Presented at the Unconventional Resources Technology Conference, Denver, Colorado, U.S.A., 12-14 August. URTEC-1618676-MS.

Bello, R.O., 2009. *Rate Transient Analysis in Shale Gas Reservoirs with Transient Linear Behavior*. Ph.D. thesis. Texas A & M University, College Station, Texas, U.S.A.

Bennion, D. B., Bietz, R. F., Thomas, F. B., Cimolai, M. P. 1994. Reductions in the Productivity of Oil and Low Permeability Gas Reservoirs due to Aqueous Phase Trapping. *Journal of Canadian Petroleum Technology*, 33 (09). PETSOC-94-09-05.

Bertoncello, A., Wallace, J., Blyton, C., Honarpour, M. M., Kabir, S. 2014. Imbibition and Water Blockage in Unconventional Reservoirs: Well-Management Implications during Flowback and Early Production. *SPE Reservoir & Evaluation*, 17 (04): 1094-6470. SPE-167698-PA.

B. C. Oil & Gas Commission. 2012. *Chemical Use in Hydraulic Fracturing*. http://fracfocus.ca/water-protection/drilling-usage. (Accessed July 27, 2018)

B. C. Oil & Gas Commission. 2014. Horn River Basin Unconventional Shale Gas Play Atlas.

Blatt, H., Tracy, R., Owens. B. 2005. Petrology: Igneous, Sedimentary and Metamorphic (Third Edition), W. H. Freeman Company.

Cao, P., Liu, J., Leong, Y. K. 2017. A Multiscale-Multiphase Simulation Model for the Evaluation of Shale Gas Recovery Coupled the Effect of Water Flowback. *Fuel*, 199: 191-205.

Canadian Society for Unconventional Resources, 2018. *Understanding Tight Oil*. http://www.mpgpetroleum.com/home/docs/Understanding_TightOil_FINAL.pdf. (Accessed July 27, 2018)

Chalmers, G. R., Ross, D. J., Bustin, R. M. 2012. Geological Controls on Matrix Permeability of Devonian Gas Shales in the Horn River and Liard Basins, Northeastern British Columbia, Canada. *International Journal of Coal Geology*, 103: 120-131.

Chang, C., Zoback, M. D., Khaksar, A. 2006. Empirical Relations between Rock Strength and Physical Properties in Sedimentary Rocks. *Journal of Petroleum Science and Engineering*, 51, (3–4): 223–237.

Chen, D., Pan, Z., Ye, Z. 2015. Dependence of Gas Shale Fracture Permeability on Effective Stress and Reservoir Pressure: Model Match and Insights. *Fuel*, 139: 383-392.

Chen, D., Pan, Z., Ye, Z., Hou, B., Wang, D., Yuan, L. 2016. A Unified Permeability and Effective Stress Relationship for Porous and Fractured Reservoir Rocks. *Journal of Natural Gas Science and Engineering*, 29: 401-412.

Cheng, W., Jin, Y., Chen, M. 2015. Experimental Study of Step-Displacement Hydraulic Fracturing on Naturally Fractured Shale Outcrops. *Journal of Geophysics and Engineering*, 12: 714-723.

Cheng, Y. 2012a. Impact of Water Dynamics in Fractures on the Performance of Hydraulically Fractured Wells in Gas-Shale Reservoirs. *Journal of Canadian Petroleum Technology*, 51 (02): 143-151. SPE-127863-PA.

Cheng, Y. 2012b. Impacts of the Number of Perforation Clusters and Cluster Spacing on Production Performance of Horizontal Shale-Gas Wells. *SPE Reservoir Evaluation & Engineering,* 15 (01): 31-40. SPE-138843-PA.

Cipolla, C. L., Lolon, E. P., Erdle, J. C., Rubin, B. 2010. Reservoir Modeling in Shale-Gas Reservoirs. *SPE Reservoir Evaluation & Engineering*, 13 (04): 638-653. SPE-125530-PA.

Clarkson, C. R., Williams-Kovacs, J. 2013. Modeling Two-Phase Flowback of Multifractured Horizontal Wells Completed in Shale. *SPE Journal*, 18 (04): 795-812. SPE-162593-PA.

Cooke, C. E. 1977. Fracturing With a High-Strength Proppant. *Journal of Petroleum Technology*, 29 (10): 1222 - 1226. SPE-6213-PA.

Crafton, J. W., Gunderson, D. W. 2006. Use of Extremely High Time-Resolution Production Data to Characterize Hydraulic Fracture Properties. Presented at the SPE Annual Technical Conference and Exhibition, San Antonio, Texas, U.S.A., 24-27 September. SPE-103591-MS.

Crafton, J. W., Gunderson, D. W. 2007. Stimulation Flowback Management - Keeping a Good Completion Good. Presented at the SPE Annual Technical Conference and Exhibition, Anaheim, California, U.S.A., 11-14 November. SPE-110851-MS.

Crafton, J. 2015. Maximize Recovery by Minimizing Production Delays and Shut-ins. *Journal of Petroleum Technology*, 67 (06). SPE-0615-0032-JPT.

Craig, D.P. 2006. *Analytical Modeling of a Fracture-injection/Fall-off Sequence and the Development of a Refracture Candidate Diagnostic Test*. Ph.D. thesis. Texas A&M University, College Station, Texas.

Curtis, J. B. 2002. Fractured Shale-Gas Systems. *AAPG Bulletin (2002)*, 86 (11): 1921-1938.

Dehghanpour, H., Lan, Q., Saeed, Y., Fei, H., Qi, Z. 2013. Spontaneous Imbibition of Brine and Oil in Gas Shales: Effect of Water Adsorption and Resulting Microfractures. *Energy & Fuels*, 27(6): 3039-3049.

Dehghanpour, H., Zubair, H.A., Chhabra, A., Ullah, A. 2012. Liquid Intake of Organic Shales. *Energy & Fuels*, 26 (9): 5750-5758.

Duan, Y., Jing, X., Meng, Y., Luo, P. 2000. Closure Behaviour of Natural Rock Fractures. Presented at the SPE/AAPG Western Regional Meeting, Long Beach, California. 19-22 June. SPE-62539-MS.

Economides, M. J., Nolte, K.G. 1989. Reservoir Stimulation (Third Edition). John Wiley & Sons, Inc.

Edwards, R. W., Celia, M. A., Bandilla, K. W., Doster, F., Kanno, C. M. 2015. A Model to Estimate Carbon Dioxide Injectivity and Storage Capacity for Geological Sequestration in Shale Gas Wells. *Environmental Science & Technology*, 49 (15): 9222-9229.

Edwards, R. W. J., Celia, M. A. 2018. Shale Gas Well, Hydraulic Fracturing, and Formation Data to Support Modeling of Gas and Water Flow in Shale Formations. *Water Resources Research*, 54: 3196–3206.

EIA. 2012. *Pad Drilling and Rig Mobility Lead to More Efficient Drilling*. U.S. Energy Information Administration, 11 September 2012, https://www.eia.gov/todayinenergy/detail.php?id=7910# (Accessed 25 July 2018).

EIA. 2015. *World Shale Resource Assessments*. U.S. Energy Information Administration, 24 September 2015, http://www.eia.gov/analysis/studies/worldshalegas/ (accessed 25 July 2018).

EIA. 2018. *Annual Energy Outlook 2018*. U.S. Energy Information Administration, 6 February 2018, http://www.eia.gov/outlooks/aeo/ (accessed 25 July 2018).

El-Banbi, A. H., Wattenbarger, R. A. 1998. Analysis of Linear Flow in Gas Well Production. Presented at the SPE Gas Technology Symposium, Calgary, Alberta, Canada, 15-18 March. SPE-39972-MS.

Engelder, T., Lash, G. G., Uzcátegui, R. S. 2009. Joint sets that enhance production from Middle and Upper Devonian gas shales of the Appalachian Basin. *AAPG Bulletin (2009)*, 93 (7): 857-889.

Engelder, T., Cathles, L. M., Bryndzia, L. T. 2014. The Fate of Residual Treatment Water in Gas Shale. *Journal of Unconventional Oil and Gas Resources*, 7, 33-48.

Ezulike, D. O., Dehghanpour, H. 2014a. A Model for Simultaneous Matrix Depletion into Natural and Hydraulic Fracture Networks. *Journal of Natural Gas Science and Engineering*, 16: 57-69.

Ezulike, D. O., Dehghanpour, H. 2014b. Modelling Flowback as a Transient Two-Phase Depletion Process. *Journal of Natural Gas Science and Engineering*, 19: 258-278.

Ezulike, D. O., Dehghanpour, H., Virues, C.J., Hawkes, R.V., Steven Jones, R., 2016. Flowback Fracture Closure: A Key Factor for Estimating Effective Pore-Volume. *SPE Reservoir & Evaluation*, 19 (04): 567 - 582. SPE-175143-PA.

Fakcharoenphol, P., Kurtoglu, B., Kazemi, H., Charoenwongsa, S., Wu, Y. S. 2014. The Effect of Osmotic Pressure on Improve Oil Recovery from Fractured Shale Formations. Presented at the SPE Unconventional Resources Conference, Woodlands, Texas, U.S.A., 1-3 April. SPE-198998-MS.

Fisher, M. K., Heinze, J. R., Harris, C. D., Davidson, B. M., Wright, C. A., Dunn, K. P. 2004. Optimizing Horizontal Completion Techniques in the Barnett Shale Using Microseismic Fracture Mapping. Presented at the SPE Annual Technical Conference and Exhibition, Houston, Texas, 26-29 September. SPE-90051-MS.

Fisher, M. K., Wright, C. A., Davidson, B. M., Steinsberger, N. P., Buckler, W. S., Goodwin, A., Fielder, E. O. 2005. Integrating Fracture Mapping Technologies to Improve Stimulations in the Barnett Shale. *SPE Production & Facilities*, 20 (02): 85 - 93. SPE-77441-PA.

Fredd, C. N., McConnell, S. B., Boney, C. L., England, K. W. 2001. Experimental Study of Fracture Conductivity for Water-Fracturing and Conventional Fracturing Applications. *SPE Journal*, 6(03): 288 - 298. SPE-74138-PA.

Friends of the Earth. 2017. *Fracking: the Facts.* https://friendsoftheearth.uk/climate-change/fracking-facts (Accessed 25 July 2018).

Fu, Y., Dehghanpour, H., Ezulike, D. O., Jones Jr, R. S. 2017. Estimating Effective Fracture Pore Volume From Flowback Data and Evaluating Its Relationship to Design Parameters of Multistage-Fracture Completion. *SPE Production & Operations*, 32 (04): 423 - 439. SPE-175892-PA.

Gale, J. F. W., Laubach, S. E., Olson, J. E., Eichhubl, P., Fall, A. 2014. Natural Fractures in Shale: A Review and New Observations. *AAPG Bulletin*, 98 (11): 2165–2216.

Gangi, A.F. 1978. Variation of Whole and Fractured Porous Rock Permeability with Confining Pressure. *International Journal of Rock Mechanics and Mining Sciences & Geomechanics Abstracts*, 15 (5): 249-257.

Gdanski, R. D., Fulton, D. D., Shen, C. 2009. Fracture-Face-Skin Evolution during Cleanup. *SPE Production & Operations* 24, (01): 22-34. SPE 101083-PA.

Ghanbari, E., Bearinger, D., Abbasi, M. A., Dehghanpour, H. 2013. Flowback Volumetric and Chemical Analysis for Evaluating Load Recovery and Its Impact on Early-Time Production. Presented at the SPE Unconventional Resources Conference Canada, Calgary, Alberta, Canada, 5-7 November. SPE-167165-MS.

Ghanbari, E., Dehghanpour, H. 2016. The Fate of Fracturing Water: A Field and Simulation Study. *Fuel*, 163 (1): 282–294.

Government of Western Australia, Department of Mines, Industry Regulation and Safety. *Hydraulic Fracture Stimulation*. http://www.dmp.wa.gov.au/Petroleum/Hydraulic-fracture-stimulation-20018.aspx. (Accessed 25 July 2018)

Gray, H. E. 1978. Gray, H. E. 1978. *Vertical Flow Correlation - Gas Wells*. User Manual for API 14B, Subsurface Controlled Safety Valve Sizing Computer Program.

Gross, M. R., 1995. Fracture partitioning: Failure Mode as a Function of Lithology in the Monterey Formation of Coastal California: *Geological Society of America Bulletin*, 107 (7): 779–792.

Hall, C. D.; Debra, J., Randy, M. 2011. Comparison of the Reservoir Properties of the Muskwa (Horn River Formation) with Other North American Gas Shales. Presented at the 2011 CSPG CSEG CWLS Convention.

Harris, N. B., Dong, T. 2013. Characterizing Porosity in the Horn River Shale, Northeastern British Columbia; in Geoscience Reports 2013, *British Columbia Ministry of Natural Gas Development*: 33-40.

Heller, R., Vermylen, J., Zoback, M. 2014. Experimental Investigation of Matrix Permeability of Gas Shales. *AAPG Bulletin*, 98 (5): 975-995.

Helms L. 2008. Horizontal Drilling. *DMR Newsletter* 35 (1): 1-3.

Hertz, H. 1882. Über die berührung fester elastischer Körper (On the Contact of Rigid Elastic Solids). In: *Miscellaneous Papers*.

Hoek, E., Brown, E.T., 1997. Practical Estimates of Rock Mass Strength. *International Journal of Rock Mechanics and Mining Sciences*, 34 (08): 1165-1186.

Holditch, S. A. 1979. Factors Affecting Water Blocking and Gas Flow from Hydraulically Fractured Gas Wells. *Journal of Petroleum Technology*, 31 (12): 1-515. SPE-7561-PA.

Huang, X., Bandilla, K. W., Celia, M. A. 2016. Multi-Physics Pore-Network Modeling of Two-Phase Shale Matrix Flows. *Transport in Porous Media*, 111(1): 123-141.

Huo, D., Li, B., Benson, S. M. 2014. Investigating Aperture-Based Stress-Dependent Permeability and Capillary Pressure in Rock Fractures. Presented at the SPE Annual Technical Conference and Exhibition, Amsterdam, The Netherlands, 27-29 October. SPE-170819-MS.

Ilk, D., Currie, S. M., Symmons, D., Rushing, J. A., Broussard, N. J., Blasingame, T. A. 2010. A Comprehensive Workflow for Early Analysis and Interpretation of Flowback Data from Wells in Tight Gas/Shale Reservoir Systems. Presented at the SPE Annual Technical Conference and Exhibition, Florence, Italy, 19-22 September. SPE-135607-MS.

Ilk, D., Currie, S. M., Blasingame, T. A. 2010. Production Analysis and Well Performance Forecasting of Tight Gas and Shale Gas Wells. Presented at SPE Eastern Regional Meeting, Morgantown, West Virginia, U.S.A., 13-15 October. SPE-139118-MS.

Ingraham, M. D., Bauer, S. J., Quintana, E. C., Bolintineau, D., Rao, R. R., Lechman, J. B. 2015. Proppant and Host Rock Deformation in Fractured Shale flow through Experiments. Presented at the 49th U.S. Rock Mechanics/Geomechanics Symposium, 28 June - 1 July, San Francisco, California. ARMA 15-0102.

Jaeger, J.C., Cook, N.G.W., Zimmerman, R. 2007. Fundamentals of Rock Mechanics (Fourth Edition). Blackwell Publishing.

Jansen, T. A., Zhu, D., Hill, A. D. 2015. The Effect of Rock Mechanical Properties on Fracture Conductivity for Shale Formations. Presented at the SPE Hydraulic Fracturing Technology Conference, The Woodlands, Texas, U.S.A., 3-5 February. SPE-173347-MS.

Javadpour, F. 2009. Nanopores and Apparent Permeability of Gas Flow in Mudrocks (Shales and Siltstone). *Journal of Canadian Petroleum Technology*, 48(08): 16-21. PETSOC-09-08-16-DA.

Johnson, M. F., Walsh, W., Budgell, P. A., Davidson, J. A. 2011. The Ultimate Potential for Unconventional Gas in the Horn River Basin: Integrating Geological Mapping with Monte Carlo Simulations. Presented at the Canadian Unconventional Resources Conference, Calgary, Alberta, Canada, 15-17 November. SPE-148976-MS.

Jones, F.O., 1982. A Laboratory Study of the Effects of Confining Pressure on Fracture Flow and Storage Capacity in Carbonate Rocks. *Journal of Petroleum Technology* (27) 01: 21-27. SPE-4569-PA.

Jack R. J., Larry K. B. 2009. Design and Appraisal of Hydraulic Fractures. Society of Petroleum Engineers.

Jones, R. S., Pownall, B., Franke, J. 2014. Estimating Reservoir Pressure from Early Flowback Data. Presented at the SPE/AAPG/SEG Unconventional Resources Technology Conference, Denver, Colorado, U.S.A., 25-27 August. SPE-2014-1934785-MS.

Kamali, A., Pournik, M. 2015. Fracture Closure and Conductivity Decline Modeling – Application in Unpropped and Acid Etched Fractures. *Journal of Unconventional Oil and Gas Resources,* 14: 44-55.

Katahara, K. 2008. What is Shale to a Petrophysicist? *The Leading Edge*, 27(6): 738-741.

Kern, L. R., Perkins, T. K., & Wyant, R. E. 1959. The Mechanics of Sand Movement in Fracturing. *Journal of Petroleum Technology*, 11 (07): 55-57. SPE-1108-G.

Krumbein, W.C., Sloss, L. L. 1951. Stratigraphy and Sedimentation, W. H. Freeman & Co., San Francisco.

Kuchuk, F. J., Biryukov, D., Fitzpatrick, T. 2014. Rate Transient and Decline Curve Analyses for Continuously (Dual-Porosity) and Discretely Naturally Fractured Reservoirs. Presented at the SPE Annual Technical Conference and Exhibition, Amsterdam, Netherlands, 27-29 October. SPE-170698-MS.

Li, C., Lafollette, R., Sookprasong, A., Wang, S. 2013. Characterization of Hydraulic Fracture Geometry in Shale Gas Reservoirs Using Early Production Data. Presented at the International Petroleum Technology Conference, Beijing, China, 26-28 March. IPTC-16896-MS.

Li, K., Gao, Y., Lyu, Y., Wang, M. 2015. New Mathematical Models for Calculating Proppant Embedment and Fracture Conductivity. *SPE Journal*, 20 (03): 496 - 507. SPE-155954-PA.

Liang, F., Sayed, M., Al-Muntasheri, G.A., Chang, F.F., Li. L. 2016. A Comprehensive Review on Proppant Technologies. *Petroleum*, 2 (1): 26-39.

Liu, F., Gordon, P.A., Valiveti, D.M. 2018. Modeling Competing Hydraulic Fracture Propagation with the Extended Finite Element Method. *Acta Geotechnica*, 13 (02): 243-265.

Liu, N., Liu, M., Zhang, S. 2015. Flowback Patterns of Fractured Shale Gas Wells. *Natural Gas Industry B*, 2, 2-3: 247-251.

Liu, Y. 2017. *Modeling of Recovery and In-situ Distribution of Fracturing Fluid in Shale Gas Reservoirs Due to Fracture Closure, Proppant Distribution and Gravity Segregation*. MSc. thesis, University of Alberta, Edmonton, Alberta.

Lutynski, M. A., 2015. A Method of Proppant Pack Permeability Assessment. *Physicochemical Problems of Mineral Processing*, 51(1): 325-334.

Makhanov, K., Habibi, A., Dehghanpour, H., Kuru, E. 2014. Liquid Uptake of Gas Shales: A Workflow to Estimate Water Loss during Shut-in Periods after Fracturing Operations. *Journal of Unconventional Oil and Gas Resources*, 7: 22-32. SPE-167157-MS.

Martin, J. C. 1959. Simplified Equations of Flow in Gas Drive Reservoirs and the Theoretical Foundation of Multiphase Pressure Buildup Analyses. SPE-1235-G.

Mattar, L., Anderson, D. 2005. Dynamic Material Balance (Oil or Gas-In-Place without Shut-Ins). Presented at the Canadian International Petroleum Conference, Calgary, Alberta. Canada, 7-9 June. PETSOC-2005-113.

Maxwell, S.C. 2011. What Does Microseismic Tell Us about Hydraulic Fracturing? Presented at the SPE Annual Technical Conference and Exhibition, Denver, Colorado, U.S.A., 30 October-2 November. SPE-146932-MS.

Meyer, B. R., Bazan, L. W., Jacot, R. H., Lattibeaudiere, M. G. 2010. Optimization of Multiple Transverse Hydraulic Fractures in Horizontal Wellbores. Presented at the SPE Unconventional Gas Conference, Pittsburgh, Pennsylvania, U.S.A., 23-25 February. SPE-131732-MS.

Moghadam, S., Jeje, O., Mattar, L. 2011. Advanced Gas Material Balance in Simplified Format. *Journal of Canadian Petroleum Technology*, 50 (01): 90-98. SPE-139428-PA.

Montgomery, C. 2012. *Effective and Sustainable Hydraulic Fracturing: Fracturing Fluids*. InTech.

Motealleh, S., Bryant, S. L. 2009. Quantitative Mechanism for Permeability Reduction by Small Water Saturation in Tight-Gas Sandstones. *SPE Journal*, 14(02): 252-258. SPE-107950-PA.

Neuzil, C. E., 1994. How Permeable are Clays and Shales? *Water Resources Research*, 30 (2): 145-150.

Noe, S., Crafton, J. W. 2013. Impact of Delays and Shut-Ins on Well Productivity. Presented at the SPE Eastern Regional Meeting, Pittsburgh, Pennsylvania, U.S.A., 20-22 August. SPE-165705-MS.

Palacio, J. C., Blasingame, T. A. 1993. Decline Curve Analysis Using Type Curves: Analysis of Gas Well Production Data. Presented at the SPE Rocky Mountain Regional/Low Permeability Reservoirs Symposium, Denver, Colorado, 12-14 April. SPE-25909-MS.

Parmar, J., Dehghanpour, H., Kuru, E. 2014. Displacement of Water by Gas in Propped Fractures: Combined Effects of Gravity, Surface Tension, and Wettability. *Journal of Unconventional Oil and Gas Resources*, 5: 10-21.

Patzek, T. W., Male, F., Marder, M. 2013. Gas Production in the Barnett Shale Obeys a Simple Scaling Theory. *Proceedings of the National Academy of Sciences*, 110(49): 19731-19736.

Penny, G. S., Conway, M. W., Lee, W. 1985. Control and Modeling of Fluid Leakoff during Hydraulic Fracturing. *Journal of Petroleum Technology*, *37*(06): 1-071. SPE-12486-PA.

Penny, G. S., Dobkins, T. A., Pursley, J. T. 2006. Field Study of Completion Fluids to Enhance Gas Production in the Barnett Shale. Presented at the SPE Gas Technology Symposium, 15-17 May, Calgary, Alberta, Canada. SPE-100434-MS.

Perez Pena, P., Zhu, D., Hill, A. D. 2016. The Effect of Rock Properties on Fracture Conductivity in the Marcellus Shale. Presented at the SPE Asia Pacific Hydraulic Fracturing Conference, Beijing, China, 24-26 August. SPE-181867-MS.

Perkins, T. K., Kern, L. R. 1961. Widths of Hydraulic Fractures. *Journal of Petroleum Technology*, 13(09): 937 - 949. SPE-89-PA.

Prabhakaran, R., De Pater, H., Shaoul, J. 2017. Pore Pressure Effects on Fracture Net Pressure and Hydraulic Fracture Containment: Insights from an Empirical and Simulation Approach. *Journal of Petroleum Science and Engineering*, 157: 724-736.

Rahman, N. M. A., Mattar, L., Anderson, D. M. 2006a. New, Rigorous Material Balance Equation for Gas Flow in a Compressible Formation with Residual Fluid Saturation. Presented at the SPE Gas Technology Symposium, Calgary, Alberta, Canada, 15-17 May. SPE-100563-MS.

Rahman, N. M. A., Kok, L., Zaoral, K. 2006b. A New Method for Computing Pseudo-Time for Real Gas Flow Using the Material Balance Equation. *Journal of Canadian Petroleum Technology*, 45(10): 36-44. PETSOC-2004-182.

Reinicke, A. 2009. *Mechanical and Hydraulic Aspects of Rock-Proppant Systems: Laboratory Experiments and Modelling Approaches*. Ph.D. thesis. University of Potsdam, Potsdam, Brandenburg, Germany.

Rezaee, R. 2015. Fundamentals of Gas Shale Reservoirs. John Wiley & Sons, Inc.

Ross, D. J., Bustin, R. M. 2008. Characterizing the Shale Gas Resource Potential of Devonian–Mississippian Strata in the Western Canada Sedimentary Basin: Application of an Integrated Formation Evaluation. AAPG bulletin, 92(1): 87-125.

Rogers, S., Elmo, D., Dunphy, R., Bearinger, D. 2010. Understanding Hydraulic Fracture Geometry and Interactions in the Horn River Basin through DFN and Numerical Modeling. Presented at the Canadian Unconventional Resources and International Petroleum Conference, Calgary, Alberta, 19-21 October. SPE-137488-MS.

Sahai, R., Miskimins, J. L., Olson, K. E. 2014. Laboratory Results of Proppant Transport in Complex Fracture Systems. Presented at the SPE Hydraulic Fracturing Technology Conference, The Woodlands, Texas, U.S.A., 4-6 February. SPE-168579-MS.

Salah, M., Orr, D., Meguid, A. A., Crane, B., Squires, S. 2016. Multistage Horizontal Hydraulic Fracture Optimization through an Integrated Design and Workflow in Apollonia Tight Chalk, Egypt from the Laboratory to the Field. Presented at the Abu Dhabi International Petroleum Exhibition & Conference, Abu Dhabi, UAE, 7-10 November. SPE-183068-MS.

Seidle, J. P., Jeansonne, M. W., Erickson, D. J. 1992. Application of Matchstick Geometry to Stress Dependent Permeability in Coals. Presented at the SPE Rocky Mountain Regional Meeting, Casper, Wyoming, U.S.A., 18-21 May. SPE-24361-MS.

Sharma, M. M., Manchanda, R. 2015. The Role of Induced Un-Propped (IU) Fractures in Unconventional Oil and Gas Wells. Presented at the SPE Annual Technical Conference and Exhibition, Houston, Texas, U.S.A., 28-30 September. SPE-174946-MS.

Shen, Y., Ge, H., Li, C., Yang, X., Ren, K., Yang, Z., Su, S. 2016. Water Imbibition of Shale and Its Potential Influence on Shale Gas Recovery—A Comparative Study of Marine and Continental Shale Formations. *Journal of Natural Gas Science and Engineering*, 35, 1121-1128.

Singh, V. K. 2013. Overview of Material Balance Equation (MBE) in Shale Gas and Non-Conventional Reservoir. Presented at the SPE Middle East Oil and Gas Show and Conference, Manama, Bahrain, 10-13 March. SPE-164427-MS.

Stehfest, H., 1970. Algorithm 358-Numerical Inversion of Laplace Transforms. *Communications of the ACM*, 13 (1): 47-49.

Syfan, F. E., Newman, S. C., Meyer, B. R., Behrendt, D. M. 2007. Case History: G-Function Analysis Proves Beneficial in Barnett Shale Application. Presented at the SPE Annual Technical Conference and Exhibition, 11-14 November, Anaheim, California, U.S.A. SPE-110091-MS.

Tabatabaie, S. H., Mattar, L., Pooladi-Darvish, M. 2013. Pseudotime Calculation in Low Permeability Gas Reservoirs. Presented at the SPE Unconventional Resources Conference Canada, Calgary, Alberta, Canada, 5-7 November. SPE-167185-MS.

Taiebat, M., Mutabaruka, P., Pellenq. R, Radjai, F. 2017. Effect of Particle Size Distribution on 3D Packings of Spherical Particles. Presented at the Powders and Grains 2017 – 8th International Conference on Micromechanics on Granular Media. *EPJ Web of Conferences*, 140, 02030.

Tokunaga,T., Cihan, A., Wan, J., Kim, Y., Shen, W. 2016. *Understanding Water Controls on Shale Gas Mobilization*. U.S. Department of Energy & National Energy Technology Laboratory. ESD14085.

Terzaghi, K., 1923. Die Berechnungder Durchlassigkeitsziffer des Tones aus dem Verlauf der hydrodynamischen Spannungserscheinungen (Calculation of the Porosity Index of Clay from Hydrodynamic Tension Conditions). Sitzbericht (Abt. IIa) Akademie der Wissenschaften, Vienna, 132.

Tkhostov, B.A., Verziroba, A.D., Vendel'shteyn, B.Y., Dobrynin, V.M. 1970. Oil in Fractured Reservoirs. Leningrad: Izd. Nedra.

Tsang, Y. W., Witherspoon, P. A. 1981. Hydromechanical Behavior of a Deformable Rock Fracture Subject to Normal Stress. *Journal of Geophysical Research*, 86 (B10): 9287-9298.

Van Everdingen, A.F., Hurst, W., 1949. The Application of the Laplace Transformation to Flow Problems in Reservoirs. *Journal of Petroleum Technology*, 1 (12): 305-324. SPE-949305-G.

Virues, C., Lypkie, K., Pyecroft, J., Zafar, H., Lehmann, J., Hendrick, J. 2015. Going from Conceptual to Analytical Drilling/Completions/Reservoir Guided Model of a Cased Uncemented Multi-Fractured Horizontal Well in the Canadian Horn River Basin. Presented at the SPE/CSUR Unconventional Resources Conference, Calgary, Alberta, Canada, 20-22 October. SPE-175932-MS.

Virues, C., Budge, J., Von Lunen, E. 2016a. Value of Integrated Geophysics – Microseismic-Derived Ultimate Expected Fracture Half-Length in SRV in a Multi-Staged Pad in the Horn River Basin. *Recorder*, 41 (04).

Virues, C., Wang, A., Pyecroft, J., Lehmann, J., Petr, C., Hendrick, J., Kuang, Z. 2016b. Performance of Plugless Toe Stages and Non-Isolated Wellbore in Multi-Stage Hydraulic Fractured 10 Well Half Pad in the Canadian Shale Gas Horn River Basin. Presented at the SPE Hydraulic Fracturing Technology Conference, the Woodlands, Texas, U.S.A., 9-11 February. SPE-179128-MS.

Wang, H., Sharma, M. M. 2017. A Non-local Model for Fracture Closure on Rough Fracture Faces and Asperities. *Journal of Petroleum Science and Engineering,* 154: 425-437.

Wang, H., Sharma, M. M. 2018. Modeling of Hydraulic Fracture Closure on Proppants with Proppant Settling. *Journal of Petroleum Science and Engineering*, 171: 636-645.

Wang, M., Leung, J. Y. 2016. Numerical Investigation of Coupling Multiphase Flow and Geomechanical Effects on Water Loss during Hydraulic-Fracturing Flowback Operation. *SPE Reservoir Evaluation & Engineering* 19 (03): 520 - 537. SPE-178618-PA.

Warpinski, N. R., Mayerhofer, M. J., Vincent, M. C., Cipolla, C. L., Lolon, E. 2008. Stimulating Unconventional Reservoirs: Maximizing Network Growth While Optimizing Fracture Conductivity. Presented at the SPE Unconventional Reservoirs Conference, 10-12 February, Keystone, Colorado, U. S. A. SPE-114173-MS.

Wattenbarger, R. A., Alkouh, A. B. 2013. New Advances in Shale Reservoir Analysis Using Flowback Data. Presented at the SPE Eastern Regional Meeting, Pittsburgh, Pennsylvania, U.S.A., 20-22 August. SPE-165721-MS.

Weng, X., Kresse, O., Cohen, C.-E., Wu, R., Gu, H. 2011. Modeling of Hydraulic-Fracture-Network Propagation in a Naturally Fractured Formation. *SPE Journal*, 26 (04). SPE-140253-PA.

Williams-Kovacs, J. D., Clarkson, C. R., Zanganeh, B. 2015. Case Studies in Quantitative Flowback Analysis. Presented at the SPE/CSUR Unconventional Resources Conference, Calgary, Alberta, Canada, 20-22 October. SPE-175983-MS.

World Energy Council. 2016. *World Energy Resources 2016*, https://www.worldenergy.org/wp-content/uploads/2016/10/World-Energy-Resources_Report_2016.pdf. (Accessed 25 July 2018).

Wu, H., Fu, P., Yang, X., Morris, J. P. 2018. Imaging Hydraulic Fracture Extents and Aperture Using Electrical Resistivity Tomography. Presented at the 3rd Workshop on Geothermal Reservoir Engineering, Stanford University, Stanford, California, February 12-14. SGP-TR-213.

Wu, R., Kresse, O., Weng, X., Cohen, C.-E., Gu, H. 2012. Modeling of Interaction of Hydraulic Fractures in Complex Fracture Networks. Presented at the SPE Hydraulic Fracturing Technology Conference, the Woodlands, Texas, U.S.A., 6-8 February. SPE-152052-MS.

Xu, M., Dehghanpour, H. 2014. Advances in Understanding Wettability of Gas Shales. *Energy & Fuels*, 28(7), 4362-4375.

Xu, Y., Adefidipe, O. A., Dehghanpour, H. 2015. Estimating Fracture Volume Using Flowback Data from the Horn River Basin: A Material Balance Approach. *Journal of Natural Gas Science and Engineering*, 25: 253-270.

Xu, Y., Adefidipe, O. A., Dehghanpour, H. 2016a. A Flowing Material Balance Equation for Two-Phase Flowback Analysis. *Journal of Petroleum Science and Engineering*, 142, 170-185.

Xu, Y., Ezulike, O. D., Zolfaghari, A., Dehghanpour, H., Virues, C. 2016b. Complementary Surveillance Microseismic and Flowback Data Analysis: An Approach to Evaluate Complex Fracture Networks. Presented at the SPE Annual Technical Conference and Exhibition, Dubai, UAE, 26-28 September. SPE 181693-MS.

Xu, Y., Dehghanpour, H., Ezulike, D. O., Virues, C. 2017. Effectiveness and Time Variation of Induced Fracture Volume: Lessons from Water Flowback Analysis. *Fuel*, 210 (15): 844-858.

Yaich, E., Williams, S., Bowser, A., Goddard, P., Souza, O. C. D. de, Foster, R. A. 2015. A Case Study: The Impact of Soaking on Well Performance in the Marcellus. Presented at the

Unconventional Resources Technology Conference, San Antonio, Texas, U.S.A., 20-22 July. URTEC-2154766-MS.

Yang, R., Huang, Z., Li, G., Yu, W., Sepehrnoori, K., Lashgari, H. R., Tian, S., Song, X., Sheng, M. 2017. A Semianalytical Approach to Model Two-Phase Flowback of Shale-Gas Wells with Complex-Fracture-Network Geometries. *SPE Journal*, 22 (06): 1,808 - 1,833. SPE-181766-PA.

Yarushina, V. M., Bercovici, D., Oristaglio, M. L. 2013. Rock Deformation Models and Fluid Leak-Off in Hydraulic Fracturing. Geophysical Journal International, 199 (3): 1514-1526.

Younes, A. I., H. Moore, N. Suurmeyer, P. R. Smith, and M. Sandstrom. 2011. Development of Mechanically Layered Haynesville-Bossier Shale-Gas Play: Search and Discovery. Presented at the AAPG Annual Convention and Exhibition, April 10-13, Houston, Texas, U.S.A. AAPG 50460.

Yu, W., Sepehrnoori, K. 2014. Simulation of Gas Desorption and Geomechanics Effects for Unconventional Gas Reservoirs. *Fuel*, *116*, 455-464.

Zhang, J., Kamenov, A., Hill, A. D., Zhu, D. 2014. Laboratory Measurement of Hydraulic-Fracture Conductivities in the Barnett Shale. *SPE Production & Operations*, 29 (03): 216-227. SPE-163839-PA.

Zhang, X., R. G. Jeffrey, M. Thiercelin, 2009. Mechanics of Fluid-Driven Fracture Growth in Naturally Fractured Reservoirs with Simple Network Geometries: *Journal of Geophysical Research*, 114, B12406.

Zhang, Y., Ehlig-Economides, C. 2014. Accounting for Remaining Injected Fracturing Fluid in Shale Gas Wells. Pressented at the SPE/AAPG/SEG Unconventional Resources Technology Conference, Denver, Colorado, U.S.A., 25-27 August. URTec-1892994.

Zimmerman, R.W. 1991. Compressibility of Sandstones (First Edition). Elsevier Science Publishers B.V.

Zimmerman, R.W., Somerton, W.H., King, M.S. 1986. Compressibility of Porous Rocks. *Journal of Geophysical Research*, 91 (B12): 12765-12777.

Zolfaghari, A., Dehghanpour, H., Ghanbari, E., Bearinger, D. 2016. Fracture Characterization Using Flowback Salt-Concentration Transient. *SPE Journal*, 21 (01), 233-244. SPE-168598-PA.

Appendix A: Derivation of the Closed-Tank Material Balance Equation for the Effective Fracture System

The MBE for the effective fracture system is given by:

Mass In (from Matrix) – Mass Out = Mass Accumulation in the Effective Fracture System

Eq. A.1 gives the MBE for the gas phase:

$$0 - q_g \rho_g^o = \frac{\partial}{\partial t}\left[V_g(t)\rho_g^R\right] \quad \text{(A.1)}$$

where ρ_g^o and ρ_g^R are the density of gas at surface and at reservoir conditions, respectively. V_g represents the volume of gas in the fractures at any time during EGP phase. Since the effective fracture volume is considered as a closed tank during EGP, the mass of gas influx from the matrix is zero.

The effective fracture volume is always completely filled with gas and water. Therefore, V_g can be related to the effective fracture volume (V_f) and volume of water in the fractures (V_w) as:

$$V_g(t) = V_f(t) - V_w(t): \quad \text{(A.2)}$$

Substituting Eq. A.2 into Eq. A.1 gives

$$-q_g \rho_g^o = \frac{\partial}{\partial t}\left[\left(V_f - V_w\right)\rho_g^R\right] \quad \text{(A.3)}$$

$\frac{\partial \rho_g^R}{\partial t}$ can be related to the isothermal gas compressibility (c_g) as

$$c_g = -\frac{1}{V_g}\frac{\partial V_g}{\partial P_f} = \frac{1}{\rho_g}\frac{\partial \rho_g}{\partial P_f} = \frac{1}{\rho_g}\frac{\partial \rho_g}{\partial t}\frac{\partial t}{\partial P_f} \quad \text{(A.4)}$$

Expanding Eq. A.3 using chain rule and substituting Eq. A.4 gives

$$-q_g \rho_g^o = \rho_g^R \frac{\partial}{\partial t}\left(V_f - V_w\right) + \left(V_f - V_w\right)\frac{\partial \rho_g^R}{\partial t} = \rho_g^R \frac{\partial}{\partial t}\left(V_f - V_w\right) + V_g \rho_g^R c_g \frac{\partial P_f}{\partial t} \quad \text{(A.5)}$$

Dividing ρ_g^R on both sides of Eq. A.5 gives

$$-q_g B_g = V_g c_g \frac{\partial P_f}{\partial t} - \frac{\partial V_w}{\partial t} + \frac{\partial V_f}{\partial t} \quad \text{(A.6)}$$

V_g and V_w can be defined as functions of cumulative gas and water production:

$$V_g = (G_{fi} - G_p)B_g \tag{A.7}$$

$$V_w = (W_{fi} - W_p)B_w \tag{A.8}$$

Substituting Eqs. A.7 and A.8 into Eq. A.6 gives

$$-q_g B_g = (G_{fi} - G_p)B_g c_g \frac{\partial P_f}{\partial t} - \frac{\partial}{\partial t}\left((W_{fi} - W_p)B_w\right) + \frac{\partial V_f}{\partial t} \tag{A.9}$$

Eq. A.9 is further expanded using chain rule

$$-(q_g B_g + q_w B_w) = (G_{fi} - G_p)B_g c_g \frac{\partial P_f}{\partial t} + (W_{fi} - W_p)B_w c_w \frac{\partial P_f}{\partial t} + \frac{\partial V_f}{\partial P_f}\frac{\partial P_f}{\partial t} \tag{A.10}$$

Eq. A.10 is normalized by dividing both sides by the V_{fi}, which can be expressed either as a function of initial gas saturation (S_{gi}) or initial water saturation (S_{wi})

$$V_{fi} = \frac{G_{fi}B_{gi}}{S_{gi}} = \frac{W_{fi}B_{wi}}{S_{wi}} \tag{A.11}$$

$$-\frac{1}{V_{fi}}(q_g B_g + q_w B_w) = \frac{(G_{fi}-G_p)B_g c_g}{\frac{G_{fi}B_{gi}}{S_{gi}}}\frac{\partial P_f}{\partial t} + \frac{(W_{fi}-W_p)B_w c_w}{\frac{W_{fi}B_{wi}}{S_{wi}}}\frac{\partial P_f}{\partial t} + \frac{1}{V_{fi}}\frac{\partial V_f}{\partial P_f}\frac{\partial P_f}{\partial t} \tag{A.12}$$

Assuming $B_w \approx B_{wi}$ during EGP, Eq. A12 becomes

$$\frac{1}{V_{fi}}[q_g B_g + q_w B_w] = -\left[\left(1 - \frac{G_p}{G_{fi}}\right)\frac{B_g}{B_{gi}} S_{gi} c_g + \left(1 - \frac{W_p}{W_{fi}}\right) S_{wi} c_w + \frac{1}{V_{fi}}\frac{\partial V_f}{\partial P_f}\right]\frac{\partial P_f}{\partial t} \tag{A.13}$$

Eq. A.13 is simplified by defining an effective compressibility term, $\tilde{C}_t$ and a total flow rate, q_t. The final fracture material balance is given by:

$$\frac{\partial P_f}{\partial t} = -\frac{q_t}{\tilde{C}_t V_{fi}} \tag{A.14}$$

where $\tilde{C}_t = \left(1 - \frac{G_p}{G_{fi}}\right)\frac{B_g}{B_{gi}} S_{gi} c_g + \left(1 - \frac{W_p}{W_{fi}}\right) S_{wi} c_w + \frac{1}{V_{fi}}\frac{\partial V_f}{\partial P}$ (A.15)

and $q_t = q_g B_g + q_w B_w$. (A.16)

Eq. A14 is the final form of the closed-tank MBE for the effective fracture system.

Appendix B: Dynamic Relative Permeability for Transient Flow Modeling in Fractures during Flowback

Ezulike and Dehghanpour (2014b) proposed a DRP function to describe the transient relative permeability in fractures during early-time flowback period. The model assumes that 1) the fractures is saturated with hydrocarbon and water phases; 2) there is negligible water influx from the matrix system; and 3) the fracture pore volume (V_{pe}) does not change with time during flowback period. The DRP function is applicable for tight sandstone reservoirs and shales.

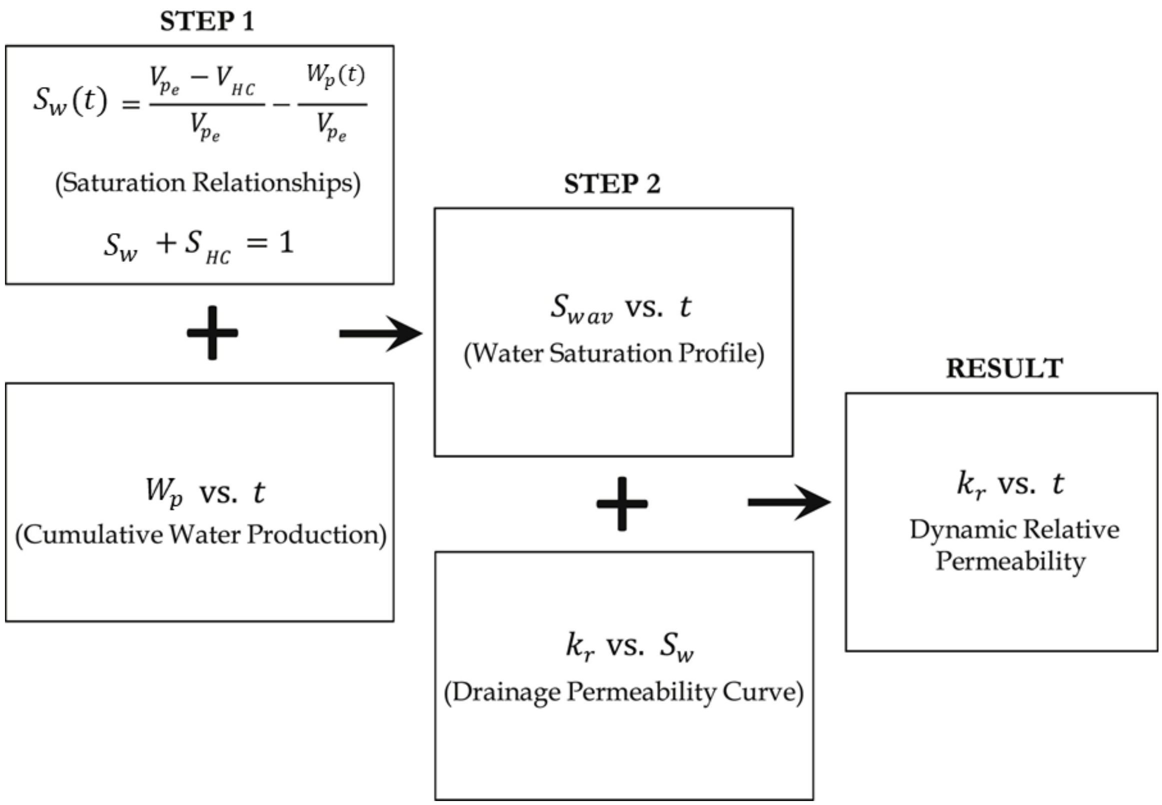

Figure B.1: Procedure to calculate relative permeability for two-phase flowback using the DRP model. *HC* and *w* in the subscripts represent hydrocarbon phase and water phase, respectively. (Modified from Ezulike and Dehghanpour, 2014b).

Figure B.1 shows the calculation procedure. First, the water saturation profiles in fractures is calculated from the cumulative water production profile and the volume of initial water inside the fractures. The hydrocarbon saturation profile in the fractures is also calculated since water and gas saturations add up to one. Then, the water and hydrocarbon relative permeability are calculated based on the saturation profiles and a representative relative permeability model such as Corey correlation. Finally, the calculated relative permeability are plotted with respect to time, and the data points are fitted using a general DPR function. The general form of the DPR model is given by:

$$k_{rg}(t) = \frac{\beta_1}{1+(\beta_2 t)^{-\beta_3}} \tag{B.1}$$

where β_1, β_2, β_3 are the fitting parameters that describes the rate of water saturation drop in fractures (i.e. fracture clean-up rate).

Appendix C: Derivation of the Closed-Tank Flowing Material Balance Equation for the Effective Fracture System

The $\frac{\partial \psi}{\partial t_a}$ term in the diffusivity equation (Eq. 4.8) can be related to the pseudo-pressure function (Eq. 4.5), pseudo-time function (Eq. 4.7), and the MBE (Eq. 4.2):

$$\frac{\partial \psi}{\partial t_a} = \frac{\partial P_f}{\partial t}\frac{\partial \psi}{\partial P_f}\frac{\partial t}{\partial t_a} \tag{C.1}$$

$$\frac{\partial \psi}{\partial t_a} = -\frac{2}{V_{fi}}\frac{q_t}{k_{rg}(t)}\frac{P_f}{Z} \tag{C.2}$$

Substituting $\frac{P_f}{Z}$ in Eq. C.2 using real gas law gives

$$\frac{P_f}{Z} = \frac{P_i}{Z_i}\frac{B_{gi}}{B_g} \tag{C.3}$$

$$\frac{\partial \psi}{\partial t_a} = -\frac{2}{V_{fi}}\frac{P_i}{Z_i}\frac{B_{gi}}{B_g}\frac{q_t}{k_{rg}(t)} \tag{C.4}$$

Define equivalent gas rate as

$$q_g{}^* = \frac{B_{gi}}{B_g}\frac{q_t}{k_{rg}(t)} = \frac{1}{k_{rg}(t)}\frac{B_{gi}}{B_g}\left[q_g B_g + q_w B_w\right] \tag{C.5}$$

Assuming $B_g \approx B_{gi}$ during EGP gives

$$q_g{}^* = \frac{1}{k_{rg}(t)}\left[q_g B_{gi} + q_w B_w\right] \tag{C.6}$$

Substituting Eq. C.6 into Eq. C.4 gives

$$\frac{\partial \psi}{\partial t_a} = -\frac{2}{V_{fi}}\frac{P_i}{Z_i}q_g{}^* \tag{C.7}$$

Substituting Eq. C.7 into the linear diffusivity equation (Eq. 4.8) gives

$$\frac{\partial^2 \psi(P_f)}{\partial y^2} = -\frac{\varphi_f}{K_f}\frac{2}{V_{fi}}\frac{P_i}{Z_i}q_g{}^* \tag{C.8}$$

Eq. C.8 can be solved using the following boundary conditions:

At the fracture tip, $y = Y_e,\ \frac{\partial\psi(P_f)}{\partial y} = 0$ (C.9)

At the wellbore, $y = 0,\ \psi(P_f) = \psi(P_{wf})$ (C.10)

Therefore,

$$\frac{\psi(\overline{P_f})-\psi(P_{wf})}{q_g^*} = \frac{\varphi_f}{K_f}\frac{2}{V_{fi}}\frac{P_i}{Z_i}\frac{Y_e^2}{3} \quad (C.11)$$

Define fracture storage coefficient (C_{st}) as

$$C_{st} = \frac{V_{fi}Z_i}{2P_i} \quad (C.12)$$

Thus, Eq. C.11 becomes

$$\frac{\psi(\overline{P_f})-\psi(P_{wf})}{q_g^*} = \frac{\varphi_f}{K_f}\frac{1}{C_{st}}\frac{Y_e^2}{3} \quad (C.13)$$

Combining Eqs. C.7 and C.12 gives

$$\frac{\partial t_a}{\partial\psi} = -C_{st}\frac{1}{q_g^*} \quad (C.14)$$

$$t_a = C_{st}\frac{\psi(P_i)-\psi(\overline{P_f})}{q_g^*} \quad (C.15)$$

Eq. A.31 is comparable to the material balance pseudo-time function suggested by Palacio and Blasingame (1993). Combining Eq. C.15with Eq. C.11, the flowing MBE can be expressed as a function of initial fracture pressure and wellbore BHP, both of which can be measured

$$\frac{\psi(P_i)-\psi(P_{wf})}{q_g^*} = \frac{\psi(P_i)-\psi(\overline{P_f})}{q_g^*} + \frac{\psi(\overline{P_f})-\psi(P_{wf})}{q_g^*} = \frac{1}{C_{st}}t_a + \frac{\varphi_f}{K_f}\frac{1}{C_{st}}\frac{Y_e^2}{3} \quad (C.16)$$

Eq. C.16 is the final form of the flowing MBE for the effective fracture system.

Appendix D: Key Calculation Results of the Two-Phase Flowing Material Balance Model

The flowback data for Wells D and F are analyzed following the analysis procedure proposed in Section 4.3. Figures D.1 to D.4 show the calculation results of two-phase relative permeability, q_g^* (Step 4), $\tilde{C}_t$ (Step 5), and t_a (Step 6), respectively. The data points correspond to EGP phase only.

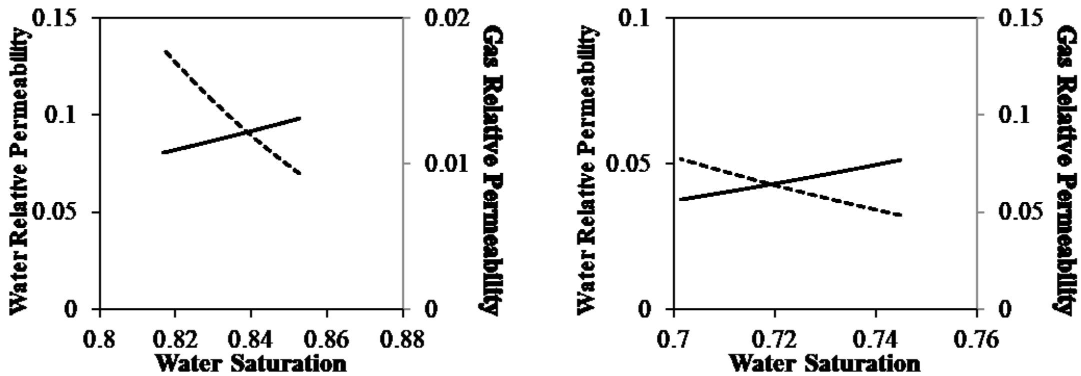

(a) (b)

Figure D.1: Two-Phase relative permeability functions for: (a) Well D and (b) Well F.

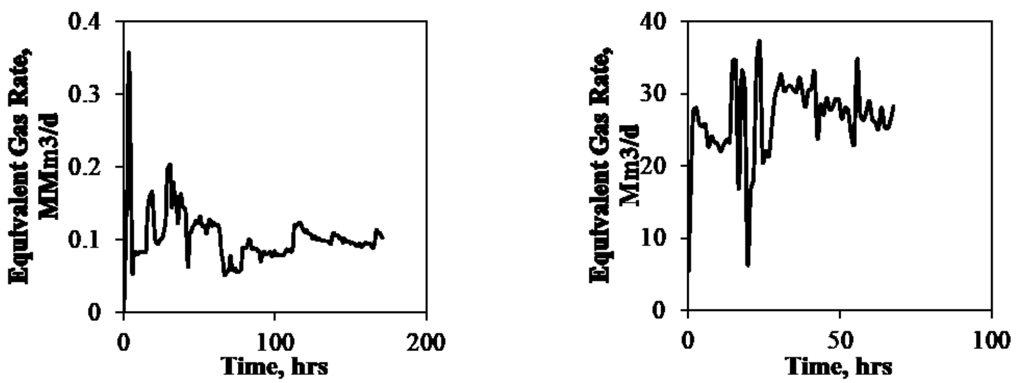

(a) (b)

Figure D.2: Calculated q_g^* during EGP: (a) Well D and (b) Well F.

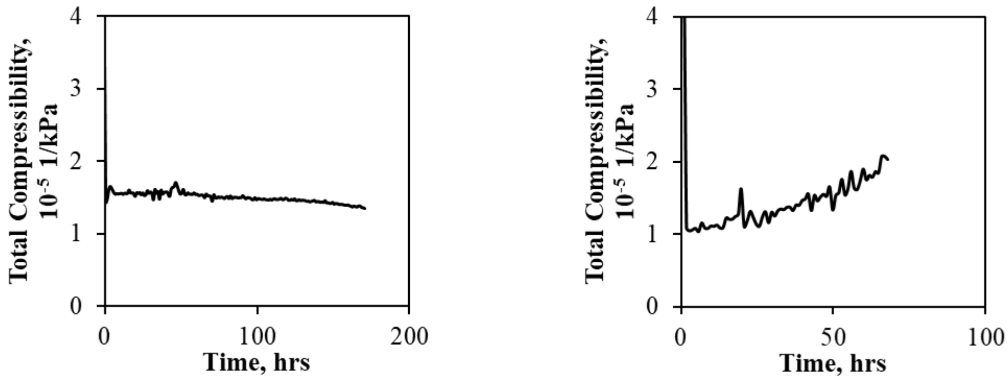

(a) (b)

Figure D.3: Calculated $\widetilde{C}_t$ during EGP: (a) Well D and (b) Well F.

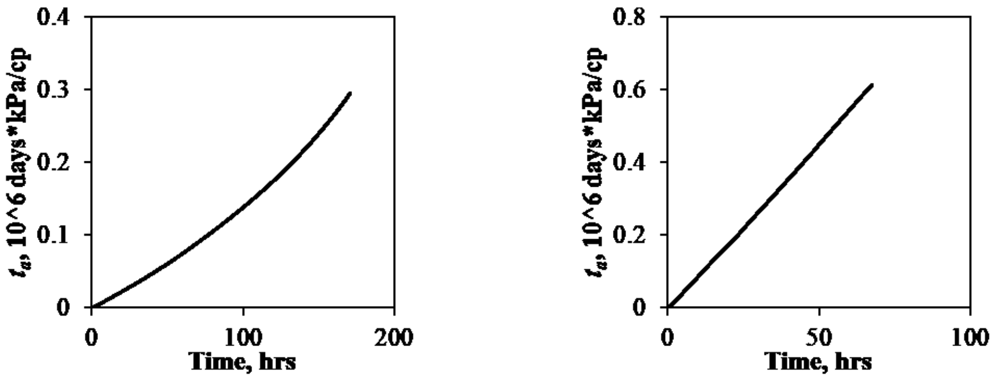

(a) (b)

Figure D.4: Calculated t_a during EGP: (a) Well D and (b) Well F.

Appendix E: Calculating Gas Influx Effect in the Open-Tank Model

The diffusivity equation for 1D gas flow is given by

$$\frac{\partial^2 m(P_m)}{\partial x^2} = \frac{\phi_m S_g}{k_m k_{rg}} \frac{\partial m(P_m)}{\partial t_a} \tag{E.1}$$

where m and t_a are the pseudo-pressure and pseudo-time functions that describe the pressure-/time-dependent gas properties respectively.

Eq. 5.10 suggest that when the fracture pressure is constant, the fracture pseudo-pressure will also be constant. Therefore, in this study, Eq. E.1 is solved using the constant pseudo-pressure boundary conditions:

Initial condition: $m(x, 0) = m(P_i)$ at $t = 0$ (E.2)

No-flow boundary: $\frac{\partial m(P_m)}{\partial x} = 0$ at $x = 0$ (E.3)

Fracture-matrix interface: $m(P_m) = m(P_f)$ at $x = L/2$ (E.4)

Eqs. E.5, E.6, E.7 and E.8 define the dimensionless length, dimensionless pseudo-pressure, dimensionless influx time and dimensionless rate, respectively:

$$x_D = \frac{x}{L/2} \tag{E.5}$$

$$m_D = \frac{m(P_i) - m(P_m)}{m(P_i) - m(P_f)} \tag{E.6}$$

$$t_D = \frac{k_m k_{rg}}{\phi_m S_g \mu_g c_t} \frac{1}{\left(\frac{L}{2}\right)^2} t \tag{E.7}$$

$$q_D = \frac{q_{in}^{SC}(t) T P_{sc} L}{T_{sc} k_m A_{mf} \, [m(P_i) - m(P_f)]} \tag{E.8}$$

Converting Eqs. E.1 to E.4 into dimensionless forms gives

$$\frac{\partial^2 m_D(P_m)}{\partial {x_D}^2} = \frac{\partial m_D(P_m)}{\partial t_{aD}} \tag{E.9}$$

Initial condition: $m_D(x_D, 0) = 0$ (E.10)

No-flow boundary: $\frac{\partial m_D}{\partial x_D} = 0$ at $x_D = 0$ (E.11)

Fracture-matrix interface: $m_D = 1$ at $x_D = 1$ (E.12)

Taking Laplace transform of Eqs. E.9 to E.12 gives

$$\frac{d^2\overline{m_D(P_m)}}{dx_D{}^2} = s\overline{m_D} - \overline{m_D}(x_D, 0) \tag{E.13}$$

Initial condition: $\overline{m_D}(x_D, 0) = 0$ (E.14)

No-flow boundary: $\frac{d\overline{m_D}}{dx_D} = 0$ at $x_D = 0$ (E.15)

Fracture-matrix interface: $\overline{m_D} = \frac{1}{s}$ at $x_D = 1$ (E.16)

The solution to Eq. E.13 is given by:

$$\overline{m_D(P_m)} = \frac{1}{s}\frac{cosh(\sqrt{s}\,x_D)}{cosh(\sqrt{s})} \tag{E.17}$$

Therefore, the dimensionless gas influx rate in Laplace space is given by

$$\overline{q_D} = \frac{d\overline{m_D(P_m)}}{dx_D}\Big|_{x_D=1} = \frac{1}{\sqrt{s}}tanh(\sqrt{s}\,) \tag{E.18}$$

Eqs. E.17 and E.18 are similar to the solutions of one-dimensional linear transient flow for production data analysis (El-Banbi and Wattenbarger, 1998; Bello, 2009). Eq. E.18 can be inverted to real-time space using the Stehfest algorithm (Stehfest, 1970). It should be noted that the inverse of the Laplace operator, s, corresponds to the dimensionless influx time, t_D.

Appendix F: Derivation of the Proppant Embedment into the Rock Matrix using Hertzian Contact Theory

Figure F.1 shows the schematic of an elastic sphere of radius r in contact with an elastic half-space at an applied force of F. The elastic sphere indents the half-space with depth of δ, and creates a contact area of radius a. δ and can be expressed using the Hertzian contact theory:

$$\delta = \frac{a^2}{r} = (\frac{9F^2}{16rE^{*2}})^{\frac{1}{3}} \tag{F.1}$$

$$\frac{1}{E^*} = \frac{1-v_1^2}{E_1} + \frac{1-v_2^2}{E_2} \tag{F.2}$$

where E_1 and E_2 are the Young's moduli of the sphere and the half-space, respectively. v_1 and v_2 are the Poisson's ratios of the sphere and the half-space, respectively. E^* can be viewed as an equivalent Young's modulus that describes the mechanical interaction between the sphere and the half-space.

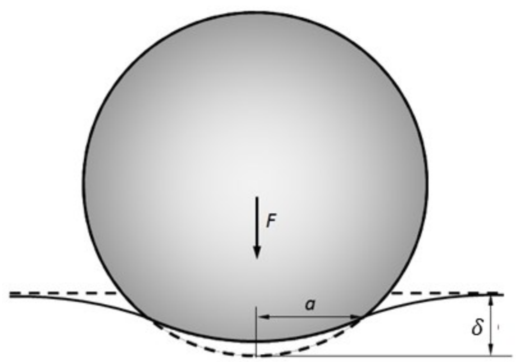

Figure F.1: Schematic illustration of an elastic sphere in contact with an elastic half-space under applied force of *F*. The sphere indents into the half-space with depth of δ, and forms a contact area of radius *r* (Modified from Wikipedia)

Let us consider a uniform layer of proppants in contact with a rock matrix, as shown in Figure. F2. The rock matrix can be assumed as an elastic half-space, while each proppant can be assumed as an elastic sphere in Figure. F1. The distance between the centres of two adjacent indenters is D, $D = 2r$. Therefore, the average force that applied on a single proppant is given by

$$F = P_e D^2 = 4r^2 P_e \tag{F.3}$$

where P_e is the effective pressure the fracture is subject to. According to Terzaghi (1923), $P_e = P_c - P_f$.

Substituting Eq. F.3 into Eq. F.1 gives the depth of indentation when the indenter layer imbeds into the rock matrix. Eq. F.4 gives the depth of indentation in the pressure form.

$$\delta = \left(\frac{9(4r^2 P_e)^2}{16rE^{*2}}\right)^{\frac{1}{3}} = r\left(\frac{3P_e}{E^*}\right)^{\frac{2}{3}} \tag{F.4}$$

$$\frac{1}{E^*} = \frac{1-v_s^2}{E_s} + \frac{1-v_r^2}{E_r} \tag{F.2}$$

where E_s and E_r are the Young's moduli of the proppant and the rock matrix, respectively. v_s and v_r are the Poisson's ratios of the proppant and the rock matrix, respectively. Eq. F.4 is the final form of proppant embedment depth used in this study.

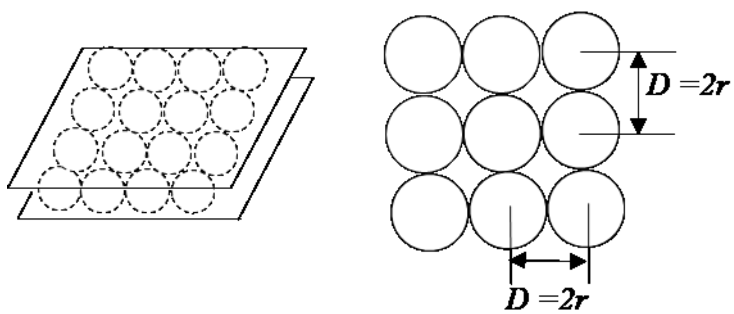

Figure F.2: Schematic illustration of a layer of proppants indents into the rock matrix (Modified from Li et al., 2015).

Appendix G: Fracture Conductivity Measurements of the Unpropped Fractures in the Horn River and the Barnett Shale Samples

Barnett Shale Samples

Zhang et al. (2014) conducted a series of laboratory experiments to measure the conductivity of fractures in the Barnett shales. The outcrops collected are the black-to-grayish-black shale in the Fort Worth Basin. Then, the shale outcrops were cut in to samples to fit their modified API conductivity cells. Special treatment such as frontend loader were used to acquire the shale samples with preserved natural fractures. Figure G.1 shows the dimensions of the samples, and the three types of natural fractures in their study.

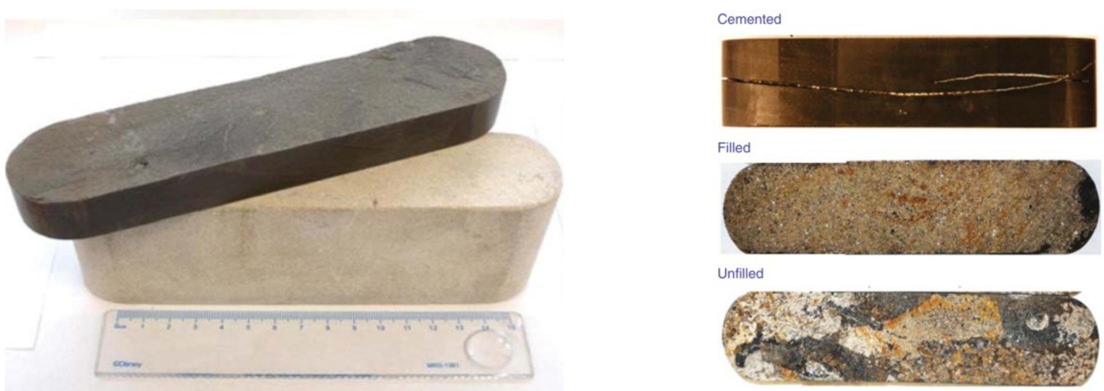

(a) (b)

Figure G.1: (a) Dimensions of the shale samples used in the fracture conductivity measurements; (b) Three types of preserved natural fractures in the shale samples: cemented, filled and unfilled (from Zhang et al., 2014).

Figure G.2 show the experimental setup, which include hydraulic load frame, gas-flow controller, conductivity cell, back pressure regulator, pressure sensors, nitrogen tank, and flow lines. The experiments were conducted at room temperature. The backpressure was set to be 50 psi. The conductivity measurements were run with closure stress/pressure from 500 psi to 4000 psi. A total of 22 samples with unpropped fractures are used in the experiments. Samples A to J are preserved natural fractures, which are cemented (Samples A and B), filled (Samples C to E), or unfilled (Samples F to J). Samples K to V are the unpropped induced fractures with preserved surface asperities. Table 6.3 presents the results of the conductivity measurements. Discussions about the experiment results are presented in Zhang et al. (2014).

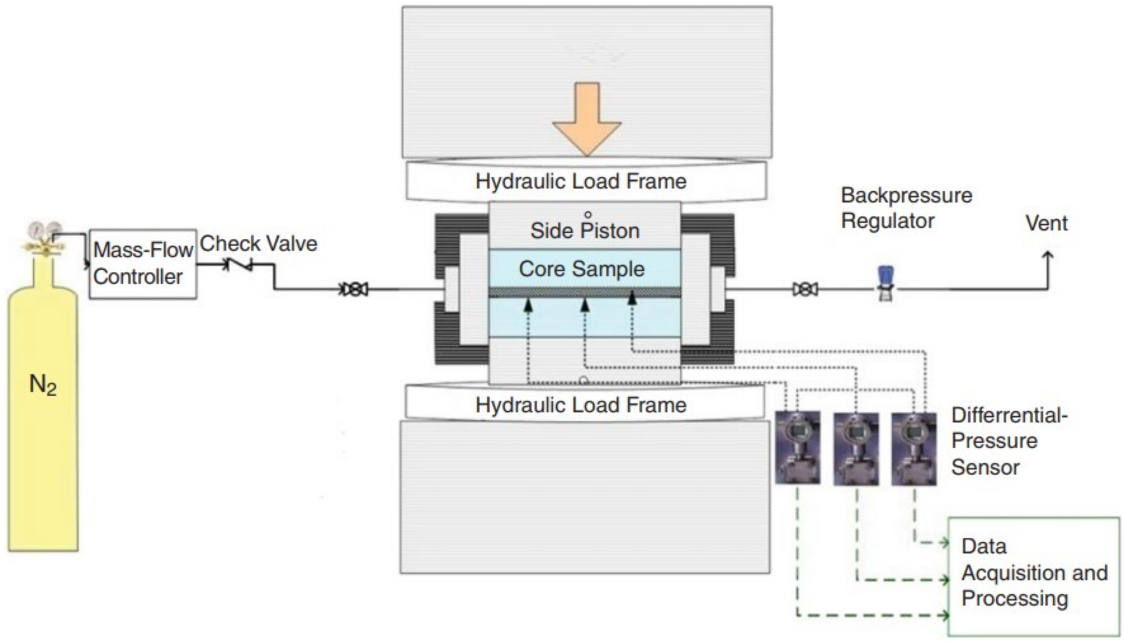

Figure G.2: Experimental apparatus of fracture conductivity measurements of the Barnett samples (from Zhang et al., 2014)

Horn River Shale Samples

The fracture conductivity tests for the12 HR samples were conducted by the Terra Tek lab. The samples are from the OP and EV members of the HRB, with depths varying from 2231 to 2395 m. The fracture conductivity experiments were conducted at the formation temperature of 240 °F. For each sample, fracture conductivity was measured at increasing closure pressure/stress from 500 to 10,000 psi. Three types of fluid are used to measure fracture conductivity: nitrogen (Samples A, B, G, and J), fresh water (Samples C, D, H, and K), and fresh water and clay stabilizer (Samples E, F, I, and L). Table 6.2 shows the measured fracture conductivity of the 22 HR samples. No relationship is observed between the test fluids and the measured conductivity data.

Appendix H: Simplification of the Compressibility Model for Propped Fractures

The derived c_f model for the propped fracture (Eq. 6.19) is revisited by neglecting the compaction of the proppant pack. In other words, the change of fracture aperture during fracture closure process only attributes to the embedment of the indenter layers into the rock matrix. Therefore, Eq. 6.9 becomes,

$$w_f = h_i + 2r - 2\delta \tag{H.1}$$

Before fracture closure, $P_e = 0$, $\delta = 0$, $w_{fi} = h_i + 2r$.

Substituting Eq. 6.10 into Eq. H.1 gives

$$w_f = h_i + 2r - 2r(\frac{3P_e}{E^*})^{\frac{2}{3}} \tag{H.2}$$

$$\frac{1}{E^*} = \frac{1-v_s^2}{E_s} + \frac{1-v_r^2}{E_r} \tag{H.3}$$

Differentiating Eq. H.2 gives the rate of fracture aperture change (i.e. $-\frac{1}{w_f}\frac{dw_f}{dP_e}$):

$$-\frac{1}{w_f}\frac{dw_f}{dP_e} = \frac{4r}{w_f E^*}\left(\frac{3P_e}{E^*}\right)^{-\frac{1}{3}} = \frac{4r}{(w_{fi}-2\delta)E^*}\left(\frac{3P_e}{E^*}\right)^{-\frac{1}{3}} \tag{H.4}$$

Substituting Eqs. H.4 and 6.12 into Eq. 6.9 gives

$$c_f = \frac{4r}{w_{fi}-2r(\frac{3P_e}{E^*})^{\frac{2}{3}}}(\frac{3P_e}{E^{*2}})^{-\frac{1}{3}} + \frac{2C_0}{P_e}\frac{\left(\frac{P_e}{E_0}\right)^{\frac{2}{3}}}{1-C_0\left(\frac{P_e}{E_0}\right)^{\frac{2}{3}}} \tag{H.5}$$

Eq. H.5 is the simplified model for estimating c_f of propped fractures. Compared with Eq. 6.19, Eq. H.5 has only two unknown parameters w_{fi} and C_o, and is more applicable for field practice.